UCL Université catholique de Louvain

École polytechnique de Louvain (EPL)

epl

The influence of spherical pores within the white matter on Diffusion-Weighted MRI signals : a numerical study using Monte-Carlo simulations

Dissertation presented by
Alain NIYIGABA ISHIMWE

for obtaining the Master's degree in
Electrical Engineering

Supervisor(s)
Pr. Benoit MACQ, Gaëtan RENSONNET

Reader(s)
Pr. Benoit MACQ, Gaëtan RENSONNET , Pr. John LEE

Academic year 2016-2017

Acknowledgements

In general, I thank my family to have supported me throughout all my studies and have motivated me along the way.

In particular, I thank my supervisors, Pr. Benoit Macq who has allowed me to work on this fascinating subject and have monitored my work during this year ; and PhD. candidate Gaëtan Ronsonnet who has helped me to grab the main concepts behind this work and has freely and generously shared his knowledge and his time.

Contents

Acknowledgements i

Contents iii

List of Figures vi

List of Tables vii

List of Abbreviations viii

Physical Constants ix

List of Symbols x

Introduction 1

1 Theoretical background : from NMR to MSI 2
- 1.1 Nuclear Magnetic Resonance . . . 2
  - 1.1.1 Basics of quantum mechanics . . . 2
  - 1.1.2 The net magnetization . . . 3
  - 1.1.3 Resonance and relaxation . . . 4
  - 1.1.4 The Bloch equations . . . 4
  - 1.1.5 The Spin Echo . . . 5
- 1.2 Magnetic Resonance Imaging . . . 6
- 1.3 Diffusion-Weighted Imaging . . . 7
  - 1.3.1 The Pulse-Gradient Spin Echo sequence . . . 7
  - 1.3.2 The diffusion process . . . 8
  - 1.3.3 The PGSE sequence with respect to the microscopic and macroscopic approach 9
- 1.4 Microstructure imaging . . . 10
  - 1.4.1 Superposition principle . . . 11
  - 1.4.2 Models present in the literature . . . 11

2 Synthetic DWI signals : generation - acquisition sequence - microstructure environment 14
- 2.1 Synthetic generation of DWI signals . . . 14
  - 2.1.1 Monte-Carlo simulations . . . 15
  - 2.1.2 Multiple correlation function approach . . . 16
- 2.2 Acquisition protocols . . . 17
  - 2.2.1 Custom multi-shell scheme . . . 17
  - 2.2.2 ActiveAx-like scheme . . . 18
  - 2.2.3 NODDI-like scheme . . . 18
- 2.3 Microstructure environments . . . 18
  - 2.3.1 Single pore within a voxel . . . 19

2.3.2 Hexagonally packed fascicles of identical axons surrounded by hexagonally distributed pores . . . 19
2.3.3 Crossing fascicles of identical axons surrounded by rectangularly distributed pores 22

3 Analysis of the impact of pores on the DWI signal 25
3.1 Determination of the Monte-Carlo simulation parameters . . . 25
3.1.1 Standard deviation study . . . 27
3.1.2 Bias study . . . 31
3.2 Comparison of the DWI signals . . . 33
3.2.1 Environment with pores only vs free diffusion . . . 35
3.2.2 Hexagonally packed fasciles of identical axons environment with vs without pores 36
3.2.3 Crossing fasciles of identical axons environment with vs without pores . . . 37
3.2.4 Results . . . 38
3.3 Determination of the effective extracellular diffusivity . . . 45

Conclusions and perspectives 51

A Determination of the intra-axonal and intra-glial volume fractions 52
A.1 For hexagonally packed fasciles of identical axons surrounded by hexagonally distributed glial cells . . . 52
A.1.1 Intra-axonal volume fraction . . . 52
A.1.2 Intra-glial volume fraction . . . 53
A.2 For crossing fasciles of identical axons surrounded by rectangularly distributed glial cells 53
A.2.1 Intra-axonal volume fraction . . . 53
A.2.2 Intra-glial volume fraction . . . 54

B MC simulation parameters 55
B.1 Standard deviation study . . . 55
B.2 Bias study . . . 57

C Comparison of DWI signals for the second set of microstructure parameters 59

D Determination of the effective extracellular diffusivity for the second set of microstructure parameters 65

Bibliography 69

List of Figures

1.1 Orientation of a particle with a spin quantum number s equal to $\frac{1}{2}$ (such that $m_s = \pm\frac{1}{2}$), in the presence of a magnetic field $\boldsymbol{B_0}$. . . . 3
1.2 Precession movement of a spinning particle in the presence of an external magnetic field $\boldsymbol{B_0}$. . . . 3
1.3 Time diagram of the spin echo pulse sequence and the corresponding MR-signals. . . . 5
1.4 Consecutive application of a 90°-pulse and a 180°-pulse on a longitudinal magnetization. 6
1.5 Phase encoding of the spin in MRI. . . . 7
1.6 The Pulse-Gradient Spin Echo sequence. . . . 8
1.7 Brain microstucture imaging. . . . 11

2.1 Spin reflecting on an impermeable cell membrane. . . . 16
2.2 Hexagonally packed fascicles of identical axons surrounded by hexagonally distributed pores 20
2.3 Variation of the intra-pore volume fraction in function of radius of the pores, for the hexagonally packed fascicles of identical axons surrounded by hexagonally distributed pores. . . . 22
2.4 Crossing fascicles of identical axons surrounded by rectangularly distributed pores. . . 23
2.5 Variation of the intra-pore volume fraction in function of radius of the pores, for the crossing fascicles of identical axons surrounded by rectangularly distributed pores. . . . 24

3.1 Variation of the free water molecule diffusion variance in function of the b-values. . . . 27
3.2 Attenuation signal in function of the z-component of the gradient direction $\hat{\boldsymbol{g}}$ for various number N of spins and for a b-value of $1000\frac{s}{mm^2}$ using a number T of time steps fixed to 2×10^4. . . . 28
3.3 Variation of the standard deviation in fonction of the number N of spins using a custom multi-shell scheme for the hexagonal packing environment and with the number T of time steps fixed to 2×10^4. . . . 29
3.4 Attenuation signal in function of the z-component of the gradient direction $\hat{\boldsymbol{g}}$ for various number N of spins and for a b-value of $10000\frac{s}{mm^2}$. . . . 29
3.5 Representation of the b-vectors that yield a standard deviation higher than the standard deviation of the free diffusion for the hexagonal packing environment. . . . 30
3.6 Variation of the bias in fonction of the number T of time steps using a custom multi-shell scheme for the hexagonal packing environment and with the number N of spins fixed to 1.5×10^4. . . . 32
3.7 Signal attenuation in function of the z-component of the gradient direction $\hat{\boldsymbol{g}}$ for various number T of time steps and for a b-value of $1000\frac{s}{mm^2}$ using a number N of spins fixed to 1.5×10^4. . . . 32
3.8 Attenuation signal in function of the gradient direction $\hat{\boldsymbol{g}}$ for various b-values and for the hexagonal packing environment, using a number N of spins equal to 1.5×10^4 and a number T of time steps equal to 10^6. . . . 33
3.9 Illustration of the environments used in the comparison study and to determine the effective diffusivity. . . . 34

3.10 Attenuation signals obtained using the ActiveAx-like scheme for the environments with pores only and in the case of free diffusion. . . . 38
3.11 Attenuation signals obtained using the NODDI-like scheme for the environments with pores only and in the case of free diffusion. . . . 39
3.12 Attenuation signals obtained using the ActiveAx-like scheme for the hexagonally packed fasciles of identical axons environment with vs without pores. . . . 40
3.13 Attenuation signals obtained using the NODDI-like scheme for the hexagonally packed fasciles of identical axons environment with vs without pores. . . . 41
3.14 MC attenuation signals obtained using the ActiveAx-like scheme for the crossing fasciles of identical axons environment with vs without pores. . . . 42
3.15 MC attenuation signals obtained using the NODDI-like scheme for the crossing fasciles of identical axons environment with vs without pores. . . . 42
3.16 Differences between the MC signals computed with and without pores. . . . 43
3.17 Attenuation signals obtained using the ActiveAx-like scheme for the crossing fasciles of identical axons environment with vs without pores considered without water molecules. 43
3.18 Attenuation signals obtained using the NODDI-like scheme for the crossing fasciles of identical axons environment with vs without pores considered without water molecules. 44
3.19 Attenuation signals obtained using the ActiveAx-like scheme for the crossing fasciles of identical axons environment with vs without pores considered filled with water molecules. 44
3.20 Attenuation signals obtained using the NODDI-like scheme for the crossing fasciles of identical axons environment with vs without pores considered filled with water molecules. 45
3.21 Attenuation signals obtained using the ActiveAx-like scheme for the hexagonally packed fasciles of identical axons environment, considering various diffusivity values when no pores are present and the intrinsic diffusivity value D_{int} when empty rigid pores are present, with a relative intra-pore volume fraction $f_{in_{(s,rel)}}$ of 0.10. . . . 47
3.22 MC signals obtained using the NODDI-like scheme for the crossing fasciles of identical axons environment, considering various diffusivity values when no pores are present and the intrinsic diffusivity value D_{int} when pores are present, with a relative intra-pore volume fraction $f_{in_{(s,rel)}}$ of 0.02. . . . 47
3.23 Variation of the effective extracellular diffusivity D_{eff} in function of the relative intra-pore volume fraction $f_{in_{(s,rel)}}$ for free diffusion environment with respect to the pores only environment. . . . 48
3.24 Variation of the effective extracellular diffusivity D_{eff} in function of the relative intra-pore volume fraction $f_{in_{(s,rel)}}$ for hexagonally packed fasciles of identical axons environment without pores with respect to the similar environment with pores, using the microstructure parameters of the firs set. . . . 49
3.25 Variation of the effective extracellular diffusivity D_{eff} in function of the relative intra-pore volume fraction $f_{in_{(s,rel)}}$ for crossing fasciles of identical axons environment without pores with respect to the similar environment with pores, using the microstructure parameters of the firs set. . . . 50

B.1 Variation of the standard deviation in fonction of the number N of spins using a custom multi-shell scheme for the crossing fascicles environment and with the number T of time steps fixed to $2x10^4$. . . . 55
B.2 Representation of the b-vectors that yield a standard deviation higher than the standard deviation of the free diffusion for the crossing fascicles environment. . . . 56
B.3 Attenuation signal in function of the gradient direction $\hat{\boldsymbol{g}}$ for various b-values and for the crossing fascicles environment, using a number N of spins equal to $1.5x10^4$ and a number T of time step equal to 10^6. . . . 57
B.4 Variation of the bias in fonction of the number T of time steps using a custom multi-shell scheme for the crossing fascicles environment and with the number N of spins fixed to $1.5x10^4$. . . . 57

B.5 Attenuation signal in function of the gradient direction $\hat{g}$ for various b-values and for a environment with gamma-distributed cylinder radii, using a number N of spins equal to $1.5x10^4$ and a number T of time step equal to 10^6. 58
B.6 Variation of the bias in fonction of the number T of time steps using a custom multi-shell scheme for a environment with gamma-distributed cylinder radii and with the number N of spins fixed to $1.5x10^4$. 58

C.1 MC attenuation signals obtained using the ActiveAx-like scheme for the crossing fasciles of identical axons environment with vs without pores. 59
C.2 MC attenuation signals obtained using the NODDI-like scheme for the crossing fasciles of identical axons environment with vs without pores. 60
C.3 Differences between the MC signals computed with and without pores. 60
C.4 Attenuation signals obtained using the ActiveAx-like scheme for the crossing fasciles of identical axons environment with vs without pores considered without water molecules. 61
C.5 Attenuation signals obtained using the NODDI-like scheme for the crossing fasciles of identical axons environment with vs without pores considered without water molecules. 61
C.6 Attenuation signals obtained using the ActiveAx-like scheme for the crossing fasciles of identical axons environment with vs without pores considered filled with water molecules. 62
C.7 Attenuation signals obtained using the NODDI-like scheme for the crossing fasciles of identical axons environment with vs without pores considered filled with water molecules. 62
C.8 Attenuation signals obtained using the ActiveAx-like scheme for the hexagonally packed fasciles of identical axons environment with vs without pores. 63
C.9 Attenuation signals obtained using the NODDI-like scheme for the hexagonally packed fasciles of identical axons environment with vs without pores. 64

D.1 Attenuation signals obtained using the ActiveAx-like scheme for the hexagonally packed fasciles of identical axons environment, considering various diffusivity values when no pores are present and the intrinsic diffusivity value D_{int} when empty rigid pores are present, with a relative intra-pore volume fraction $f_{in_{(s,rel)}}$ of 0.15. 65
D.2 MC signals obtained using the NODDI-like scheme for the crossing fasciles of identical axons environment, considering various diffusivity values when no pores are present and the intrinsic diffusivity value D_{int} when pores are present, with a relative intra-pore volume fraction $f_{in_{(s,rel)}}$ of 0.04. 66
D.3 Variation of the effective extracellular diffusivity D_{eff} in function of the relative intra-pore volume fraction $f_{in_{(s,rel)}}$ for hexagonally packed fasciles of identical axons environment without pores with respect to the similar environment with pores, using the microstructure parameters of the firs set. 67
D.4 Variation of the effective extracellular diffusivity D_{eff} in function of the relative intra-pore volume fraction $f_{in_{(s,rel)}}$ for crossing fasciles of identical axons environment without pores with respect to the similar environment with pores, using the microstructure parameters of the firs set. 68

List of Tables

2.1 Values of the gradient intensity G and the pulse duration δ (custom multi-shell). 17
2.2 b-values composing the custom 9-shell scheme. 18
2.3 Parameters of the spherical pores (single pore within a voxel). 19
2.4 Parameters of the cylindrical axons (hexagonal packing - crossing fascicles). 21
2.5 Parameters of the spherical pores (hexagonal packing - crossing fascicles). 22

3.1 Simulation parameters investigated for the MC simulations 26
3.2 Environment parameters investigated for the MC simulations. 26
3.3 Time step dynamic of the environment composed of hexagonally packed fascicles of identical axons surrounded by hexagonally distributed pores, using the first set of environment parameters. 31
3.4 Time step dynamic of the environment composed of crossing fascicles of identical axons surrounded by rectangularly distributed pores, using the first set of environment parameters. 31
3.5 Simulation parameters for the MC simulations of the attenuation signals used in the comparison study (using a diffusivity equal to $3 \times 10^{-9} \frac{m^2}{s}$), together with the corresponding complexity U and time step. 33
3.6 PGSE parameters of the two clinically-realistic protocols that are used (i.e. ActiveAx-like and NODDI-like schemes). 36
3.7 Candidate values for effective extracellular diffusivity used to determine the effective extracellular diffusivity D_{eff} in the case of hexagonally packed and crossing fasciles of identical axons environments. 45
3.8 Relative intra-pore volume fraction corresponding to an effective diffusivity equal to the commonly used diffusivity (i.e. $2 \times 10^{-9} \frac{m^2}{s}$) in the MC simulations found in the literature, for the first set of environment configuration. 46

List of Abbreviations

CSF	**C**erebro**S**pinal **F**luid
DIAMOND	**DI**stribution of **A**nisotropic **M**icr**O**structural e**N**vironments with **D**iffusion-Weighted Imaging
DTI	**D**iffusion **T**ensor **I**maging
DWI	**D**iffusion-**W**eighted **I**maging
DW-MRI	**D**iffusion-**W**eighted **M**agnetic **R**esonance **I**maging
FID	**F**ree **I**nduction **D**ecay
GPD	**G**aussian **P**hase **D**istribution
MC	**M**onte-**C**arlo
MRI	**M**agnetic **R**esonance **I**maging
MSI	**M**icro-**S**tructure **I**maging
MTM	**M**ulti-**T**ensor **M**odel
NMR	**N**uclear **M**agnetic **R**esonance
PDE	**P**artial **D**ifferential **E**quation
PGSE	**P**ulsed-**G**radient **S**pin **E**cho
SE	**S**pin **E**cho
SPG	**S**hort **P**ulse **G**radient
RF	**R**adio **F**requency

Physical Constants

Boltzmann's constant	$k = 1.38 \times 10^{-23} \frac{\mathrm{J}}{\mathrm{K}}$
Intrinsic extracellular diffusivity	$D_{int} = 3.0 \times 10^{-9} \frac{\mathrm{m}^2}{\mathrm{s}}$
Nuclear gyromagnetic ratio	$\gamma = 42.576 \times 10^{6} \frac{\mathrm{Hz}}{\mathrm{T}}$ $\gamma = 2\pi \ \gamma \frac{rad}{sT}$
Planck's constant	$h = 6.6 \times 10^{-34}\,\mathrm{J\,s}$

List of Symbols

b or b_{pgse}	b-value	$\frac{\mathrm{s}}{\mathrm{m}^2}$
B	external magnetic field	T
c	concentration of substance	$\frac{\mathrm{mol}}{\mathrm{m}^3}$
E	DW-MRI signal attenuation	-
f_0	Lamor precession frequency	Hz
$\boldsymbol{g}$	3-D encoding gradient	$\frac{\mathrm{T}}{\mathrm{m}}$
$\boldsymbol{J}$	diffusion flux	$\frac{\mathrm{mol}}{\mathrm{m}^2\mathrm{s}}$
l	azimutal quantum number	-
m	magnetic quantum number	-
M	net magnetization	$\frac{\mathrm{N}}{\mathrm{Tm}^2}$
n	principal quantum number	-
$\boldsymbol{p}_{pgse}$	pulse-gradient spin echo parameters	($\frac{\mathrm{T}}{\mathrm{m}}$,s,s)
P	probability distribution	-
$\boldsymbol{q}$	vector of the q-space	m^{-1}
R	radius	m
s	spin quantum number	-
S	DW-MRI signal	-
S_0	T_2-weighted reference signal	-
T	temperature	K
T_1	spin-lattice relaxation time	s
T_2	spin-spin relaxation time	s
T_E	echo time	s
T_R	repetition time	s
T_{RF}	pulse duration	s

α	flip angle	rad
δ	duration of one pulse	s
Δ	time between two consecutive pulses	s
μ	magnetic moment	$\frac{\mathrm{Nm}}{\mathrm{T}}$
ϕ	phase angle	rad
ω_0	Lamor precession angular velocity	$\frac{\mathrm{rad}}{\mathrm{s}}$
Ω	diffusion environment	-
ρ	spin density	$\frac{\#}{\mathrm{m}^3}$

Introduction

Disabilities, diseases or disorders caused by brain damage are quite vast, ranging from simply aging to mental illnesses such as schizophrenia as well as stroke, multiple sclerosis, autism or Alzheimer's disease. These diseases and disorders affect children, women or men worldwide without any discrimination, at any stage of their life [7, 10]. Therefore, any tool that might help in the early detection of those abnormalities or any of their characteristic features is eagerly welcome.

Interestingly, in the past few decades, a new and non-invasive imaging method, diffusion-weighted magnetic resonance imaging (DW-MRI), also known as diffusion-weighted imaging (DWI), has emerged for assessing the microstructure of the brain (e.g. the orientation of the axons or their radius). This approach is based on the diffusion of water molecules within tissues. Researchers have started to investigate this method as injuries alter the diffusion in a characteristic manner [15] due to the fact that diffusion of water molecule is sensitive to the underlying tissue microstructure [6]. Additionally, links were established between diseases and microstructural abnormalities, for example, damage affecting small-diameter axons were linked to cognitive impairment, whereas damage caused by a large-diameter were related to physical disabilities [24].

Subsequently, MRI methods were numerously developed and used to assess brain characteristics. For example multi-compartmental tissue models, in which fascicles of axons are modelled by infinitely long cylinders and glial cells by spherical pores, were used to evalute which model is best suited for clinical data [33, 34]. Additional researchers used multi-compartmental models to find the optimal PGSE sequence settings [9], to validate a phantom that mimic tumour cellular structure [19], or to investigate the diffusion in compartment models based on animal diseases [16].

Consequently, this Master's Thesis aims to provide additional insight into the theory of DW-MRI, especially in the development of multi-compartmental tissue models, by validating biophysically the use of an apparent lower intrinsic diffusivity. Altough lowering this value allows to artificially incorporate additional (restriction) phenomena that are not simulated. For instance, the apparent diffusion coefficient is influenced by membrane permeability, cellular volume fraction, extracellular or intracellular diffusion [28].

To do so, theoretical notions of DW-MRI are first developed in chapter 1, together with a quick overview of existing multi-compartmental models. Then in chapter 2, reference is made on the synthetic generation method of the DWI signals developed along with the proposed acquisition sequences needed to simulate those signals. In this chapter, the microstructure environments are also thoroughly detailed along with their configuration settings.

Afterwards, in chapter 3, emphasis is put on the determination of the simulation parameters that are necessary to synthetically generate the DWI signals. Additionally, a comparative study of the simulated signal is provided. This study investigate two different sets of configuration parameters of our multi-compartment environments while considering two physical representations for the pores. The latter is considered as glial cells, when filled with water molecules, and as macromolecules in quasi solid-state or cellular debris, when empty. Finally, by considering different values for the diffusivity, microstructure parameters that justify the use of an effective diffusivity are highlighted.

Chapter 1

Theoretical background : from NMR to MSI

This chapter aims to introduce the reader to the main theoretical concepts behind this master thesis. Any reader familiar with the concepts behind Diffusion Weighted Magnetic Imaging can readily skip this chapter.

The chapter is organized as follows : in

§1.1 *Starting form some quantum mechanic bases, we develop the notion of magnetization for particles with a spin quantum number equal to $\frac{1}{2}$ (such as hydrogen in water molecules); and describe how we can interfere with it, using a Radio-Frequency pulse. Additionally, we discuss the consequence of the application of this RF signal and provide mathematical formulations, in order to grab the general notion around Nuclear Magnetic Resonance.*

§1.2 *Using properties developed earlier, we explain how a Magnetic Resonance Image can be obtained by applying linear magnetic field gradients on a specific region of the body.*

§1.3 *Merging the notions of MRI and diffusion, we explain the Diffusion-Weighted Imaging process : by first introducing the concept of a Pulse-Gradient Spin Echo sequence, then by describing the diffusion with two different approaches (a microscopic and a macroscopic one), and finally by mixing both concepts to characterize the DW-MRI signal.*

§1.4 *Considering DW-MRI signals of voxels and the superposition principle, we develop how we can derive a certain microstructure of the brain, and we provide some examples of models that are present in the literature.*

1.1 Nuclear Magnetic Resonance

1.1.1 Basics of quantum mechanics

Nuclear Magnetic Resonance (NMR) is an analysis technique relying on the magnetic properties of the nuclei of the atoms. Conformally to the quantum mechanic theory, the nucleus of an atom is characterized by four quantum numbers: the principal quantum number (n), the magnetic quantum number (m), the azimuthal quantum number (l) and the spin quantum number (s) [32]. The latter ($s \in \{0, \frac{1}{2}, 1, \frac{3}{2}, 2\}$) [32] , in the presence of an external magnetic field (i.e. $\boldsymbol{B_0} = B_0 \boldsymbol{e_z}$), allows the orientation of a particle to be determined, i.e. a particle with $s = \frac{1}{2}$ has two possible orientations (FIGURE 1.1) that correspond to two different energy states [22, 17]. This is so, because a particle with a non-zero spin quantum number (called abusively "*spin*") can be represented in a pictorial way as a particle rotating around its axis [22, 17]. Furthermore, as the particle is charged, its rotation generates an electrical current that subsequently induces a magnetic field characterized by its magnetic

moment $\boldsymbol{\mu}$ [22, 17]. Due to the external magnetic field, this magnetic moment experiences a torque [22] ($\boldsymbol{\Gamma} = \boldsymbol{\mu} \times \boldsymbol{B_0}$) that causes a precession movement around the field axis (FIGURE 1.2) [22, 17]. The angular velocity of this precession is known as the Larmor frequency and is given by [22]

$$\omega_0 = \gamma B_0 \Leftrightarrow f_0 = \gamma B_0 \,, \tag{1.1}$$

where γ is the gyromagnetic ratio (a characteristic of the nucleus) and is equal to $42.58 \frac{\text{MHz}}{\text{T}}$ for a proton (^1H).

(A) **Parallel alignment that correspond to a lower energy state.**

(B) **Anti-parallel alignment, that correspond to a higher energy state.**

FIGURE 1.1: **Orientation of a particle with a spin quantum number s equal to $\frac{1}{2}$ (such that $m_s = \pm\frac{1}{2}$), in the presence of a magnetic field B_0.** Figures adapted from [22].

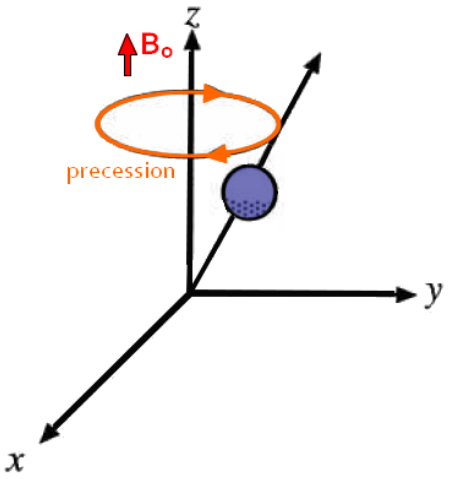

FIGURE 1.2: **Precession movement of a spinning particle in the presence of an external magnetic field B_0.** Figure adapted from [22].

1.1.2 The net magnetization

If a collection of spins, each characterized by their own magnetic moment, is considered; a macroscopic magnetization can be defined as [22]

$$\boldsymbol{M} = \frac{1}{V}\sum_i \boldsymbol{\mu}_i \,, \tag{1.2}$$

where V is the volume containing the spins.

If we limit the study to the case of particles with spin quantum number equal to $\frac{1}{2}$, the vector sum is equal to zero, as the spins are generally randomly oriented [22, 17]. However, when an external magnetic field is applied, the macroscopic magnetization becomes non-zero and is oriented in the same direction as the applied field, $\boldsymbol{M} = M_0 \boldsymbol{e_z}$, due to the fact that there are more parallel (lower energy) spins than anti-parallel (higher energy) ones [22, 17] ; where M_0 can be computed as [22]

$$M_0 = \frac{\gamma^2 h^2 \rho B_0 s(s+1)}{3kT} , \tag{1.3}$$

with ρ being the spin density.

In the case of thermal equilibrium, the ratio of spins $\frac{N_\uparrow}{N_\downarrow}$ ($N_\uparrow$ and $N_\downarrow$ corresponding respectively to the number of parallel and anti-parallel spins) is determined by the Botlzmann distribution $e^{\frac{\Delta E}{kT}}$, where ΔE is the energy difference, k is the Boltzmann's constant and T the absolute temperature [22]. Knowing that $\Delta E \equiv E_\downarrow - E_\uparrow = hf_0 > 0$ with h being the Planck's constant, we get $\frac{N_\uparrow}{N_\downarrow} > 1$ [22].

1.1.3 Resonance and relaxation

Applying a RF-pulse, $\boldsymbol{B_1}(t)$, oscillating on resonance ($f_{RF} = f_0$), causes the magnetization $\boldsymbol{M}$ to tilt by an angle $\alpha = \gamma \int_{T_{RF}} B_1(t) dt$ [22] (called *the flip angle*) with respect to actual magnetization orientation, as the particles absorb the energy of the pulse.* However, in practice the RF-pulse has a finite duration and a constant amplitude, such that the flip angle is simplified to [22]

$$\alpha = \gamma B_1 T_{RF} , \tag{1.4}$$

where T_{RF} is the pulse duration. Specific values of α are 90° and 180°, therefore we speak respectively about a 90°-pulse or a 180°-pulse. The resulting magnetization has now a transverse component in addition of the longitudinal : [22]

$$\boldsymbol{M} = M_z \boldsymbol{e_z} + M_{xy} \boldsymbol{e_{xy}} . \tag{1.5}$$

However after some time, when the pulsed is no more applied, the system goes back to equilibrium : M_z evolves back to M_0 and M_{xy} disappears [22, 17]. This occurs in two distinct steps : the first one is called the spin-spin (or transverse) relaxation (or T_2-relaxation), and the second one, the spin-lattice (or longitudinal) relaxation (or T_1-relaxation) [22, 17]. In the T_2-relaxation, the spins lose their phase coherence causing M_{xy} to vanish; this occurs without any energy exchange and is mainly caused by field fluctuations and static inhomogeneities [22]. Furthermore, the spatial non-uniformities in the external field ($\boldsymbol{B_0}$) impacts the spin-spin relaxation; and to account for this, an effective relation time is considered instead : [22]

$$T_2^* = \left(\frac{1}{T_2} + \gamma \Delta B_0 \right)^{-1} , \tag{1.6}$$

with ΔB_0 being the spread of the external field. Whereas, in the case of T_1-relaxation, the spins exchange energy with the surrounding environment, in order to return to the Boltzmann equilibrium distribution; and so causing M_z to move back to M_0 [22, 17].

1.1.4 The Bloch equations

Using the following complex notation for the transversal component of magnetization and the external magnetic field :[25]

$$M_{xy}(\boldsymbol{r}, t) = M_x(\boldsymbol{r}, t) + i M_y(\boldsymbol{r}, t) \text{ and } B_{xy}(\boldsymbol{r}, t) = B_x(\boldsymbol{r}, t) + i B_y(\boldsymbol{r}, t) . \tag{1.7}$$

*Details on the effect of the RF-pulse on the magnetic moment is given in lecture notes [22] at the section 4.1.3 . Nevertheless, the general idea is that the low energy state protons absorb the energy of the RF-pulse becoming high energy state protons and causing a parity in the spin population (50% parallel spins and 50% anti-parallel spins); and that the RF-pulse forces the protons to synchronize and so to spin in phase.

The equations of motion used to describe the phenomenological evolution of the nuclear magnetization, $\boldsymbol{M}(\boldsymbol{r},t)$, in the presence of a general field, $\boldsymbol{B}(\boldsymbol{r},t)$, also known as the Bloch-equation, considering a stationary frame, become [23, 22]

$$\begin{cases} \dfrac{\partial M_{xy}}{\partial t}(\boldsymbol{r},t) = \underbrace{-i\gamma\Big(M_{xy}(\boldsymbol{r},t)B_z(\boldsymbol{r},t) - M_z(\boldsymbol{r},t)B_{xy}(\boldsymbol{r},t)\Big)}_{\text{Larmor precession}} - \underbrace{\dfrac{M_{xy}(\boldsymbol{r},t)}{T_2}}_{T_2\text{-relaxation}} \\ \dfrac{\partial M_z}{\partial t}(\boldsymbol{r},t) = \underbrace{i\dfrac{\gamma}{2}\Big(M_{xy}(\boldsymbol{r},t)\overline{B_{xy}(\boldsymbol{r},t)} - \overline{M_{xy}(\boldsymbol{r},t)}B_{xy}(\boldsymbol{r},t)\Big)}_{\text{Larmor precession}} - \underbrace{\dfrac{M_z(\boldsymbol{r},t) - M_0}{T_1}}_{T_1\text{-relaxation}} \end{cases}, \tag{1.8}$$

where $\overline{B_{xy}(\boldsymbol{r},t)}$ and $\overline{M_{xy}(\boldsymbol{r},t)}$ are respectively the complex conjugate form of $B_{xy}(\boldsymbol{r},t)$ and $M_{xy}(\boldsymbol{r},t)$. Note that, here, we consider a general external magnetic field that can also have xy-components (i.e. due to the application of a specific RF-pulse), that depend on the position of the spin (i.e. due to the application of magnetic field gradients) and that can vary in time (i.e. if the RF-pulse(s) or the gradients vary in time).

1.1.5 The Spin Echo

If only one RF-pulse is applied, the transverse magnetization induces a signal called Free Induction Decay (FID) that could be measured, but is not due to large signal loss caused by the T_2^*-relaxation [22]. On the contrary, the spin echo (SE, also called RF-echo) formed after the application of two consecutive RF-pulses (a 90°-pulse followed by a 180°-pulse), at a time 2τ, is preferably measured, as it is only influenced by the T_2-relaxation despite the fact that the envelope of the echo is still influenced by the T_2^*-relaxation (FIGURE 1.3) [22]. The 90°pulse converts the longitudinal magnetization into a transverse one, whereas 180°-pulse refocuses the dephasing at the other side of the transverse plane [22], as portrayed on FIGURE 1.4.

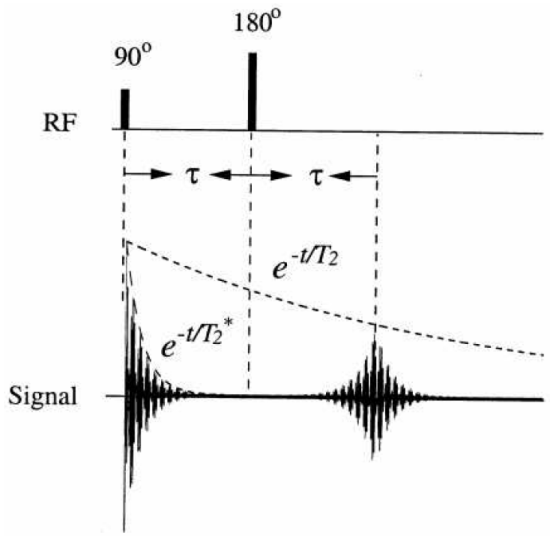

FIGURE 1.3: **Time diagram of the spin echo pulse sequence and the corresponding MR-signals.** Figure taken from [22].

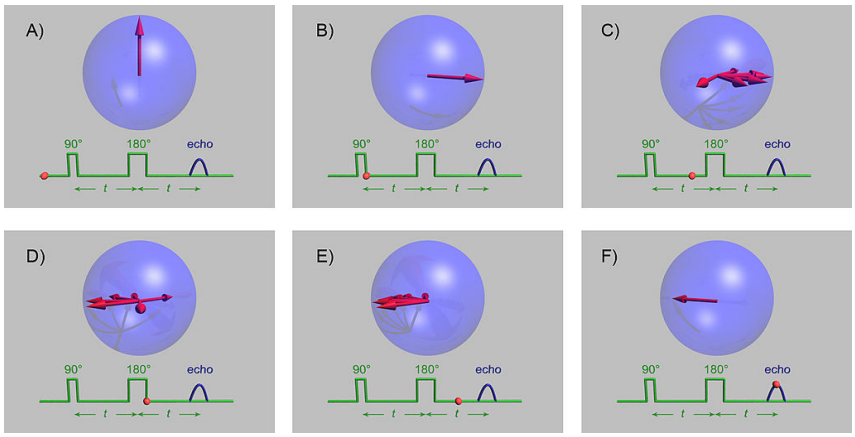

FIGURE 1.4: **Consecutive application of a 90°-pulse and a 180°-pulse on a longitudinal magnetization.** SOURCE: HTTPS://EN.WIKIPEDIA.ORG/WIKI/SPIN_ECHO.

1.2 Magnetic Resonance Imaging

In contrast to NMR, Magnetic Resonance Imaging (MRI) allows the MR-signals (FID or SE) to be localized in space, by exciting a specific region of the patient [22, 17]. This is done by applying three different magnetic field gradients† (G_x, G_y, G_z), which are generally much smaller than the already present static magnetic field, $\boldsymbol{B_0}$ [22, 17]. Those gradients generate an additional component, such that the total field becomes [22]

$$\boldsymbol{B}(\boldsymbol{r},t) = \boldsymbol{B_0} + \big(\boldsymbol{G}(t)\cdot\boldsymbol{r}\big)\boldsymbol{e_z}\ , \tag{1.9}$$

if we consider time varying gradients, and with $\boldsymbol{G(t)} = \big(G_x(t), G_y(t), G_z(t)\big)$ and $\boldsymbol{r} = \big(x,y,z\big)$. This subsequently causes the Larmor frequency to vary in position and time : [22]

$$f_0(\boldsymbol{r},t) = \gamma(B_0 + \boldsymbol{G}(t)\cdot\boldsymbol{r})\ . \tag{1.10}$$

This frequency variation in position is used to localize a specific area (a *slice*) : knowing that the Larmor frequency in the z-direction subject to a gradient G_z is equal to $f_0(z) = \gamma(B_0 + G_z z)$, a slice of thickness Δz can be selected by exciting the spins within this area with a RF-pulse of bandwidth $\Delta f = \gamma G_z \Delta z$ and a center frequency $f_c = f_0 + \gamma G_z z_0$, causing the desired area to resonate [22]. Nevertheless, as the local magnetic gradient is homogeneous in the two other directions, all the net magnetic moments in the slice are in phase, such that the spins can't yet be distinguished (localized) within the excited slice [22, 17].

In order to encode spatial information into the MR signals, first a phase encoding gradient is applied, for a short period of time, in one of the other directions (e.g. along the y-axis) [22, 17]. During the time it is on, this gradient causes the magnetic moments along the y-axis to spin with different frequency velocity [22, 17], as depicted of FIGURE 1.5. After the gradient is turned off, the moments go back to spinning at the same rate, but with different phases in the y-direction [22, 17]. Those variations in phase are used to localize the spins in the y-direction, by forcing the system to be sensitive to a specific phase [22, 17].

† [22] The magnetic field gradients (G_x, G_y, G_z) are defined as ($\frac{\partial B_z}{\partial x}$, $\frac{\partial B_z}{\partial y}$, $\frac{\partial B_z}{\partial z}$), such that $B_z = G_x x + G_y y + G_z z$. Additionally, we always have $B_x = 0$ and $B_y = 0$.

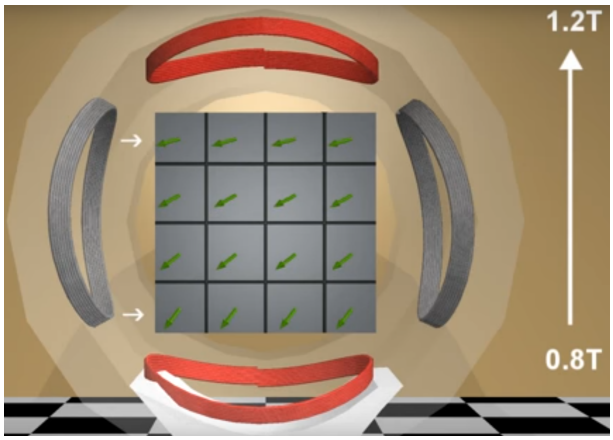

FIGURE 1.5: **Phase encoding of the spin in MRI.** Due to the application of the gradient, the spins at the bottom slow down and those at the top speed up. Figure taken from[17].

Subsequently, a frequency encoding gradient is applied, in the remaining direction (i.e. along the x-axis), to force the spins in the x-direction to spin with different frequency velocity [22, 17]. This gradient is held on during the recording of the MR-signal, as during this period every spin in the slice as a unique phase and frequency, allowing to easy localize them [22, 17]. This process (phase encoding and frequency encoding) is repeated until each area in the slice (called a *voxel*) is uniquely recorded, and given a gray-scale value[‡] corresponding to the strength of the MR-signal in the voxel [22, 17].

1.3 Diffusion-Weighted Imaging

Diffusion-Weighted Magnetic Resonance Imaging (DW-MRI), also known as Diffusion-Weighted Imaging (DWI), combines the use of RF pulses (in our case, a SE sequence) with the application of two consecutive linear magnetic fields, in order to produce a medical image. Doing so allows to capture the diffusion motion of the molecules within the area of interest and thereby gather information about the underlying microstructure.

1.3.1 The Pulse-Gradient Spin Echo sequence

As illustrated on FIGURE 1.6, the Pulse-Gradient Spin Echo (PGSE) sequence is characterized by three specific parameters : [25]

- $\boldsymbol{g} = G\hat{\boldsymbol{g}}$, the 3-D encoding gradient, with G its magnitude and $\hat{\boldsymbol{g}}$ is unitary direction ;
- Δ, the time between two onsets of the consecutive linear magnetic fields ;
- and δ, the duration of the 3-D gradient ;

and those parameters are grouped under one single vector $\boldsymbol{p}_{pgse} := (\boldsymbol{g}, \Delta, \delta)$.

[‡]In the gray-scale system used in MRI : white corresponds to a strong signal, whereas black corresponds to no (or a extremely weak) signal.

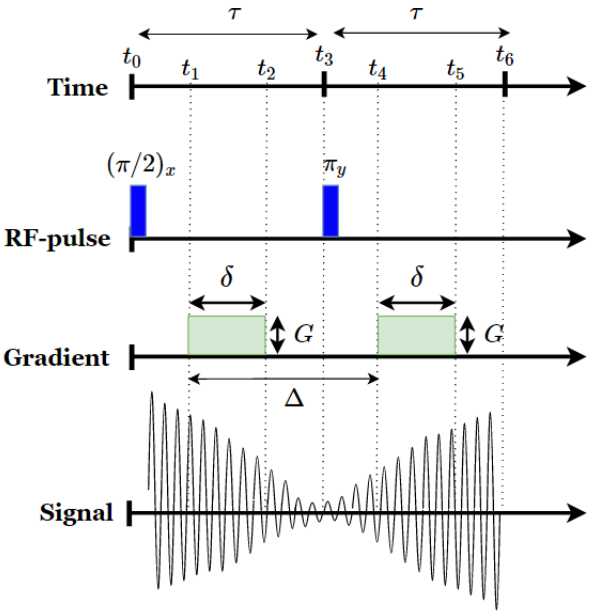

FIGURE 1.6: **The Pulse-Gradient Spin Echo sequence.** Figure adapted from [22].

As in MRI (§ 1.2), the on- and offset of the first 3-D gradient causes the spins that were precessing in phase after the application of the 90°-pulse to dephase, as they experience different Larmor frequencies while the gradient is on [23, 11]. The second 3-D gradient, which is of the same magnitude, direction and duration as the first one, is applied after the 180°-pulse, in order to refocus all the spins since their rotation have been inverted by the latter pulse [23, 11].

Now, considering the diffusion of molecules, if the spins were stationary, after the application of the second gradient, they should all be correctly refocused and the measured signal would be a classical SE [23, 11]. Nevertheless, as the particles moves (randomly or according to a specific direction), the refocusing is not perfect, hence the received signal undergoes some losses [23, 11].

1.3.2 The diffusion process

Diffusion is a process that aims to describe the movement of a substance within a specific region. There are mainly two approaches to understand the diffusion : an atomic (also called microscopic) approach considering the random walk of particles, or a phenomenological (also called macroscopic) approach using Fick's law [23].

The microscopic approach

The atomic approach considers diffusion as the motion of particles resulting from the random collision between one another; in which the particles move due to thermal agitation [23].

The macroscopic approach

The phenomenological approach is based on the diffusion equation : [23]

$$\frac{\partial c}{\partial t}(\boldsymbol{r},t) = \nabla \cdot (\boldsymbol{D} \cdot \nabla c(\boldsymbol{r},t)) \,, \tag{1.11}$$

where $c(\boldsymbol{r},t)$ is the concentration of substance that varies in position and time and $\boldsymbol{D}$ is a symmetric, positive-definite diffusion tensor. In the case of an isotropic diffusion [23]

$$\frac{\partial c}{\partial t}(\boldsymbol{r},t) = D\nabla^2 c(\boldsymbol{r},t) \,, \tag{1.12}$$

with $D > 0$, also called the diffusivity. Those equations are obtained by combining the equation of mass conservation (1.13); and Fick's law (1.14) that links the diffusive flux, $\boldsymbol{J}(\boldsymbol{r}, t)$, to the concentration, $c(\boldsymbol{r}, t)$, and that postulates that a substance diffuses from a high concentration region to a low concentration one : [23]

$$\frac{\partial c}{\partial t}(\boldsymbol{r}, t) = -\nabla \cdot \boldsymbol{J}(\boldsymbol{r}, t) \,, \tag{1.13}$$

$$\boldsymbol{J}(\boldsymbol{r}, t) = -\boldsymbol{D} \cdot \nabla c(\boldsymbol{r}, t) \,. \tag{1.14}$$

1.3.3 The PGSE sequence with respect to the microscopic and macroscopic approach

Considering the PGSE sequence, the overall magnetic field, resulting from the application of the RF-pulses and the gradient, which superposes itself to the static field, $\boldsymbol{B_0} = B_0 \boldsymbol{e_z}$, is summarized as [25]

$$\boldsymbol{B_1}(\boldsymbol{r}, t) = \big(f(t)\boldsymbol{g} \cdot \boldsymbol{r}\big)\boldsymbol{e_z} \,, \tag{1.15}$$

where $\boldsymbol{g} \cdot \boldsymbol{r}$ characterized the 3-dimensional linear magnetic field amplitude and $f(t)$ is a piecewise-constant temporal function that account for the application of the gradient and the inversion of the spins due to the 180°-pulse : [25]

$$f(t) = \begin{cases} 1, \text{ during the } 1^{st} \text{ application of the gradient} \\ -1, \text{ during the } 2^{nd} \text{ application of the gradient} \\ 0, \text{ otherwise} \end{cases} . \tag{1.16}$$

The microscopic approach

Knowing that the phase angle is obtained by integrating the angular velocity over a specific time period : [22]

$$\phi = \int_T \omega(\boldsymbol{r}, t) dt \overset{(1.1)}{=} \gamma \int_T B(\boldsymbol{r}, t) dt \,. \tag{1.17}$$

During the first part of the pulse sequence up to the 180°-pulse, a spin-bearing proton evolving in Brownian motion in a specific voxel experiences a phase shift [14]

$$\phi_k^{(1)}(\boldsymbol{g}, \delta) = \gamma \int_{t_0}^{t_3} B_0 + \boldsymbol{g} \cdot \boldsymbol{r_k}(t) dt = \underbrace{\gamma B_0 \tau}_{\substack{\text{uniform} \\ \text{magnetic} \\ \text{field}}} + \underbrace{\gamma \int_{t_1}^{t_1+\delta} \boldsymbol{g} \cdot \boldsymbol{r_k}(t) dt}_{\text{gradient dephasing}} \,, \tag{1.18}$$

where $\boldsymbol{r_k}(t)$ is the random position of the spin at time t. Similarly, during the second part of the pulse sequence, the proton experiences a phase shift [14]

$$\phi_k^{(2)}(\boldsymbol{g}, \Delta, \delta) = -\big(\gamma \int_{t_3}^{t_6} B_0 + \boldsymbol{g} \cdot \boldsymbol{r_k}(t) dt\big) = -\big(\underbrace{\gamma B_0 \tau}_{\substack{\text{uniform} \\ \text{magnetic} \\ \text{field}}} + \underbrace{\gamma \int_{t_1+\Delta}^{t_1+\Delta+\delta} \boldsymbol{g} \cdot \boldsymbol{r_k}(t) dt}_{\text{gradient rephasing}} \big) \,, \tag{1.19}$$

with the minus sign accounting for the inverting 180°-pulse. Such that the net phase is equal to[§] [14]

$$\phi_k(\boldsymbol{p}_{pgse}) = \phi_k^{(1)}(\boldsymbol{g}, \delta) + \phi_k^{(2)}(\boldsymbol{g}, \Delta, \delta) = \gamma\Big(\int_{t_1}^{t_1+\delta} \boldsymbol{g} \cdot \boldsymbol{r_k}(t) dt - \int_{t_1+\Delta}^{t_1+\Delta+\delta} \boldsymbol{g} \cdot \boldsymbol{r_k}(t) dt \Big) \,. \tag{1.20}$$

[§]The parameters $\boldsymbol{p}_{pgse}$ is used to indicate that the signal depends on $\boldsymbol{g}$, Δ and δ.

Recalling that a voxel contains a certain number of spins and considering that the phases of those spins follow a certain distribution $P_\Phi(\phi_k)$, the measured signal is equal to [14]

$$S(\boldsymbol{p}_{pgse}, T_E; \Omega) = S_0(T_E) \sum_{k=1}^{N} P_\Phi(\phi_k) e^{i\phi_k(\boldsymbol{p}_{pgse})} \cong S_0(T_E) \sum_{k=1}^{N} \frac{1}{N} e^{i\phi_k(\boldsymbol{p}_{pgse})} , \tag{1.21}$$

where Ω accounts for the diffusion environment and $S_0(T_E)$ is the T_2-weighted reference signal associated to the sample. The reference signal is the signal obtained without the gradients and measured at the echo time : [16]

$$S_0(T_E) = M_{xy,0} e^{-\frac{T_E}{T_2}} , \tag{1.22}$$

with $M_{xy,0} = M_{xy}(t_0) = M_x(t_0) + iM_y(t_0)$ being the net magnetization in the xy-plane right after the application of the 90°-pulse. Furthermore, as there are only approximations to estimate the expression of the probability distribution $P_\Phi(\phi_k)$, the signal in (1.21) can only be conjectured [14].

The macroscopic approach : Bloch-Torrey equation

Taking into account the diffusion process as described in section 1.3.2 and that the magnetic field has only a component along the z-axis, the transverse part of the Bloch equations of section 1.1.4 can be rewritten as [23]

$$\begin{aligned} \frac{\partial M_{xy}}{\partial t}(\boldsymbol{r}, t) &= -i\gamma M_{xy}(\boldsymbol{r}, t) B(\boldsymbol{r}, t) - \frac{M_{xy}(\boldsymbol{r}, t)}{T_2} + \nabla \cdot (\boldsymbol{D} \cdot \nabla M_{xy}(\boldsymbol{r}, t)) \\ &= \underbrace{-i\gamma M_{xy}(\boldsymbol{r}, t) B_0}_{\substack{\text{uniform} \\ \text{magnetic} \\ \text{field}}} \underbrace{-i\gamma M_{xy}(\boldsymbol{r}, t) B_1(\boldsymbol{r}, t)}_{\substack{\text{gradient} \\ \text{encoding}}} \underbrace{-\frac{M_{xy}(\boldsymbol{r}, t)}{T_2}}_{T_2\text{-relaxation}} + \underbrace{\nabla \cdot (\boldsymbol{D} \cdot \nabla M_{xy}(\boldsymbol{r}, t))}_{\text{diffusion}} \cdot \end{aligned} \tag{1.23}$$

If a solution can be founded for this PDE, then the measured signal in the transverse plane is obtained by integrating the net transverse magnetization over the positions of the spins in the diffusion environment Ω : [23]

$$S(\boldsymbol{p}_{pgse}, T_E; \Omega) = \int_\Omega M_{xy}(\boldsymbol{r}, T_E) d\boldsymbol{r} . \tag{1.24}$$

1.4 Microstructure imaging

Microstructure imaging is a non-invasive technique that aims to determine a specific structure of the body by matching it to an acquired image ; in the particular case of *brain microstructure imaging*, we try to correlate the signal obtained via DW-MRI to a cellular structure within the brain, i.e. the white matter (which is mainly composed of *axons* covered by a protecting shield called the *myelin*, and *glial cells*) [29].

To do so, the brain is considered as a set of subregions called *voxels* (that are typically of $\approx 8\, mm^3$) from which a certain number of scalar DW-MRI images are generated based on distinct combinations of parameters (i.e. $\boldsymbol{p}_{pgse}$) that are related to an analytical expression [29]. Then based on this link, a particular representation of the brain microstructure is inferred for each voxel, as illustrated on FIGURE 1.7.

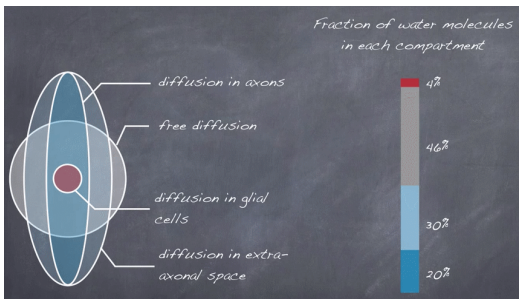

(A) **Representation of the microstructure of a specific voxel.**

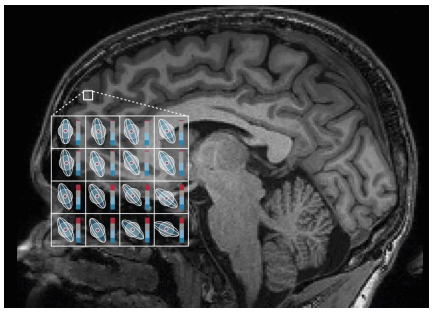

(B) **Representation of the microstructure of several neighboring voxels.**

FIGURE 1.7: **Brain microstructure imaging.** Figure taken from [29].

1.4.1 Superposition principle

The characterization of the brain microstructure using DW-MRI is eased by considering the superposition principle [29]. Considering a diffusion environment Ω (i.e. a voxel), the brain microstructure can be expressed as the union of mutually-disjoint and independent ($\equiv$ with perfectly reflecting boundaries) compartments Ω_i (i.e. the intra-axonal space, the intra-glial space or the free diffusion space), such that the DW-MRI signal can be expressed as [29]

$$S(\boldsymbol{p}_{pgse}, T_E; \Omega) = \sum_{i=1}^{K} f_i S(\boldsymbol{p}_{pgse}, T_E; \Omega_i) \,, \tag{1.25}$$

where $f_i = \frac{\Omega_i}{\Omega}$ correspond to the volume fraction of each compartment i. However, in practice, in order to avoid simulating the T_2-weighted reference signal, we work with the signal attenuation $E(\boldsymbol{p}_{pgse}; \Omega)$: [23]

$$E(\boldsymbol{p}_{pgse}; \Omega) = \frac{S(\boldsymbol{p}_{pgse}, T_E; \Omega)}{S_0(T_E)} \,, \tag{1.26}$$

such that the superposed signal becomes [23, 29]

$$E(\boldsymbol{p}_{pgse}; \Omega) = \sum_{i=1}^{K} f_i E(\boldsymbol{p}_{pgse}; \Omega_i) \,. \tag{1.27}$$

Moreover, the compartments are considered independent due to the *slow exchange limit* principle which states in the case of diffusion that *they are very few molecules transfer between compartments that occur at small time scale* ($\lesssim 100\, ms$) [23].

1.4.2 Models present in the literature

Actually, there exists two ways of modelling the brain based of the DWI signals : a structural one, that uses the superposition principle previous stated (§ 1.4.1) and tries to describe as accurately as possible the brain microstructure; and a phenomenological one, that try to infer to the signal a mathematical expression and somehow eluding the microstructure even if they provide information about the diffusion process.

Phenomenological models

The diffusion tensor imaging model (DTI) is one of the first and best known phenomenological model and is based on the resolution of the Bloch-Torrey equations (§ 1.3.3) in the case of free (Gaussian) diffusion. Such that the signal attenuation equals [23]

$$\begin{aligned} E(\boldsymbol{p}_{pgse}; \mathbb{R}^n) &\overset{isotropic}{=} e^{-b_{pgse} D} \\ &\overset{anisotropic}{=} e^{-4\pi^2 \boldsymbol{q}^T \cdot \boldsymbol{D} \cdot \boldsymbol{q}} = e^{-b_{pgse} \hat{\boldsymbol{g}}^T \cdot \boldsymbol{D} \cdot \hat{\boldsymbol{g}}} \end{aligned} \,, \tag{1.28}$$

where b_{pgse} is the commonly use b-value associated with a PGSE sequence and which is defined as[¶]

$$b_{pgse} = (\gamma G \delta)^2 (\Delta - \frac{\delta}{3}) \, . \tag{1.29}$$

Additionally $\boldsymbol{q}$ is linked to phase encoding gradient $\boldsymbol{g}$ by [23]

$$\boldsymbol{q} = \frac{1}{2\pi} \gamma \delta \boldsymbol{g} \, , \tag{1.30}$$

and $\boldsymbol{D}$ is the diffusion tensor for which the principal eigenvector gives a good indication of the fascile's principal direction.

The multi-tensor model extends the DTI model by assuming various diffusion tensors $\boldsymbol{D_i}$ corresponding to different fasciles and weights the related signal attenuation with the appropriate volume fraction (f_i) : [30, 26]

$$E_{MTM} = \sum_i f_i e^{-\frac{b}{G^2} \boldsymbol{g}^T \cdot \boldsymbol{D_i} \cdot \boldsymbol{g}} \, , \tag{1.31}$$

therefore allowing the principal direction of multiple fasciles to be characterized.

Subsequently, a refined extension is provided by the recent DIAMOND model which weights the multi-tensor signal attenuation with an additional peak-shaped Gamma probability distribution $P(\boldsymbol{D})$ defined over the set of positive-definite symmetric tensors $\boldsymbol{D}$: [27]

$$E_{DIAMOND} = \int_{\boldsymbol{D} \in \mathbb{S}_3^+} \sum_i f_i P(\boldsymbol{D}) e^{-b \boldsymbol{g}^T \cdot \boldsymbol{D} \cdot \boldsymbol{g}} d\boldsymbol{D} \, . \tag{1.32}$$

Microstructural models

As previously mentioned, the microstructural models are developed based on the superposition principle and therefore separate the MR signal into different parts. Generally most of the models consider that the overall signal is a weighted sum of signals from three main compartments : [21]

- the intra-axonal compartment Ω_1 : where the signal is generated by water molecules evolving within the axons ;
- the extra-axonal compartment Ω_2 : where the signal is generated by water molecules from outside the axons subject to isotropic or anisotropic free diffusion ;
- and the compartment Ω_3 regrouping all the outer isotropic restriction : where the signal is generated by water molecules interaction with other cellular structures (i.e. glial cells or trapped molecules).

Furthermore, for each of those independent compartments various models can be considered. The first compartment (Ω_1) can be represented using either a *stick*, a *cylinder* or a *gamma-distributed radii* model [21]. If the *stick* model, in which the axon is modelled by a cylinder with zero radius , is considered the related signal is given by [21]

$$E(\boldsymbol{p}_{pgse}; \Omega_1) = e^{-bD(\boldsymbol{n} \cdot \boldsymbol{g})^2} \, , \tag{1.33}$$

where $\boldsymbol{n}$ corresponds the principal direction of the axon. Whereas for the *cylinder* model, the cylinder radius is this time non-zero and the GPD approximation for perpendicular signal is assumed [21].[‖]

[¶] In the upcoming sections, the notation "b_{pgse}" will simply be replaced by "b" in order to lighten the notations except if any ambiguity could arise.

[‖] The expression of the signal corresponding to this model is given in the appendix A of [21].

Finally the *gamma-distributed radii* model associates to the different axons present in a fasicle radii drawn from a gamma distribution [21]

$$P(R;k,\vartheta) = \frac{R^{k-1}e^{\frac{-R}{\vartheta}}}{\Gamma(k)\vartheta^k} \,, \tag{1.34}$$

where R corresponds to the radius, k to the shape parameter, ϑ to the scale parameter and Γ to the gamma function. Additionally, $k\vartheta$ and $k\vartheta^2$ give the mean and the variance of the distribution.

The second compartment (Ω_2) is represented by the DTI model but with diverse constraints on the diffusivity tensor [21]. For the *CSF* and the *hindered* part of the compartment, the related signal is given respectively by the isotropic and anisotropic expressions : [21]

$$E(\boldsymbol{p}_{pgse};\Omega_{2i}) = e^{-bD} \,, \tag{1.35a}$$

$$E(\boldsymbol{p}_{pgse};\Omega_{2a}) = e^{-b\hat{\boldsymbol{g}}^T\cdot\boldsymbol{D}\cdot\hat{\boldsymbol{g}}} \,. \tag{1.35b}$$

where the isotropic model is also called the *ball* model. Moreover, two different models can be derived from the anisotropic part, the *zeppelin* model and the *tensor* model, considering respectively to the cases where diffusivity tensor ($\boldsymbol{D}$) has two directions (a principal one and a perpendicular one) or is considered as a full tensor : [21]

$$\boldsymbol{D} = \alpha\boldsymbol{n}\cdot\boldsymbol{n}^T + \beta\boldsymbol{I} \quad \text{, with } d_{||} = \alpha+\beta \text{ and } d_\perp = \beta \,; \tag{1.36a}$$

$$\boldsymbol{D} = d_{||}\boldsymbol{n}\cdot\boldsymbol{n}^T + d_{\perp_1}\boldsymbol{n}_{\perp_1}\cdot\boldsymbol{n}_{\perp_1}^T + d_{\perp_2}\boldsymbol{n}_{\perp_2}\cdot\boldsymbol{n}_{\perp_2}^T \,; \tag{1.36b}$$

where $\boldsymbol{n}$, $\boldsymbol{n}_{\perp_1}$ and $\boldsymbol{n}_{\perp_2}$ correspond respectively to the principal direction and the two perpendicular directions, and $d_{||}$, $d_{\perp_1}$ and $d_{\perp_2}$ are the corresponding diffusivity associated with those directions.

Finally, for the third compartment (Ω_3), four possible models can be used to represent either isotropic (i.e. due to astrocytes) or spherical (i.e. due to spherical glial cells) restriction : the *astrosticks* model, the *astrocylinders* model, the *sphere* model and the *dot* model [21]. Where the two first are modelled by cylinders with uniformly distributed orientation but with respectively zero and non-zero radii ; and the two latter by impermeable spherical boundaries with respectively non-zero radius and zero radius, which encompass water molecules that either involve within the sphere or don't move [21]. Derived expression for the signal attenuation of the *astrosticks* model and the *astrocylinders* can be found in Apprendix A of [21] ; whereas for the signal attenuation of the *sphere* model and the *dot* model, respectively the GPD approximation is assumed and is equal to 1.

Chapter 2

Synthetic DWI signals : generation - acquisition sequence - microstructure environment

This chapter gathers most of the concept that are necessary to simulate the DWI attenuation signal, and is organized as follows : in

§2.1 *The Monte-Carlo simulation framework which is used to compute the attenuation signal of our main region of interest (i.e. the extracellular space), is described. Then a brief overview of the MCF methodology is given as this was used to synthesize the signal arising from spherical pores in a few of our subsequent experiments.*

§2.2 *An overview of the custom multi-shell acquisition scheme that is generated to find one of the optimal MC simulation parameter, is provided ; together with a review of two clinically-realistic and commonly used acquisition protocols in the literature which are used to study the impact of spherical pores on the DWI signal.*

§2.3 *Details about the three microstructure environments that are investigated, are provided. The corresponding environments without pores are not directly portrayed, but can be readily extrapolated (i.e. by simply omitting the information about the spherical entities).*

2.1 Synthetic generation of DWI signals

In order to synthetically simulate the DWI attenuated signal $E(\boldsymbol{p}_{pgse};\Omega)$, the hybrid approach used in [25] is considered. In this method, the signal is composed of two superposed signals :*

(i) the first signal $E_{MC}(\boldsymbol{p}_{pgse};\Omega_{ex})$ is obtained using Monte-Carlo simulations in the extra-cell compartment Ω_{ex} ;

(ii) whereas the second signal $E_{MCF}(\boldsymbol{p}_{pgse};\Omega_{in})$ is computed based on the multiple correlation function (MCF) approach applied for the intra-cell compartment Ω_{in} ;

such that the overall attenuation signal is given by [25]

$$E(\boldsymbol{p}_{pgse};\Omega) = f_{ex}E_{MC}(\boldsymbol{p}_{pgse};\Omega_{ex}) + f_{in}E_{MCF}(\boldsymbol{p}_{pgse};\Omega_{in}) \,, \tag{2.1}$$

with f_{ex} and f_{in} being respectively the volume fraction of extra-cell compartement and of the intra-cell compartment, and respectively corresponding to $\frac{\Omega_{ex}}{\Omega_{ex}+\Omega_{in}}$ and $\frac{\Omega_{in}}{\Omega_{ex}+\Omega_{in}}$.

*The intra-cell compartment refers to the combination of the intra-axonal and the intra-pore compartments, whereas the extra-cell compartment is the remaining environment.

This approach has proven to reduce the computation time, with respect to using only MC simulations for both compartments (Ω_{ex} and Ω_{in}), for the same precision in a fixed diffusion environment [25]. Moreover, if the simulation time is fixed, the precision of the hybrid method increase with the intra-axonal volume fraction ; when this precision remain constant for the MC approach, in addition of being lower or equal to the precision of the hybrid method [25].†

Furthermore, as the aim of this master thesis is to study the impact of spherical pores in the white matter, the region of interest is the extra-axonal compartment. Therefore, the MCF approach is mainly used to compute the signal within the pores (i.e. in the intra-pore compartment) when the latter is assumed to contain water molecules.

2.1.1 Monte-Carlo simulations

MC simulations are well-suited to the microscopic approach described in § 1.3.3, as it models the spins as *random walkers* in a 3-D environment [14]. For each of this spins that are initially uniformly distributed across the environment, a trajectory is computed, and together with the PGSE sequence, is used to derive the corresponding phase and therefore the corresponding noise-free attenuation signal [14].

As the phase (1.17) is obtained by integration over a specific period of time and in order to approach it numerically, the time interval is partitioned from the application of the 90°-pulse to the echo time (T_E), such that the phase at the instance t_i for a specific spins k is equal to [14, 25]

$$\phi_k(t_i) = \gamma f(t_i) \boldsymbol{g} \cdot \boldsymbol{r}(t_i) dt_i \,, \tag{2.2}$$

with $t_i \in \{t_0 = 0, t_1, ..., t_{2\tau} = T_E\}$, with dt_i being the time step which is set to be constant and equal to $\frac{T_E}{T}$, and with T being the number of time steps. Then those phases are summed up in order to obtain the overall net phase [14]

$$\phi_k(\boldsymbol{p}_{pgse}) = \sum_{i=0}^{2\tau} \phi_k(t_i) \,, \tag{2.3}$$

such that the attenuation signal is computed as [14]

$$E_{MC}(\boldsymbol{p}_{pgse}; \Omega_{ex}) = \frac{1}{N} \sum_{k=1}^{N} e^{i\phi_k(\boldsymbol{p}_{pgse})} \,. \tag{2.4}$$

Additionally, the position $\boldsymbol{r}(t_i)$ is updated at each iteration as followed [14, 25]

$$\boldsymbol{r}(t_i) = \boldsymbol{r}(t_{i-1}) + \Delta \boldsymbol{r}_{i-1} \,, \tag{2.5}$$

where each step $\Delta \boldsymbol{r}_{i-1}$ is randomly oriented and is of fixed length [14]

$$L_{step} = \sqrt{6 D dt_i} \,. \tag{2.6}$$

Due to the central limit theorem, summing up repeatedly the randomly generated step ensures that the distribution of the position $\boldsymbol{r}(t)$ at time t converges to a Gaussian distribution, as expected from Brownian motion [14]. While computing the trajectory, if a spin encounters a barrier, it is reflected, as shown on FIGURE 2.1, due to the fact that we assume perfectly impermeable cell membranes [14]. Moreover, as *the trajectory of each spin is independent of its accumulated phase, one set of spins*

†The simulations in [25] were done considering only cylindrical axons in the environment, nevertheless, those conclusions can be readily extrapolated to an environment containing additional spherical pores.

dynamics can thus be used to compute the signals associated to several different sets of PGSE parameters $(\boldsymbol{g}, \Delta, \delta)$ [25].

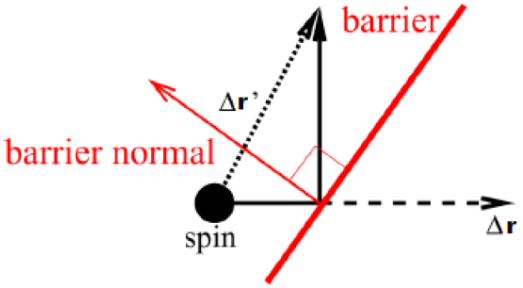

FIGURE 2.1: **Spin reflecting on an impermeable cell membrane.** Figure adapted from [14]

Under the assumptions that the studied system is isolated with time-invariant properties in which no net fluxes occur [31], which is our case, the DWI signal has been proven to be real and positive. Yielding a synthetic attenuation signal equal to [14]

$$E_{MC}(\boldsymbol{p}_{pgse}; \Omega_{ex}) = \frac{1}{N} \sum_{k=1}^{N} cos\big(\phi_k(\boldsymbol{p}_{pgse})\big) \,. \tag{2.7}$$

Finally, in order to properly generate a synthesized attenuation signal using MC simulations, three parameters have to be accordingly fixed :

(i) the environment diffusivity D, which is the subject of interest of this master thesis ;

(ii) the number T of time steps, which is discussed in § 3.1.2 ;

(iii) the number N of time steps, which is discussed in § 3.1.1.

2.1.2 Multiple correlation function approach

Here, only a quick and very succinct summary of the MCF approach is given, the reader is redirected toward [25] for a wider summary or toward [12, 13] for more precision.

In order to solve the macroscopic Bloch-Torrey PDE (1.24), Grebenkov sets up an unified mathematical framework based on the decomposition of the solution into Laplace eigenfunctions, referred to as the multiple correlation function approach [12, 13]. The attenuation signal, for a microstructural environment Ω_{in} of a certain typical length scale L_0 (i.e. the radius) and its corresponding PGSE sequence, is given by [12, 13]

$$E_{MCF}(\boldsymbol{p}_{pgse}; \Omega_{in}) = \big[\underbrace{e^{-(p\Lambda - iq\mathfrak{B})\frac{\delta}{T}}}_{\substack{\text{gradient} \\ \text{rephasing}}} \underbrace{e^{-p\frac{(\Delta-\delta)}{T}}}_{\substack{\text{pure} \\ \text{diffusion}}} \underbrace{e^{-(p\Lambda + iq\mathfrak{B})\frac{\delta}{T}}}_{\substack{\text{gradient} \\ \text{dephasing}}} \big]_{0,0} \,, \tag{2.8}$$

where $p = \frac{DT}{L_0}$ and $q = \gamma G L_0 T$ are dimensionless numbers with T being related to the typical time scale of the PGSE sequence, where exponentials are matrix exponentials on diagonal matrix Λ and symmetric matrix $\mathfrak{B}$, both of infinite dimension, and where $[\cdot]_{0,0}$ denotes the first diagonal element. In practice, only the first M terms of the eigenfunction expansion are kept [12, 13].

Finally, despite the fact that the method gives extremely accurate solution for DWI attenuation signal up to a truncation error (that is negligible with truncation parameter $M \approx 50$), the method can only applied to simple geometries such as cylinders (finite or infinite) and spheres, in which the Laplace eigenfunctions have a known analytical expression [12, 13].

2.2 Acquisition protocols

While synthetically generating the MC attenuation signal $E_{MC}(\boldsymbol{p}_{pgse};\Omega_{ex})$, using different PGSE parameter combinations $\{\boldsymbol{p}_{pgse}\}_i := (\boldsymbol{g}_i, \Delta_i, \delta_i)$ yields different measurements. Therefore, it is necessary to fix those parameters, also referred to as *acquisition protocols* or *acquisition schemes* and which can be seen as MRI machine settings. Although, there exist at least six different well-known acquisition protocols : [25, 11]

(i) HARDI-like scheme [30] ;

(ii) DTI-like scheme [5] ;

(iii) ActiveAx-like scheme [3] ;

(iv) NODDI-like scheme [34] ;

(v) DSI-like scheme [31] ;

(vi) CUSP-like schemes [26] ;

we choose to investigate only the schemes (iii) and (iv) for the study of the impact of pores on the DWI attenuation signal. Those protocols were selected as they are clinically-realistic. Whereas an additional custom multi-shell scheme is created in order to assess the MC simulation parameters. Additionally, we limited ourselves to those three protocols in order to not lengthen the simulation time. The latter behind directly proportional to the number of acquisition sequences.

The three acquisition protocols, that are used in this master thesis, are directly driven from the simpler (one-shell) HARDI-like scheme. For this scheme, the PGSE sequences are generated using a fixed b-value (i.e. G, Δ and δ being fixed for all sequences) with 90 directions uniformly distributed across a three-dimensional unitary sphere [30].

Varying the gradient intensity G, the time Δ between to two consecutive pulses or the pulse duration δ, generates M shells of different b-values. If those shells are combined to N gradient directions, a multi-shell scheme is obtained. Such that if the 90 directions of the one-shell HARDI-like scheme are used with shells of b-values generated by varying only G, we get a multi-shell HARDI-like protocol.

2.2.1 Custom multi-shell scheme

In order to assess as precisely as possible the number T of time steps for the MC simulations, we selected a PGSE profile (FIGURE 1.6) that exhibits sharp and extreme transitions ; therefore requiring smaller time steps to estimate accurately the phase. To do so, the gradient intensity G is set to its maximum achievable values, whereas the gradient duration δ is set to its smallest realistic values (i.e. highest δ reaching up to $60ms$ [31]). TABLE 2.1 summarises the values for the different shells, in which the two first values of G correspond respectively to the maximal gradient intensity that can actually be reached in a human system and in animal systems [3].

$G\,[\frac{m\mathrm{T}}{\mathrm{m}}]$	80	200	300
$\delta[ms]$	2	6	10

TABLE 2.1: **Values of the gradient intensity G and the pulse duration δ.**

Additionally, we choose to explore a wide range of b-values (TABLE 2.2) going from very small values (i.e. $50\frac{s}{mm^2}$) to extremely high values (i.e. $10000\frac{s}{mm^2}$, this value has been reached in the Human Connectome Project [11]).

$b\ [\frac{s}{mm^2}]$	50	100	200	500	1000	2000	3000	5000	10000

TABLE 2.2: **b-values composing the custom 9-shell scheme.**

Those b-values are obtained by combining together all the values of G and δ from TABLE 2.1 and by adapting Δ accordingly and always ensuring that $\Delta \geq \delta$. Such that at the end, a total of 810 acquisition sequences are generated for this custom protocol.

2.2.2 ActiveAx-like scheme

ActiveAx is a four-shell HARDI-like protocol with gradients and b-vectors distributed over spherical shells. This scheme was first designed to estimate distribution of axon diameters in the human white matter in vivo [3].

Furthermore, its 90 gradient directions and its 4 related combinations of G, Δ and δ, where determined by attempting to minimize the variance of a simple microstructural model based on the CHARMED model, using the Cramer-Rao Lower bound, while keeping sequences that are clinically realistic [4].

2.2.3 NODDI-like scheme

Similarly, NODDI is an optimized two-shell HARDI-like protocol (i.e. with two gradient intensities, and identical pulse duration δ and pulse separation time Δ) with the supplementary condition that the total number of acquisition protocols have to be limited to 90 (due to the available hardware requirements at the time) [2].

Additionally, the outer shell is sampled at twice the angular resolution of the inner shell (i.e. $N_1 = 30$ and $N_2 = 60$), because DWI signal at higher b-values are estimated to be more sensitive to complex microstructure configurations [8]. Nevertheless, two additional intermediate shells sampled respectively at 30 and 60 angular directions were afterwards added, raising the total number of acquisition sequences to 180 [34].

Finally, the scheme was first introduced to validate the three-compartment tissue model including neurite orientation dispersion [34].

2.3 Microstructure environments

Based on the three of the four types of elementary mircostructure configurations (also called *atoms*) described in [25] :

(i) **single fascicles of identical axons** modelled by infinitely long and parallel cylinders of constant radius ;

(ii) **two crossing fascicles of identical axons** modelled by two crossing sets of infinitely long and parallel cylinders respectively with constant radius ;

(iii) and **glial cells** modelled by spheres ;

three distinct microstructure environments are generated and studied. Moreover, those environments are put in perspective with their homologue environments in which the spherical pores have been removed.

The choice of modelling fascicles by infinitely long cylinders is understandable as those are much longer than thicker (i.e. the order of magnitude of their radius and their length are respectively of micrometer and millimeter or centimeter [1, 18]). Whereas the choice of spherical entities to model

glial cells is due to the fact that it fits and explains better DWI data than elaborate model attempting to reproduce the exact biological shape (i.e. *astrostick*) [21]. Additionally, from now on, the spherical *atoms* representing glial cells will be referred as pores, a more general term used in the DWI community. This choice is not only driven by semantic reason, but allows us to investigate two distinct types of microstructure : glial cells when water molecules are assumed to evolve within the pores and spherical debris when no inside water molecules are considered.

2.3.1 Single pore within a voxel

First of all, we consider a simple environment composed of spherical pores only. This configuration is chosen as a reference environment in order to study the impact of spherical entities on the DWI signals, because the corresponding environment without pores is the free environment for which an exact analytical solution exist (i.e. the free Gaussian isotropic diffusion solution).

This simple environment is characterized by the voxel length L, the radius $r_{(s)}$ of the spheres and the spacing $s_{(s)}$ between the pore and the voxel. The voxel length and the spacing are encompassed in the intra-pore volume fraction f_{in_s} and can be replaced by the latter, as they are linked by :

$$f_{in_{(s)}} = \frac{4\pi}{3}\Big(\frac{r_{(s)}}{2r_{(s)} + s_{(s)}}\Big)^3 , \tag{2.9}$$

where $L = 2r_{(s)} + s_{(s)}$. As by definition $L \geq 2r_{(s)}$, an upper bound for the intra-pore volume fraction is found when the equality holds :

$$f_{in_{(s)}} \leq \frac{\pi}{6} \approx 0.523 . \tag{2.10}$$

Subsequently, the parameters for the environment are chosen as followed :

	set 1						set 2							
$r_{(s)}$ [μm]	0.2						0.6							
$f_{in_{(s)}}$	0.0125	0.025	0.05	0.1	0.15	0.2	0.0125	0.025	0.05	0.1	0.15	0.2	0.3	0.4

TABLE 2.3: **Parameters of the spherical pores.**

Finally, another important characteristic of the environments that are studied is their typical length scale a of diffusion . This feature allows to determine the limit from which the spin dynamic undergoes Brownian motion, as discussed latter in § 3.1.2. In the case of a simple environment composed of spherical pores only, its value is given by

$$a = s_{(s)} = L - 2r_{(s)} . \tag{2.11}$$

2.3.2 Hexagonally packed fascicles of identical axons surrounded by hexagonally distributed pores

The second environment to be investigated is composed of single fascicles of identical axons that are hexagonally packed and that are surrounded by hexagonally distributed glial cells, as illustrated on FIGURE 2.2. This packing configuration has been chosen because it is the tightest packing of circle in 2D, which subsequently allow to achieve the largest intra-axonal and intra-pore volume fractions.

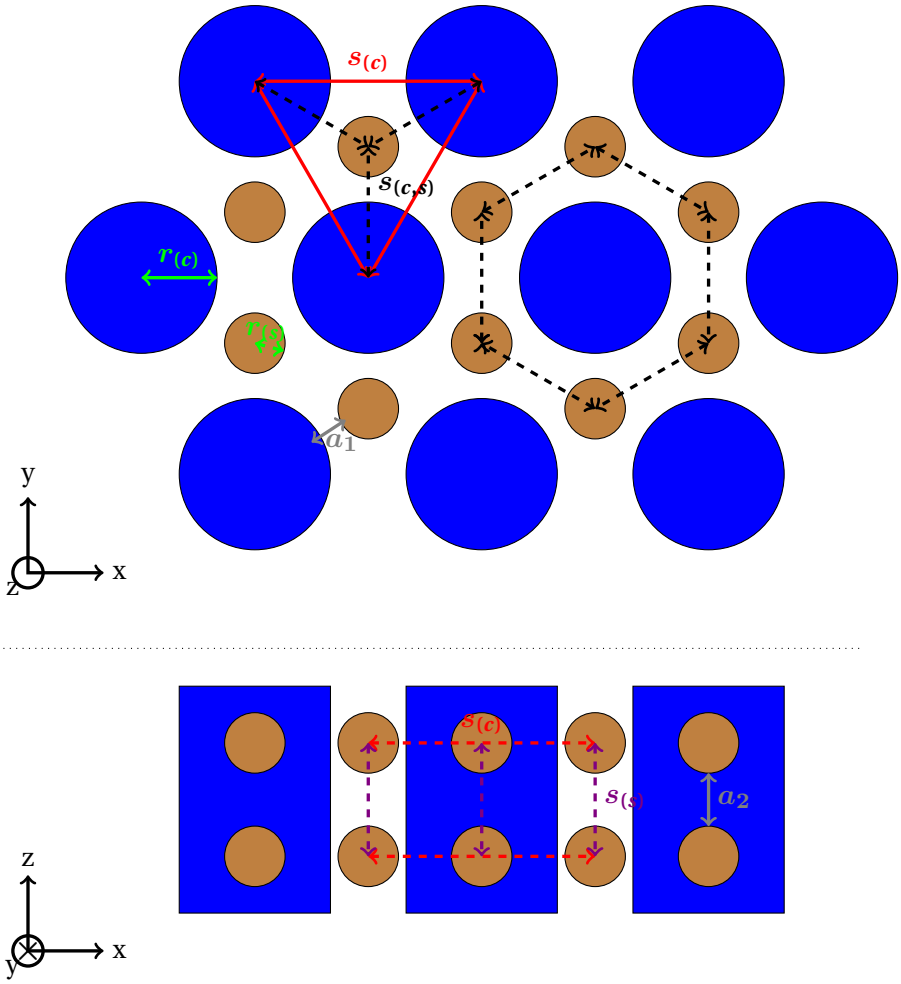

FIGURE 2.2: **Hexagonally packed fascicles of identical axons surrounded by hexagonally distributed pores.** The blue circles and the blue rectangles represent the cylindrical fascicles respectively in the xy-plane and the xz-plane, whereas the brown spheres represent the spherical pores. Moreover $s_{(c)}$ represents the separation between two adjacent cylinders, $s_{(c,s)}$ represents the separation between a sphere adjacent to a cylinder, $r_{(c)}$ represents the cylinder radius, $s_{(s)}$ represents the sphere radius, $a_1 = s_{(c,s)} - (r_{(c)} + r_{(s)})$ represents one of the candidate that could be considered as the typical length scale of diffusion, $s_{(s)}$ represents the separation between adjacent spheres in the x-direction, $s_{(s)}$ represents the separation between adjacent spheres in the z-direction, and $a_2 = s_{(s)} - 2r_{(s)}$ represents the second candidate to be considered as the typical length scale of diffusion of the environment.

This configuration is principally characterized by the radii $r_{(c)}$ and $r_{(s)}$ of respectively the cylinders and the spheres, which both can be considered as the primary parameters. Typically values for the fascile radius $r_{(c)}$ vary between 0.1 and 5 μm [1, 18], whereas there are no specific values for the radius $r_{(s)}$. However, we choose to set the latter to be smaller than the cylinder radius, as the pores represent either debris or glial cells.

Moreover, the environment is also characterized by the spacing $s_{(c)}$ between cylinders in the xy-plane and the spacing $s_{(s)}$ between spheres in the xz-plane. Nevertheless, as it is more practical to work with the intra-axonal volume fraction $f_{in_{(c)}}$ and the intra-glial volume fraction $f_{in_{(s)}}$, those are

considered as the secondary parameters and are linked to the spacings by[‡]

$$\begin{cases} f_{in_{(c)}} = \dfrac{2\pi}{\sqrt{3}}\left(\dfrac{r_{(c)}}{s_{(c)}}\right)^2 & \text{(2.12a)} \\ f_{in_{(s)}} = \dfrac{16\pi}{3\sqrt{3}}\dfrac{r_{(s)}^3}{s_{(c)}^2 s_{(s)}} & \text{(2.12b)} \end{cases}$$

Additionally, in order to have a feasible environment (i.e. to avoid any overlap), three elementary conditions must be fulfilled :

$$\begin{cases} s_{(c)} \geq 2r_{(c)} & \text{(2.13a)} \\ s_{(c,s)} \geq r_{(c)} + r_{(s)} & \text{(2.13b)} \\ s_{(s)} \geq 2r_{(s)} & \text{(2.13c)} \end{cases}$$

where $s_{(c,s)}$ corresponds to the spacing between a fascile and an adjacent glial cell.

Considering that the cylinders are fully-packed (i.e. $s_{(c)} = 2r_{(c)}$), a mathematical upper bound can be found for the intra-axonal volume fraction :[§]

$$f_{in_{(c)}} \leq \frac{\pi}{2\sqrt{3}} \approx 0.907\,; \tag{2.15}$$

such that the intra-glial volume fraction is therefore bounded by

$$f_{in_{(s)}} \leq \frac{2\pi(2-\sqrt{3})^2}{9\sqrt{3}} \approx 0.029\,. \tag{2.16}$$

As configuration using only fascicles have been extensively studied in the literature, mainly the parameters concerning the spheres are investigated. Therefore, we only choose two sets of values for the cylinders radius $r_{(c)}$ and the intra-axonal volume fraction $f_{in_{(c)}}$:

	set 1	set 2
$r_{(c)}$ [μm]	1	2
$f_{in_{(c)}}$	0.71	0.60

TABLE 2.4: **Parameters of the cylindrical axons.**

Where the first set represents the most representative values of the human white matter tissue [14] and yields a upper bound of 0.088 for the intra-pore volume fraction $f_{in_{(s)}}$.[¶] On the other hand, the second set is chosen in order to allow more spacing between the axons (i.e. allowing therefore to reach higher intra-pore volume fractions : the upper bound reaches now 0.141) and has cylinder parameters that do not depart too much from the typical values of set 1. The upper bounds and the variation for the intra-pore volume fraction, for both sets, are depicted on FIGURE 2.3.

[‡]Details about how those fractions are obtained are given in Appendix A.

[§]The bound for $f_{in_{(c)}}$ is directly found by substitution ; whereas for $f_{in_{(s)}}$ the following relations between $s_{(c,s)}$, $r_{(c)}$, $r_{(s)}$ and $s_{(c)}$ must be used :

$$\left.\begin{aligned} s_{(c,s)} &= r_{(c)} + r_{(s)} \\ &= \frac{s_{(c)}}{\sqrt{3}} \end{aligned}\right\} \overset{s_{(c)}=2r_{(c)}}{\Rightarrow} r_{(s)} = \frac{2-\sqrt{3}}{\sqrt{3}} r_{(c)}\,. \tag{2.14}$$

[¶]This maximal value of $f_{in_{(s)}}$ is found by substituting (2.12a) into (2.12b), by considering (2.14), and the fixed value for $r_{(c)}$ and $f_{in_{(c)}}$.

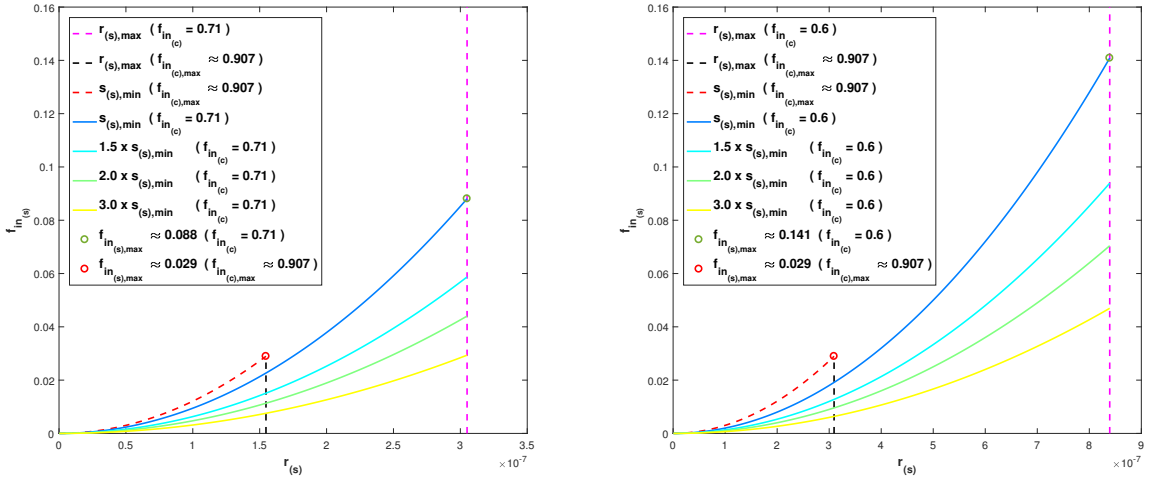

(A) $r_{(c)} = 1\mu m$ (B) $r_{(c)} = 2\mu m$

FIGURE 2.3: **Variation of the intra-pore volume fraction in function of radius of the pores, for the hexagonally packed fascicles of identical axons surrounded by hexagonally distributed pores.** Where the graph (A) correspond to the first set , while the graph (B) correspond to the second set. On both graphs, we can notice clearly the maximal radius $r_{(s),max}$ that can be reached for each set. As expected, this radius values is higher for the second set (A) for which the extra-axonal volume fraction is higher. Moreover, we see that the upper limit of the intra-pore volume fraction $f_{in_{(s)}}$ decreases when the spacing $s_{(s)}$ between the spherical pores along the z-direction increases.

With respect to those sets, the parameters of the pores are fixed as follow :

	set 1				set 2			
$r_{(s)}$ [μm]	0.2				0.6			
$f_{in_{(s)}}$	0.005	0.015	0.02	0.03	0.015	0.03	0.04	0.06

TABLE 2.5: **Parameters of the spherical pores.**

Although higher intra-pore volume fractions can be reached, we limit ourselves to those values as those combinations of microstructural parameters yields more suitable simulation parameters : other combinations urging us to use extremely high number T of time steps in order to fulfil the Brownian condition.

Finally, the typical length scale of diffusion of the environment necessary to determine the Brownian behaviour is given by

$$a = min\{a_1\ ,\ a_2\} = min\{s_{(c,s)} - (r_{(c)} + r_{(s)})\ ,\ s_{(s)} - 2r_{(s)}\}\ . \tag{2.17}$$

2.3.3 Crossing fascicles of identical axons surrounded by rectangularly distributed pores

Two sets of crossing fascicles, surrounded respectively by four pores arranged in a rectangular manner, compose the second environment to be investigated, as portrayed on FIGURE 2.4. This configuration has been designed such that when the two fascicles are parallel to one another (i.e. their crossing angle is zero) and when the spacing $s_{(c,c)}$ between adjacent cylinders of different fascicles is equal to the spacing $s_{(c)}$ between cylinders of the same population, the pseudo-hexagonal packing is found back.

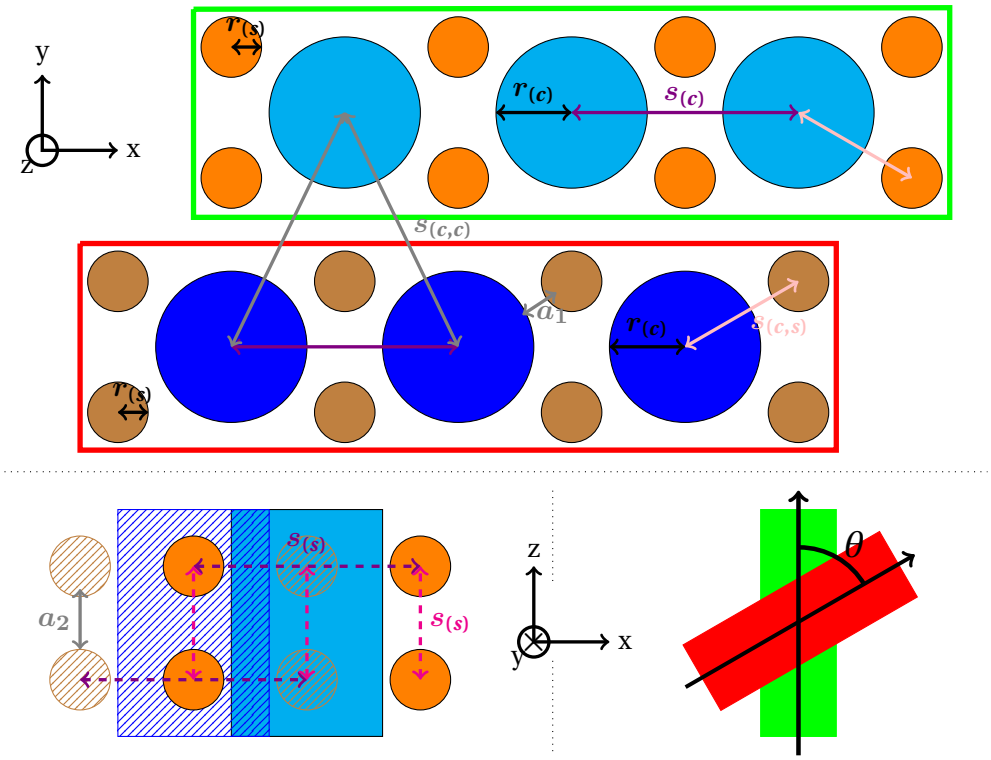

FIGURE 2.4: **Crossing fascicles of identical axons surrounded by rectangularly distributed pores.** The lighter blue circles as well as the filled rectangle represent the cylindrical fascicles, and the orange circles represent the spherical pores, in the first population ; whereas the darker blue circles as well as the hashed rectangle represent the cylindrical fascicles, and the brown circles represent the spherical pores, both in the second population. Additionally, the upper representation and the one below on the left side are drawn without considering any rotation. This rotation between the two populations of fascicles with their respective pores is shown on the bottom right side. As for the previous environment, $s_{(c)}$ represents the separation between two adjacent cylinders, $s_{(c,s)}$ represents the separation between a sphere adjacent to a cylinder, $r_{(c)}$ represents the cylinder radius, $s_{(s)}$ represents the sphere radius, $a_1 = s_{(c,s)} - (r_{(c)} + r_{(s)})$ represents one of the candidate that could be considered as the typical length scale of diffusion, $s_{(s)}$ represents the separation between adjacent spheres in the x-direction, $s_{(s)}$ represents the separation between adjacent spheres in the z-direction, and $a_2 = s_{(s)} - 2r_{(s)}$ represents the second candidate to be considered as the typical length scale of diffusion of the environment. Finally, the pore positions were chosen so the are equally spaced with respect to their adjacent fascicles.

As for the second environment, mainly the sphere parameters are studied, such that the cylinders radius $r_{(c)}$ and the intra-axonal volume fraction $f_{in_{(c)}}$ have been fixed to the same values (TABLE 2.4). Moreover, as the two populations of fascicles are assumed to have identical axons, those values are equal in both cases. Subsequently, the spacing $s_{(c,c)}$ between adjacent cylinders of the different populations is fixed to be equal to $\frac{\sqrt{5}}{2}s_{(c)}$, such that its projection on the y-axis is equal to $s_{(c)}$.[‖] Therefore, the remaining parameters that characterize this environment are the spheres radius $r_{(s)}$, the spacing $s_{(s)}$ between the spheres along the principal direction and the rotation angle θ. Similarly to the hexagonal packing configuration, the spacings are linked to the volume fractions by

$$\begin{cases} f_{in_{(c)}} = \pi\left(\dfrac{r_{(c)}}{s_{(c)}}\right)^2 & \text{(2.18a)} \\ f_{in_{(s)}} = \dfrac{8\pi}{3}\dfrac{r_{(s)}^3}{s_{(c)}^2 s_{(s)}} & \text{(2.18b)} \end{cases}$$

In order to have a feasible environment, the configuration must also fulfil the elementary conditions

[‖]The latter is mainly a design choice and don't necessary have a physical base.

in (2.13). Subsequently, the most compact configuration admits, for intra-axonal volume fraction, the following upper bound :**

$$f_{in_{(c)}} \leq \frac{\pi}{4} \approx 0.785\,; \tag{2.19}$$

such that the intra-glial volume fraction is therefore bounded by

$$f_{in_{(s)}} \leq \frac{\pi}{3}\left(\frac{2-\sqrt{3}}{\sqrt{3}}\right)^2 \approx 0.025\,. \tag{2.20}$$

As for the previous environment composed of fascicles, we use the same sets of values (TABLE 2.4) for the cylinders radius r_c and the intra-axonal volume fraction $f_{in_{(c)}}$. This also increase the upper bound for the intra-pore volume fraction $f_{in_{(s)}}$ to 0.083 in the first set and to 0.114 in the second set, as shown on FIGURE 2.5. Finally, we also use the same parameters (TABLE 2.5) for the pores as for the second environment and the typical length scale is chosen according to (2.17).

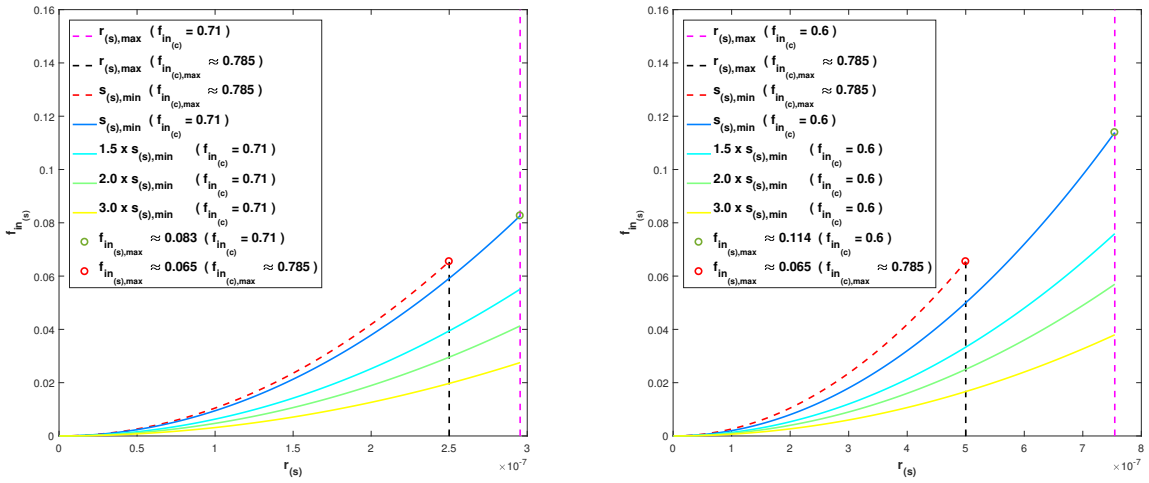

(A) $r_{(c)} = 1\mu m$ (B) $r_{(c)} = 2\mu m$

FIGURE 2.5: **Variation of the intra-pore volume fraction in function of radius of the pores, for the crossing fascicles of identical axons surrounded by rectangularly distributed pores.** Where the graph (A) correspond to the first set , while the graph (B) correspond to the second set. On both graphs, we can notice clearly the maximal radius $r_{(s),max}$ that can be reached for each set. As expected, this radius values is higher for the second set (A) for which the extra-axonal volume fraction is higher. Moreover, we see that the upper limit of the intra-pore volume fraction $f_{in_{(s)}}$ decreases when the spacing $s_{(s)}$ between the spherical pores along the z-direction increases.

**The bounds $f_{in_{(c)}}$ and $f_{in_{(s)}}$ are found in the same manner as for the hexagonal packing.

Chapter 3

Analysis of the impact of pores on the DWI signal

This chapter covers all the results obtained simulating the attenuation signal, going from the study of the MC simulation parameters to the study of the effective diffusivity ; and is organized as follows : in

§1.1 *Based on a procedure similar to the one used in [14], we determine the optimal MC simulation parameters that must be used in the following studies. Although the determination is done for the commonly used diffusivity, the corresponding parameters are extrapolated for other diffusivity.*

§1.2 *We compare attenuation signals for three pairs of microstructure environment by considering their MC signals, their signals when pores are considered to be empty and their signals when pores are assumed to be filled with water molecules.*

§1.3 *By varying the diffusivity of the environments without pores, we determine the effective extracellular diffusivity that is necessary to obtain signals with equivalent restriction.*

3.1 Determination of the Monte-Carlo simulation parameters *

The accuracy and the precision of MC simulations is function of the number N of spins and the number T of time steps used to simulate the attenuation signal. Increasing N leads to more precision, as it decreases the statistical standard deviation between the sets of simulated signals ; while increasing T leads to more accuracy, as it decreases the time step used to compute the integral of the phase. Nevertheless, both parameters cannot be increased definitively as we must keep tractable computation times ; therefore, a trade-off must be found.

In [14], the authors suggested that trading off the number T of updates in favour of the number N of spins (i.e. $T = 10^3$ and $N = 10^5$), optimizes both the precision and the accuracy of the signal. They reach this conclusion by scrutinizing various combinations of the product U = NT, which is a measure of the complexity of the simulations. Subsequently, the optimal combination is found by seeking *the configuration that minimizes the standard deviation of signals synthesized from sets of simulations while maintaining approximate agreement with the analytical model* used to asset the accuracy [14].

Nevertheless, as conjectured in [25], the number T of time steps is at least more important than

*Although we discuss the parameter settings in both the hexagonal packing and the crossing fasciles environment, we only show the result for the hexagonal packing environment, in order to not overcrowd the section with figures and as the conclusion are strictly similar. The figures for the crossing environment can be found in Appendix B.

suggested in [14] or as much important as the number N of spins. This can be understood by considering the mean square error of a MC signal $E_{MC}(\boldsymbol{p}_{pgse};\Omega)$:[†]

$$\begin{aligned} MSE_{(MC)} &= \mathbb{E}\Big[\big(E_{MC}(\boldsymbol{p}_{pgse};\Omega) - E(\boldsymbol{p}_{pgse};\Omega)\big)^2\Big] \\ &= \underbrace{var\Big(E_M(\boldsymbol{p}_{pgse};\Omega)\Big)}_{\propto \frac{1}{\sqrt{N}}} + \underbrace{Bias\Big(E_{MC}(\boldsymbol{p}_{pgse};\Omega)\ ,\ E(\boldsymbol{p}_{pgse};\Omega)\Big)}_{\propto T}, \end{aligned} \tag{3.1}$$

where $\mathbb{E}\Big[\cdot\Big]$ denotes the expectation, where $E(\boldsymbol{p}_{pgse};\Omega)$ is the really measured signal, where $var\Big(E_M(\boldsymbol{p}_{pgse};\Omega)\Big)$ is the variance of the MC signal and $Bias\Big(E_{MC}(\boldsymbol{p}_{pgse};\Omega)\Big)$ is the bias between the really measured signal and the MC signal. This expression shows us that the mean square error is influenced by both the variance (hence the number N of spins) and the bias (hence the number T of time steps).

Furthermore, the parameter T should be investigated with respect to the total duration time (i.e. T_E) of each acquisition protocol, as the ratio of the latter to the former (i.e. $dt_i = \frac{T_E}{T}$) impacts the step length L_{step} (2.6) (i.e. therefore the Brownian motion of the spins) and the accuracy of the quadrature for the integral.

Then, in order to determine the optimal MC parameters for our simulations, we proceed to an analysis of the variance and the "bias" of the generated signals for different number N of spins and number T of time steps (TABLE 3.1). Those studies are done for two "representative" environments (TABLE 3.2) and the results are then extrapolated for the other environments. Furthermore, the signals are computed 30 times using a different random seed at each simulation (i.e. in order to have statistically relevant data) and using the custom multi-shell protocol described in § 2.2.1 (i.e. yielding 810 signals per simulation).

Finally, in order to be able to compare our parametric study with the one in [14], the MC simulations are done using a diffusivity value D equal to $2 \times 10^{-9}\,\frac{m^2}{s}$.

	Standard deviation study				Bias study							
N	10^2	10^3	10^4	10^5	1.5×10^4							
T	2×10^4				10^2	10^3	10^4	2×10^4	5×10^4	10^5	5×10^5	10^6

TABLE 3.1: **Simulation parameters investigated for the MC simulations.** For each of the study, one of the parameters had to be fixed, we choose to fix those parameters according to the optimal values determined in [14] : the number T of time steps in the standard deviation study was fixed to 2×10^4 (ten times higher than the one used in [14], i.e. $T = 10^3$), while the number N of spins in the bias study was fiex to 1.5×10^4 (ten times lower than the one used in [14], i.e. $N = 10^5$).

	$r_{(c)}$ $[\mu m]$	$fin_{(c)}$ [-]	$r_{(s)}$ $[\mu m]$	$fin_{(s)}$ [-]	θ [°]
hexagonal packing	1	0.71	0.2	0.03	-
crossing	1	0.71	0.2	0.03	67.5

TABLE 3.2: **Environment parameters investigated for the MC simulations.**

[†]The last equality is found by adding and subtracting $\mathbb{E}\Big[E_{MC}(\boldsymbol{p}_{pgse};\Omega)\Big]$, grouping the terms, developing the expectation, and considering that $\mathbb{E}\Big[E_{MC}(\boldsymbol{p}_{pgse};\Omega)\Big] - E(\boldsymbol{p}_{pgse};\Omega)$ is constant, as well as $\mathbb{E}\Big[E_{MC}(\boldsymbol{p}_{pgse};\Omega)\Big]$.

3.1.1 Standard deviation study

Methodology

Due to the fact that the DWI signal is function of the spin position $\boldsymbol{r}(t)$ which is a random variable for which the probability density function converges toward a Gaussian distribution (§ 2.1.1), the DWI signal is also a random variable converging toward a Gaussian distribution. So that, a theoretical standard deviation σ_E can be defined for the attenuation signal :

$$\begin{aligned}\sigma_E(\Omega) &= \sqrt{var\Big(E(\boldsymbol{p}_{pgse};\Omega)\Big)} = \sqrt{var\Big(\frac{1}{N}\sum_{k=1}^{N} cos\big(\phi_k(\boldsymbol{p}_{pgse})\big)\Big)} \\ &= \sqrt{\frac{1}{N^2}\sum_{k=1}^{N} var\Big(cos(\phi_k(\boldsymbol{p}_{pgse}))\Big)} = \sqrt{\frac{var\Big(cos\big(\phi_k(\boldsymbol{p}_{pgse})\big)\Big)}{N}} = \frac{\sigma_c(\Omega)}{\sqrt{N}}\,,\end{aligned} \tag{3.2}$$

where $var(\cdot)$ refers to the variance and where σ_c is the standard deviation of the cosinus of the spin phase. The latter, in the case of free diffusion, is given by [23]

$$\begin{aligned}&\sigma_c(FD) = \sqrt{\frac{var_c(FD)}{N}} \\ &\text{with } var_c(FD) = \frac{1}{2} + \frac{1}{2}e^{-4bD} - e^{-2bD}\,.\end{aligned} \tag{3.3}$$

Furthermore, as illustrated on FIGURE 3.1, we see that the variance in the case of free water molecule diffusion is bounded by 0.5 and that it decreases with the decrementing values of diffusivity. The last observation implying that the variance (hence the standard deviation) of the signals generated in an environment subject to more restriction (i.e. in pore-added environments) should exhibit a lower variance (hence standard deviation).

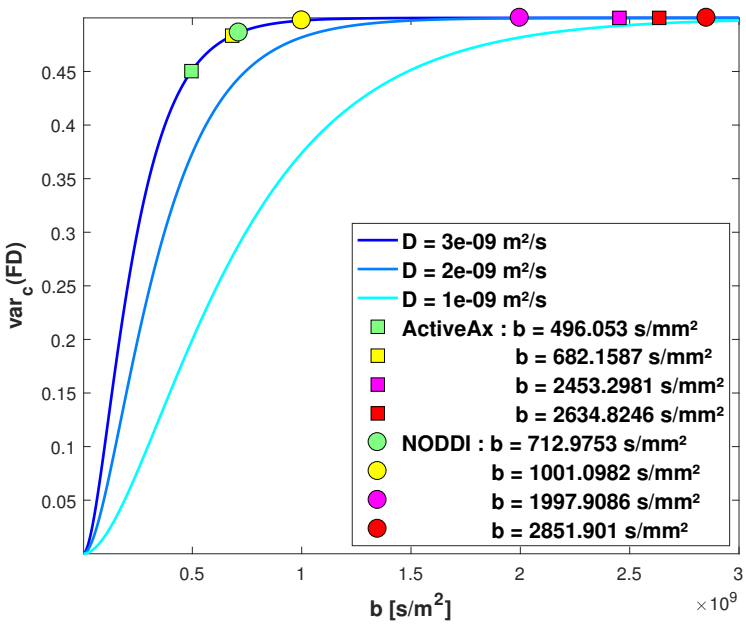

FIGURE 3.1: **Variation of the free water molecule diffusion variance in function of the b-values.** Moreover, we pick point the variance of the b-values used in the ActiveAx-like scheme and in the NODDI-like scheme with respect to the intrinsic extracellular diffusivity (i.e. $3 \times 10^{-9}\,\frac{m^2}{s}$).

On the other hand, the empirical standard deviation of each generated attenuation signal i is computed as follow :

$$std_i = \sqrt{\frac{1}{S}\sum_{n=1}^{S}\left(E_{MC,n}(\boldsymbol{p}_{pgse,i};\Omega_{ex}) - \bar{E}_{MC}(\boldsymbol{p}_{pgse,i};\Omega_{ex})\right)^2} \tag{3.4}$$

with $\bar{E}_{MC}(\boldsymbol{p}_{pgse,i};\Omega_{ex}) = \frac{1}{S}\sum_{i=1}^{S} E_{MC,n}(\boldsymbol{p}_{pgse,i};\Omega_{ex})$ being the mean of the signal, S being the number of random seed (i.e. 30), and $i \in [1:810]$.

Results and discussion

As discussed in the previous section, as already shown in [14, 25] and as illustrated by FIGURE 3.3, we can see that the standard deviation decreases with an increasing number of spins and that this decrease is proportional to $\sqrt{\frac{1}{N}}$. Additionally, this improvement in the standard deviation is portrayed differently in FIGURE 3.2, where we notice that the signal gets smoother with increasing values of N. At the same time, we can see that the signal obtained in our environment is always higher than the signal obtained in the case of isotropic free diffusion, independently of the direction ; which was expected as the spins are subjected to more restriction in our environments.

Nevertheless, as discussed in the previous section, all the standard deviation of the synthetic signals obtained using MC simulations should always be lower than the standard deviation of the signal in the case of free diffusion, which is not the case for 25% of our signals. Furthermore, on FIGURE 3.5, we can see that this phenomenon is mainly independent of the gradient direction, but occurs for (extremely) high b-values. This can be understood by considering FIGURE 3.4, where we notice that due to the fact that the b-value is extremely high, the attenuation signal is very low (i.e. near zero) and that from time to time the signal becomes negative. The latter observation might be the cause that 25% of our data exhibit higher standard deviation, as negative attenuation signals should never occur for a DWI signal. Finally, those negative values are certainly caused by the lack of precision for such low values, which is mainly due to numerical truncation error ; as even for a number T of time step equal to 10^6, we still notice negative signal values for higher b-values, as depicted on FIGURE 3.8.

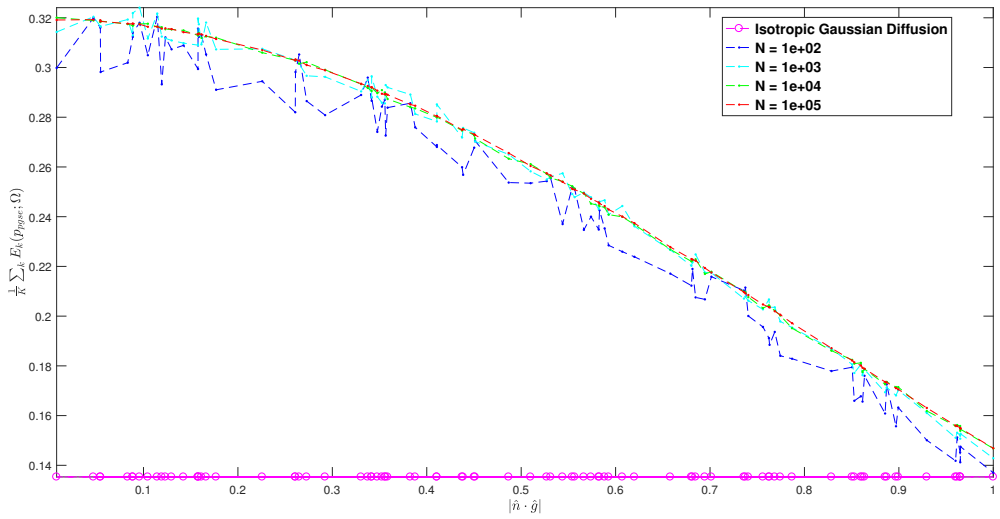

FIGURE 3.2: **Attenuation signal in function of the z-component of the gradient direction $\hat{g}$ for various number N of spins and for a b-value of $1000\frac{s}{mm^2}$ using a number T of time steps fixed to 2×10^4.**

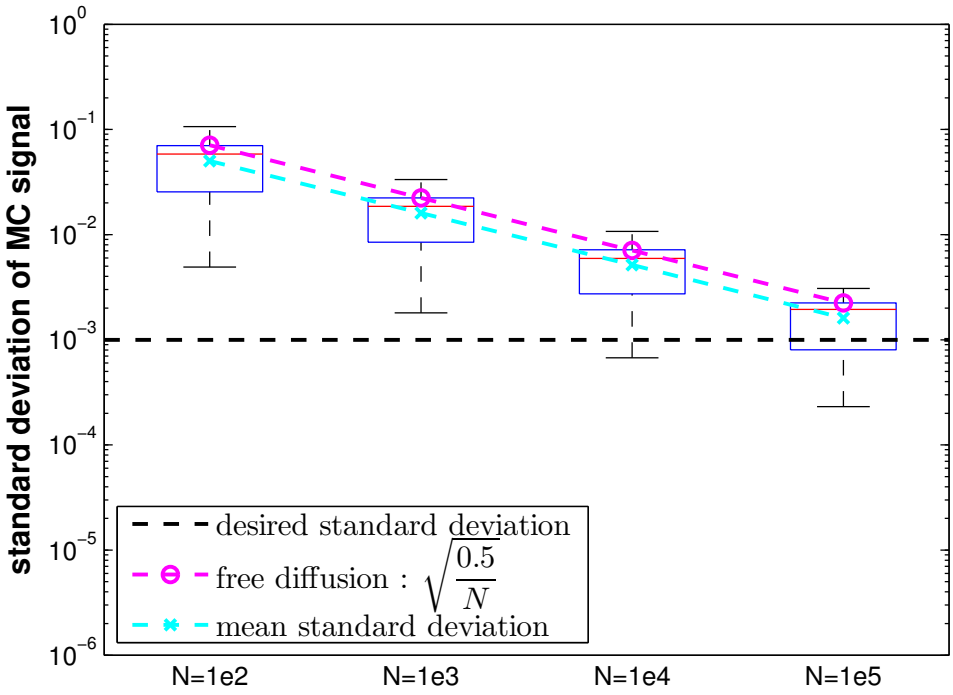

FIGURE 3.3: **Variation of the standard deviation in fonction of the number** N **of spins using a custom multi-shell scheme for the hexagonal packing environment and with the number** T **of time steps fixed to** 2×10^4**.** Each boxplot is generated based on the standard deviation computed for the 810 signals of the custom multi-shell protocol.

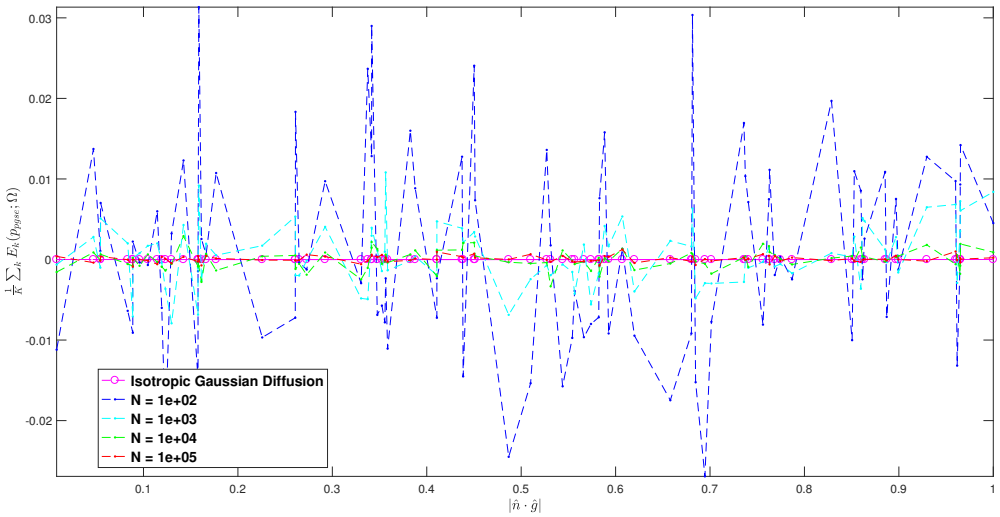

FIGURE 3.4: **Attenuation signal in function of the** z**-component of the gradient direction** $\hat{g}$ **for various number** N **of spins and for a b-value of** $10000\,\frac{s}{mm^2}$**.**

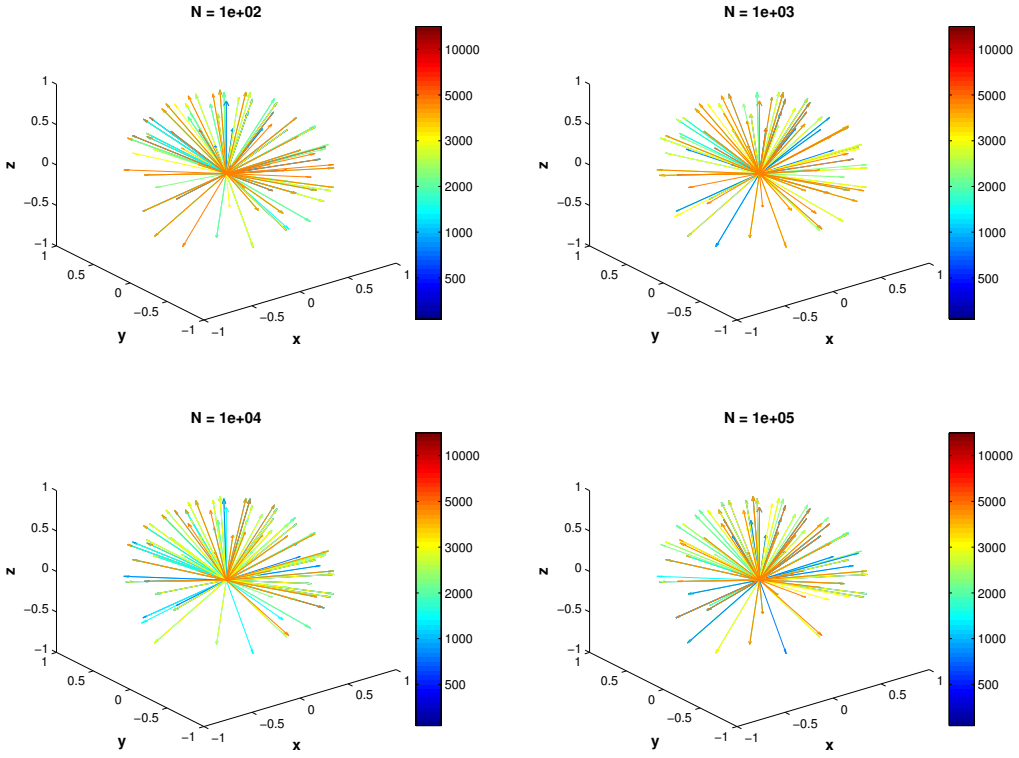

FIGURE 3.5: **Representation of the b-vectors that yield a standard deviation higher than the standard deviation of the free diffusion for the hexagonal packing environment.** The colorbar represents the intensity of the b-values, whereas the arrows represent their gradient directions.

3.1.2 Bias study

Lacking a ground-truth analytical model to compare our MC simulations data to, the study of the bias is done by investigating the absolute difference between the signals generated with the highest computationally reasonable number T of time steps, with the signals computed with lower T :

$$Bias_{i,n} = \left| E_{MC}(\boldsymbol{p}_{pgse,i}; \Omega_{ex})_{T_n} - E_{MC}(\boldsymbol{p}_{pgse,i}; \Omega_{ex})_{T_{MAX}} \right| , \tag{3.5}$$

where i denotes i^{th} generated signals, n indicates which number T of time steps is considered and T_{MAX} is the maximal number T of time steps that we have investigated (i.e. 10^6).

As expected, the bias decreases as the number T of time steps increases, as portrayed on FIGURE 3.6. Nevertheless, this increase in accuracy seems to stagnate when T reaches 50000. Additionally, if we consider the optimal number of time steps of 10^3 proposed in [14], we see that for at least 50% of the synthetic signal the bias is higher then 10^{-2}. This is emphasized by FIGURE 3.7 where we clearly see that for T lower than 10^4, the computed signals drastically diverge from the "true" signals.

Additionally, we notice, on FIGURE 3.6, that in order to still have a Brownian behaviour, T must be at least equal to 60318 or 100384, if respectively the NODDI or the ActiveAx protocol is used, for the hexagonal packing environment. Those values yield a time step dt equal to $0.91\mu s$, so that the step length L_{step} is equal to the typical length scale a of the diffusion of the environment, as shown in TABLE 3.3. This step length is the upper limit necessary to have a Brownian motion :

$$L_{step} \leq a = 0.23nm \, . \tag{3.6}$$

	T	T_E $[ms]$	dt $[\mu s]$	L_{step} $[\mu m]$
ActiveAx	100384	92	0.91	0.23
NODDI	60318	55.3	0.91	0.23

TABLE 3.3: **Time step dynamic of the environment composed of hexagonally packed fascicles of identical axons surrounded by hexagonally distributed pores, using the first set of environment parameters.** Where T represents the number of time step, T_E represents the echo time which is equal to $\Delta + \delta$, $dt = \frac{T_E}{T}$ represents the time step, and L_{step} represents the step length.

Similarly, for the crossing fasciles environment, the time step dynamic values are as found in TABLE 3.4 and illustrated on FIGURE B.4.

	T	T_E $[ms]$	dt $[\mu s]$	L_{step} $[\mu m]$
ActiveAx	121173	92	0.76	0.15
NODDI	72835	55.3	0.76	0.15

TABLE 3.4: **Time step dynamic of the environment composed of crossing fascicles of identical axons surrounded by rectangularly distributed pores, using the first set of environment parameters.** Where T represents the number of time step, T_E represents the echo time which is equal to $\Delta + \delta$, $dt = \frac{T_E}{T}$ represents the time step, and L_{step} represents the step length.

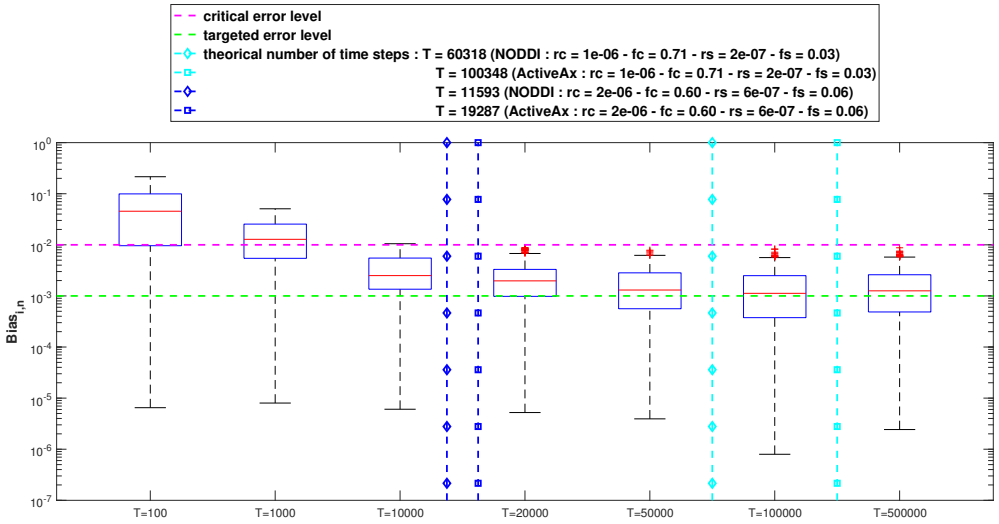

FIGURE 3.6: **Variation of the bias in fonction of the number** T **of time steps using a custom multi-shell scheme for the hexagonal packing environment and with the number** N **of spins fixed to** 1.5×10^4**.**

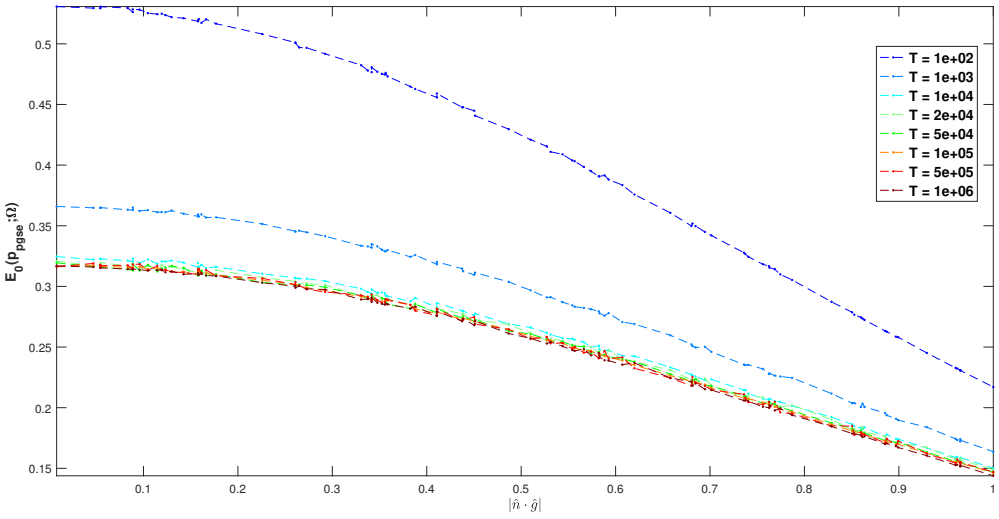

FIGURE 3.7: **Attenuation signal in function of the** z**-component of the gradient direction** $\hat{g}$ **for various number** T **of time steps and for a b-value of** $1000 \frac{s}{mm^2}$ **using a number** N **of spins fixed to** 1.5×10^4**.**

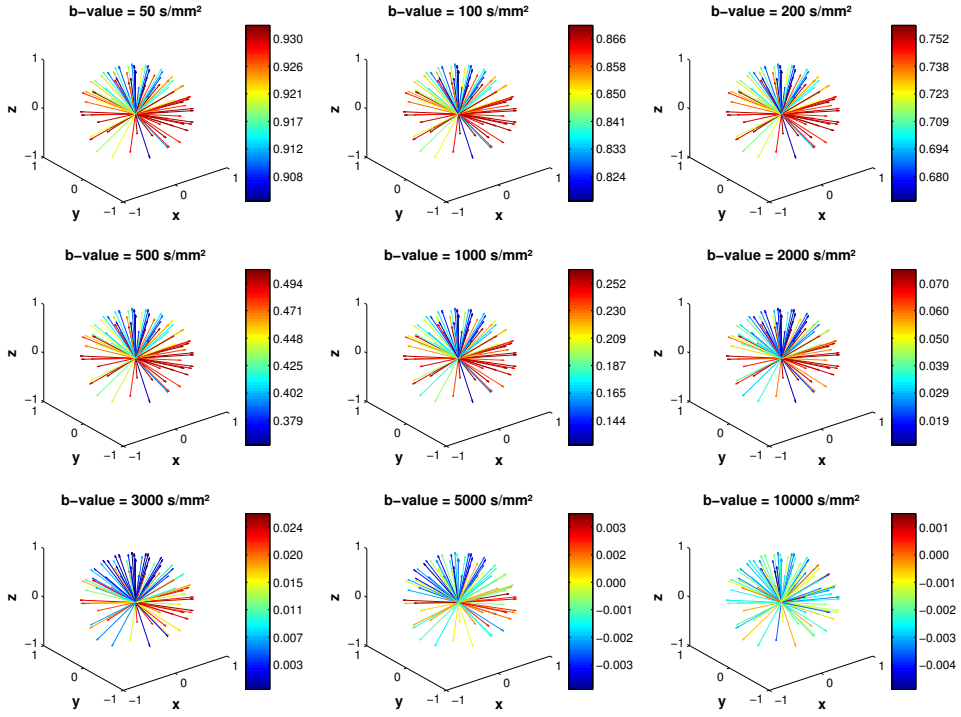

FIGURE 3.8: **Attenuation signal in function of the gradient direction $\hat{g}$ for various b-values and for the hexagonal packing environment, using a number N of spins equal to 1.5×10^4 and a number T of time steps equal to 10^6.** The colorbar represents the intensity of the attenuation signal, whereas the arrows represent the gradient directions of the b-vectors. Moreover, the negative signal attenuation, observed for high b-values (i.e. $5000 \frac{s}{mm^2}$ and $1000 \frac{s}{mm^2}$) are due to numerical truncation errors, as the computed signals are really low.

3.2 Comparison of the DWI signals

Based on the observations drawn from § 3.1, the MC simulation parameters are fixed to the values found in TABLE 3.5 for the following studies.

	ActiveAx-like scheme	NODDI-like scheme
N	10^6	10^6
T	3×10^5	1.5×10^5
U	3×10^{11}	1.5×10^{11}
dt [μs]	0.306	0.368
L_{step} [μm]	0.074	0.082

TABLE 3.5: **Simulation parameters for the MC simulations of the attenuation signals used in the comparison study (using a diffusivity equal to $3 \times 10^{-9} \frac{m^2}{s}$), together with the corresponding complexity U and time step.** Those parameters were determined based on the standard deviation and bias analysis performed on the hexagonally packed and crossing fasciles of identical axons environment. Although, those analysis were done using a diffusivity equal to $2 \times 10^{-9} \frac{m^2}{s}$. Using the latter diffusivity, the optimal parameters were initially (N ; T) = (10^6 ; 2×10^5) for the ActiveAx-like scheme and (N ; T) = (10^6 ; 1×10^5) for the NODDI-like scheme. However, if the diffusivity is modified, the number T of time steps must be adapted in order to keep Brownian motion. Therefore, the ratio $\xi = \frac{DT_E}{T}$ was defined for each protocol and was kept constant, such that when the diffusivity was increased by a factor 0.5, the time step was also incremented by the same factor.

For the first study, we choose to compare the signals obtained with three environments of section 2.3 to the signals obtained with their homologous environments that do not contains any pores, as illustrated on FIGURE 3.9. For each environment, we use the corresponding microstructure environment parameters given in TABLES 2.3, 2.4 and 2.5, and we fix the rotation angle θ of the crossing fasciles environment to 67.5°.

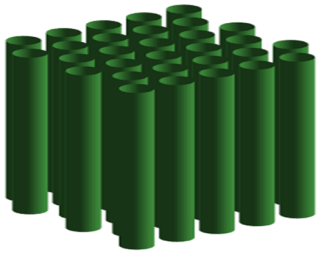

(A) **Hexagonally packed fasciles of identical axons without pores.**

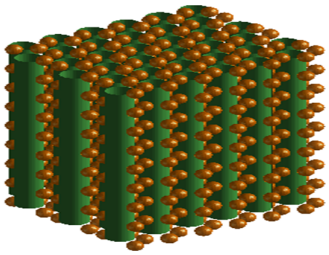

(B) **Hexagonally packed fasciles of identical axons with pores.**

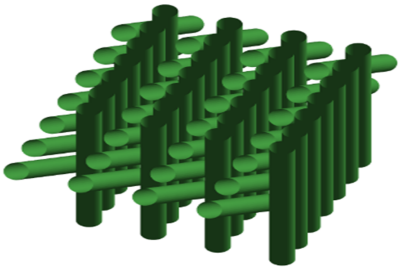

(C) **Crossing fasciles of identical axons without pores.**

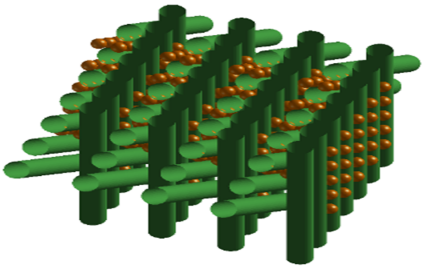

(D) **Crossing fasciles of identical axons with pores.**

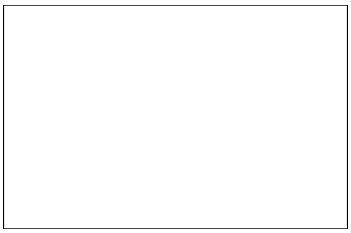

(E) **Free diffusion.**

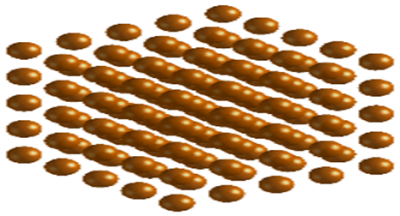

(F) **Pores only.**

FIGURE 3.9: **Illustration of the environments used in the comparison study and to determine the effective extracellular diffusivity.** On the right-hand side, the three environments discussed in § 2.3 are found , whereas on the left-hand side their homologous environments without pores are illustrated.

Comparison is done based on the MC attenuation signals computed for each pair (3.7a), and also on based on the total signals when the pores are assumed without inner water (3.7b) and filled with water molecules (3.7c) :

$$E_{MC}(\boldsymbol{p}_{pgse};\Omega_{ex,CYL}) \quad VS \quad E_{MC}(\boldsymbol{p}_{pgse};\Omega_{ex,SPH})\ ; \tag{3.7a}$$

$$f_{ex_{(CYL)}} \times E_{MC}(\boldsymbol{p}_{pgse};\Omega_{ex,CYL}) \quad VS \quad f_{ex_{(SPH)}} \times E_{MC}(\boldsymbol{p}_{pgse};\Omega_{ex,SPH})\ ; \tag{3.7b}$$

$$f_{ex_{(CYL)}} \times E_{MC}(\boldsymbol{p}_{pgse};\Omega_{ex,CYL}) \quad VS \quad f_{ex_{(SPH)}} \times E_{MC}(\boldsymbol{p}_{pgse};\Omega_{ex,SPH}) + f_{in_{(s)}} \times E_{MCF}(\boldsymbol{p}_{pgse};\Omega_{ex,SPH})\ ; \tag{3.7c}$$

with $E_{MC}(\boldsymbol{p}_{pgse};\Omega_{ex,CYL})$ and $E_{MC}(\boldsymbol{p}_{pgse};\Omega_{ex,SPH})$ being respectively the MC signal in the environment without and with spherical pores, and $f_{ex_{(CYL)}} = 1 - f_{in_{(c)}}$ and $f_{ex_{(SPH)}} = 1 - f_{in_{(c)}} - f_{in_{(s)}}$ corresponding to the extra-cell volume fraction in the respective environments.

As we can see from the set of compared signals in (3.7a), (3.7b) and (3.7c), the intra-axonal signal is not considered at all. This choice is made, as our region of interest is the extra-axonal compartment and as this signal is identical for both environments of the same pair. Subsequently, when results should be given in function of the intra-pore volume fraction $f_{in_{(s)}}$, we give those results instead in function of

the relative intra-pore volume fraction

$$f_{in_{(s,rel)}} = \frac{f_{in_{(s)}}}{1 - f_{in_{(c)}}}\,, \tag{3.8}$$

which better captures the space occupied by the pores in the extra-axonal region.

Finally, for the comparison study, all the signals are computed using the intrinsic extracellular diffusivity value D_{int} of water molecules at 37° which is equal to $3 \times 10^{-9} \frac{m^2}{s}$.

3.2.1 Environment with pores only vs free diffusion

As expected, adding spherical entities to the free diffusion environment increases the attenuation signals, as the spins are subjected to more restrictions, as shown on FIGURES 3.10A, 3.10C, 3.11A and 3.11C. On those figures, we can also notice that the signals increase proportionally with the intra-pore volume fraction, as the pores occupy a large space in the voxel and therefore increasing the restriction.

Nevertheless, if we assume that the pores are rigid entities without inner water molecules, for lower b-values, the MC attenuation signals tend to decrease with the intra-pore volume fraction and get even below the free diffusion attenuation signal, as depicted on FIGURES 3.10B and 3.11B. This is mainly due to the fact that the initial difference between the MC signals with and without pores is low, such that when the MC signals with pores are weighted by a smaller volume fraction, the overall signals get lower.

Additionally, despite for b-values higher than $1000 \frac{s}{mm^2}$, the signals obtained with the two sets of spherical parameters (TABLE 2.3) yield identical values. Prompting us for the rest of this thesis, to discuss the results based on one set, in order to not overcrowd the section with numerous figures. Nevertheless, the corresponding results of the second set are provided in Appendix C and explicit references are made when the results divert or help emphasizing the observations. Subsequently, for those high b-values, we verify that the MC signals were really small (FIGURES 3.10A and 3.11A), such that adding the intra-pore signal yields identical signals (FIGURES 3.10C and 3.10C).

Moreover, based on the values of TABLE 3.6, FIGURES 3.10A and 3.11A show that smaller b-values obtained with a shorter pulse duration δ exhibit a steeper increase in their MC signals with respect to the relative intra-pore volume fraction $f_{in_{(s,rel)}}$ (i.e. $\left|\frac{\Delta y}{\Delta x}\right|_{(\delta=5)} > \left|\frac{\Delta y}{\Delta x}\right|_{(\delta=13)} > \left|\frac{\Delta y}{\Delta x}\right|_{(\delta=17.5)}$). This behaviour also occurs when the separation time Δ increases in the ActiveAx-like scheme (i.e. $\left|\frac{\Delta y}{\Delta x}\right|_{(\Delta=87)} > \left|\frac{\Delta y}{\Delta x}\right|_{(\Delta=20)}$), and when the gradient intensity G decreases (i.e. $\left|\frac{\Delta y}{\Delta x}\right|_{(G=31.9)} > \left|\frac{\Delta y}{\Delta x}\right|_{(G=37.8)}$) while the pulse duration δ and separation time δ are fixed. Those observations are not investigated for higher b-values as their signal intensity is too small (i.e. of order of magnitude of 10^{-3}) to be representative.

The same conclusions, for the pulse duration δ and the separation time Δ, about the steepness of the ***decrease*** of the signal attenuation in function of the relative intra-pore volume fraction $f_{in_{(s,rel)}}$ are derived form attenuation signals (FIGURES 3.10B and 3.11B) obtained for environments where the pores are considered to be empty. Furthermore, the increase in steepness is observed for decreasing values of the gradient intensity G, independently of the value of δ and Δ (i.e. $\left|\frac{\Delta y}{\Delta x}\right|_{(G=31.9)} > \left|\frac{\Delta y}{\Delta x}\right|_{(G=37.8)} > \left|\frac{\Delta y}{\Delta x}\right|_{(G=57)} > \left|\frac{\Delta y}{\Delta x}\right|_{(G=60)}$). Similarly, higher b-values are not considered.

On the other hand, when the attenuation signals (FIGURES 3.10C and 3.11C) are driven from environments with water-filled pores, the signal increase is steeper for smaller b-values obtained with longer pulse duration δ (i.e. $\left|\frac{\Delta y}{\Delta x}\right|_{(\delta=17.5)} > \left|\frac{\Delta y}{\Delta x}\right|_{(\delta=13)} > \left|\frac{\Delta y}{\Delta x}\right|_{(\delta=5)}$). Subsequently, the same inversion of

behaviour with respect to the previous attenuation signals is observed for the separation time Δ : where the increase in steepness occurs for decreasing values of Δ (i.e. $\left|\frac{\Delta y}{\Delta x}\right|_{(\Delta=20)} > \left|\frac{\Delta y}{\Delta x}\right|_{(\Delta=87)}$). This inversion of comportment also occurs for the gradient intensity at fixed pulse duration δ and separation time Δ : $\left|\frac{\Delta y}{\Delta x}\right|_{(G=37.8)} > \left|\frac{\Delta y}{\Delta x}\right|_{(G=31.9)}$. Despite the fact that attenuation signals of higher b-values have now more significant values, as their attenuation signals are highly equal and their difference in steepness is negligible.

Although all those observations are interesting, a more careful investigation should be done in order to study individually the impact of PGSE parameters on the steepness of the DWI signal variation in function of the relative intra-pore volume fraction. This could be done by designing a custom multi-shell scheme with different acquisition sequences for which only one parameter varies at a time.

	b-values $[\frac{s}{mm^2}]$	$G\,[\frac{T}{m}]$	$\delta\,[ms]$	$\Delta\,[ms]$
ActiveAx	496.05	57	5	87
	682.16	60	13	20
	2453.30	46	15	77
	2634.82	58	12	80
NODDI	712.98	31.9	17.5	37.8
	1001.10	37.8		
	1997.91	53.4		
	2851.90	63.8		

TABLE 3.6: **PGSE parameters of the two clinically-realistic protocols that are used (i.e. ActiveAx-like and NODDI-like schemes).**

3.2.2 Hexagonally packed fasciles of identical axons environment with vs without pores

Strangely, adding spherical pores to an hexagonally packed environment of fasciles, only increase the MC attenuation signals for gradient directions that have a higher parallel component to the fasciles central direction $\hat{n}$, as shown on FIGURES 3.12A and 3.13A. This odd behaviour could be understood by assuming that a certain "diffraction" phenomenon occurs when we add symmetrically small spherical particles. Nevertheless, we lack theoretical bases to assert that with certainty. Furthermore, as this behaviour tends to disappear when the pores are added in a wider extracellular region, as depicted onFIGURES C.8A and C.9A, where the signals are computed with the second settings of microstructure parameters. However excepted for this main difference, the rest of our observations are valid for both settings.

Furthermore, based on FIGURES 3.12B and 3.13B, we reinforce the fact that increasing the intra-pore volume fraction, or in other words decreasing the extra-cell region, yield greater difference between the signal with pores than without pores.

As already mentioned in § 3.2.1 and as it can be spotted on FIGURES 3.12D, 3.12C, 3.13D and 3.13C, considering empty rigid pores decrease the attenuation signals, whereas considering pores filled with water molecules increases the attenuation signals. The latter assertion is due to the fact that the MCF intra-pore signals added to the MC signals are very high (i.e. they are always equal 1, the highest attenuation signal possible). This high intensity arises as the signals are computed in an extremely small restricted environment, i.e. a spherical environment with a radius of order of tenth of nanometer.

3.2.3 Crossing fasciles of identical axons environment with vs without pores

On the graphics of FIGURE 3.14 to 3.20, the signals are expected to be in the upper region with respect to *identity line* "$CYL: f_{in_{(s,rel)}} = 0$" which correspond to the signals without pores in function of themselves.

Subsequently, the same conclusions drawn in § 3.2.3 for the hexagonally packed fascicles environment, can be readily inferred for the crossing fasciles environment :

(i) some of the MC attenuation signals seem to be subject to the so presumed "diffraction" phenomenon, as portrayed on FIGURES 3.14 and 3.15 ;

(ii) small difference between the compared MC signals is observed, as suggested on FIGURES 3.14 and 3.16B ;

(iii) considering pores with inner water molecules yield high attenuation signals, whereas considering empty rigid pores decrease those signals.

Nevertheless, the difference between the MC signals for the two compared environments varies less in function of the relative intra-pore volume fractions $f_{in_{(s,rel)}}$: the boxplot (FIGURES 3.16A and 3.16B) for values of $f_{in_{(s,rel)}}$ equal to 0.10, 0.07 and to 0.05 are relatively more similar. Moreover, there seem to be an odd increase going from 0.10 to 0.07, where we would have expected a decrease.

Finally, as there is no more a single principal central direction, we are no more able to tell if the "diffraction" occurs for specific directions.

3.2.4 Results

Environment with pores only vs free diffusion

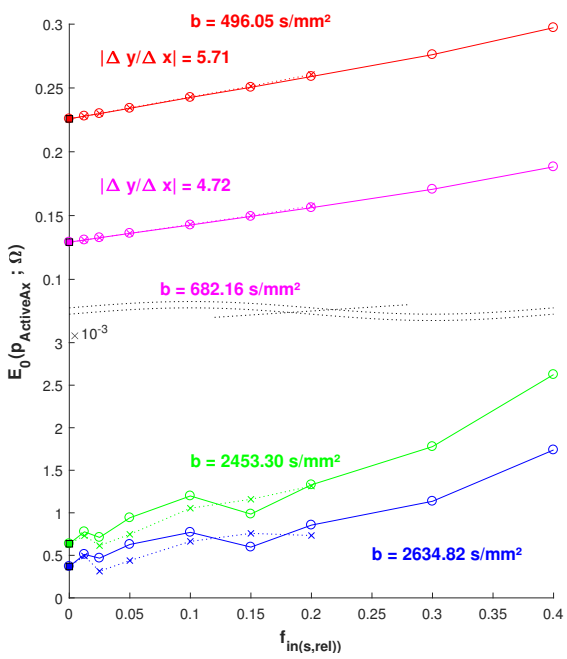

(A) **MC signals for comparison following 3.7a.**

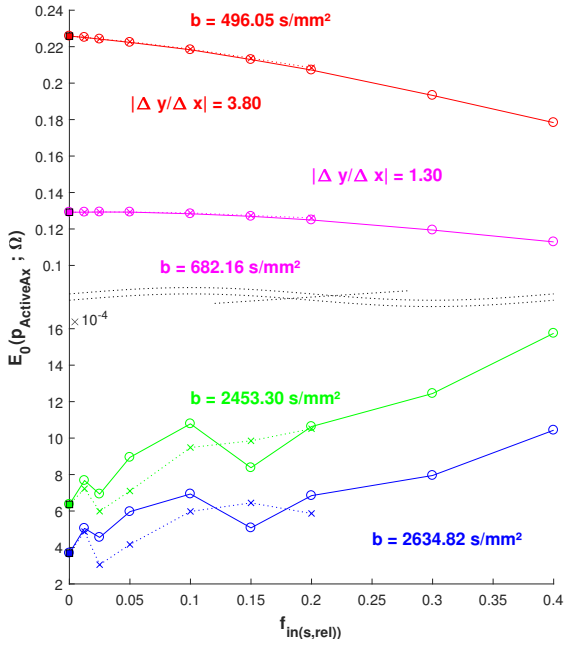

(B) **Total signals with pores considered without water molecules for comparison following 3.7b.**

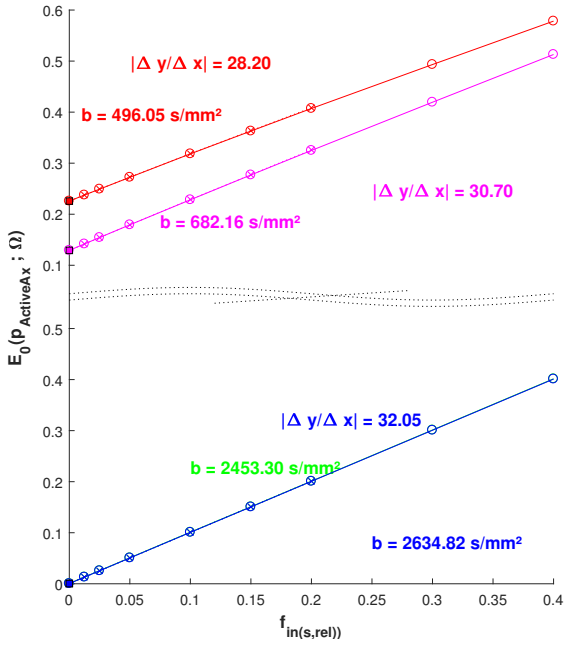

(C) **Total signals with pores considered filled with water molecules for comparison following 3.7c.**

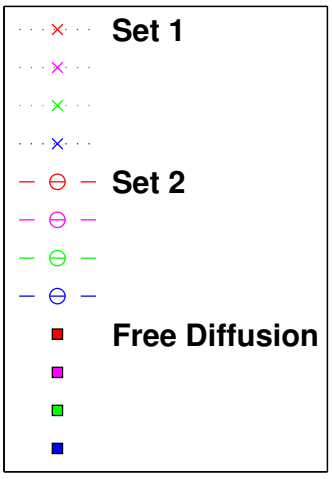

(D) **Legend for the three signal plots.**

FIGURE 3.10: **Attenuation signals obtained using the ActiveAx-like scheme for the environments with pores only and in the case of free diffusion.** The two dashed line crossed by another dash line are there to delimit the two different scales used respectively for lower and higher b-values.

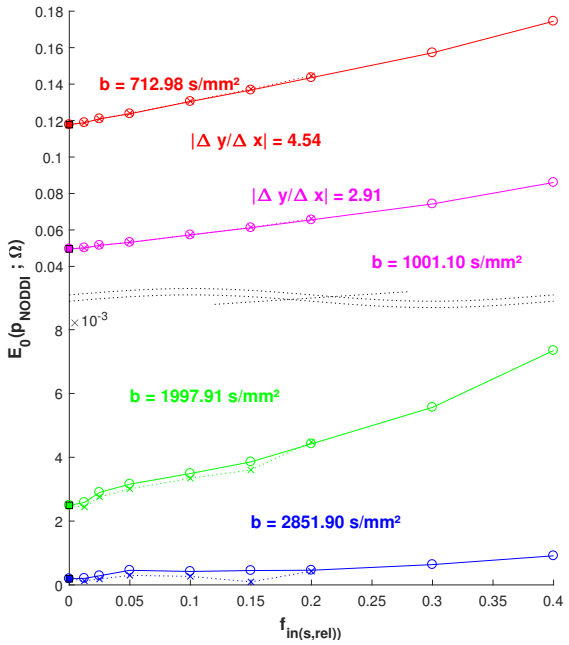

(A) **MC signals for comparison following 3.7a.**

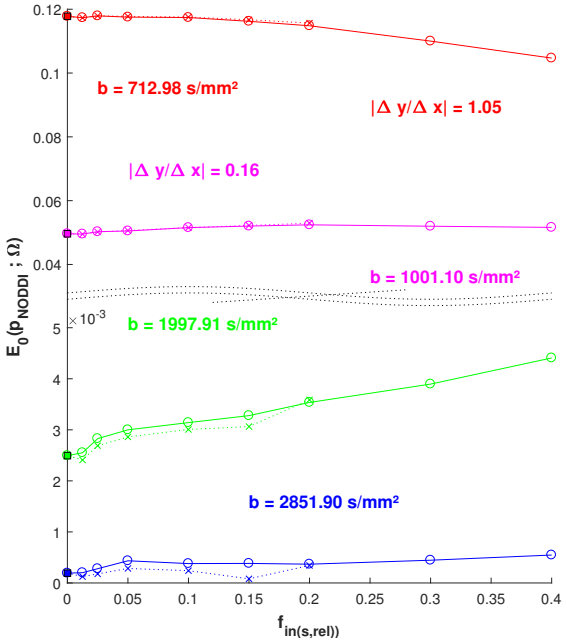

(B) **Total signals with pores considered without water molecules for comparison following 3.7b.**

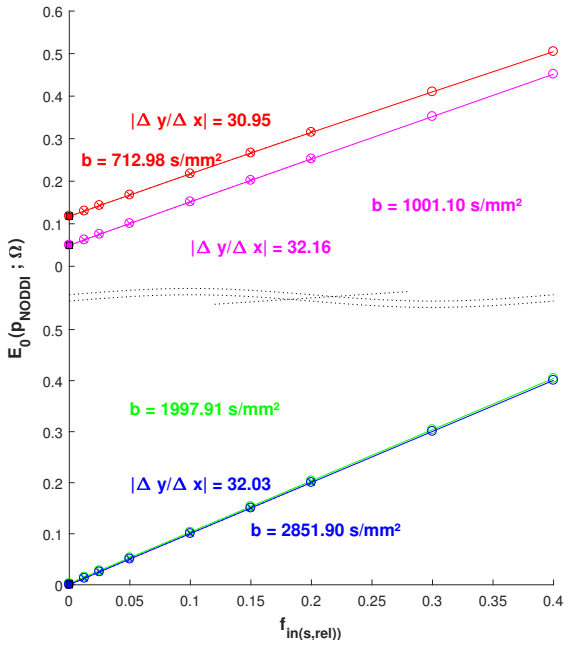

(C) **Total signals with pores considered filled with water molecules for comparison following 3.7c.**

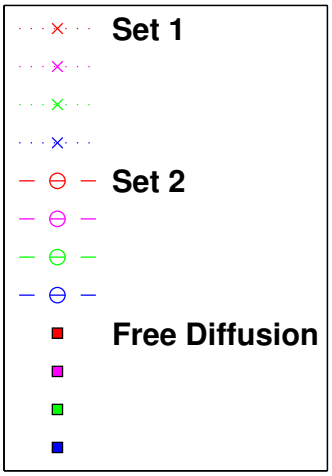

(D) **Legend for the three signal plots.**

FIGURE 3.11: **Attenuation signals obtained using the NODDI-like scheme for the environments with pores only and in the case of free diffusion.** The two dashed line crossed by another dash line are there to delimit the two different scales used respectively for lower and higher b-values.

Hexagonally packed fasciles of identical axons environment with vs without pores

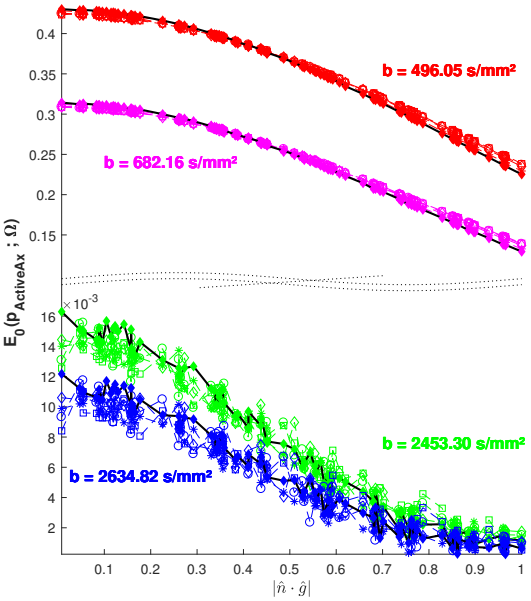

(A) **MC signals for comparison following 3.7a.**

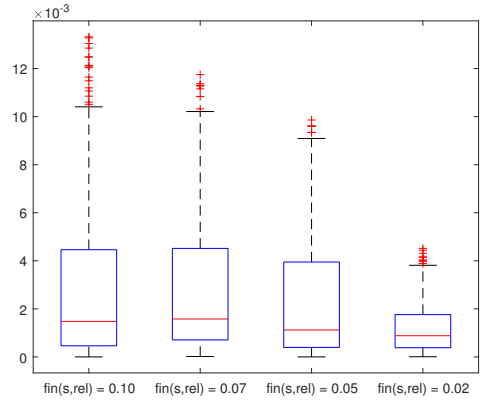

(B) **Differences between the MC signals computed with and without pores.**

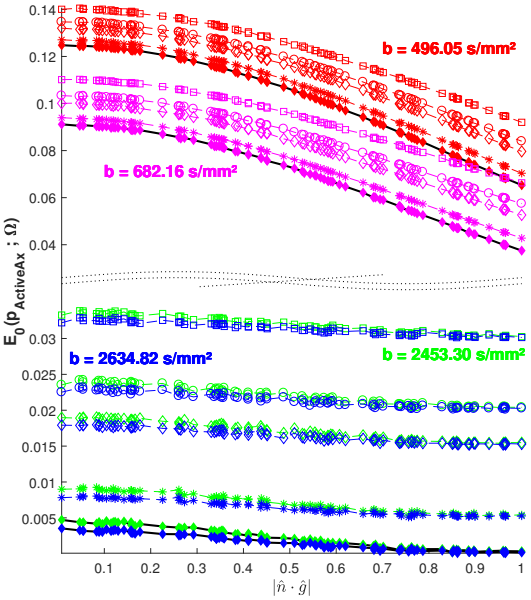

(C) **Total signals with pores considered filled with water molecules for comparison following 3.7c.**

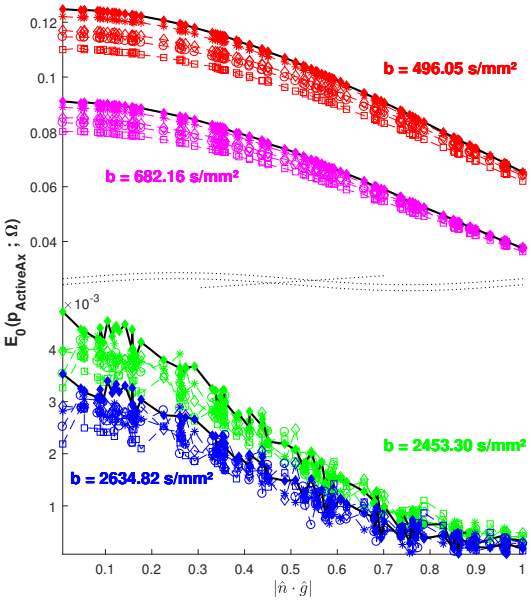

(D) **Total signals with pores considered without water molecules for comparison following 3.7b.**

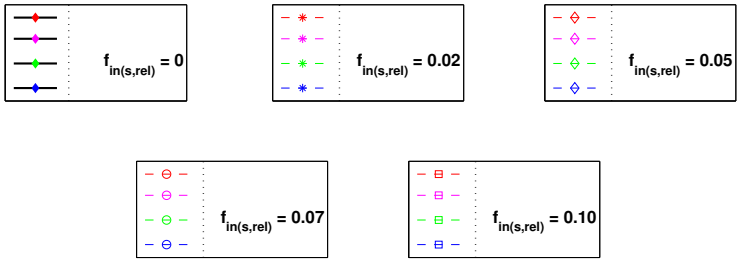

(E) **Legend for the three signal plots.**

FIGURE 3.12: **Attenuation signals obtained using the ActiveAx-like scheme for the hexagonally packed fasciles of identical axons environment with vs without pores.** The two dashed line crossed by another dash line are there to delimit the two different scales used respectively for lower and higher b-values.

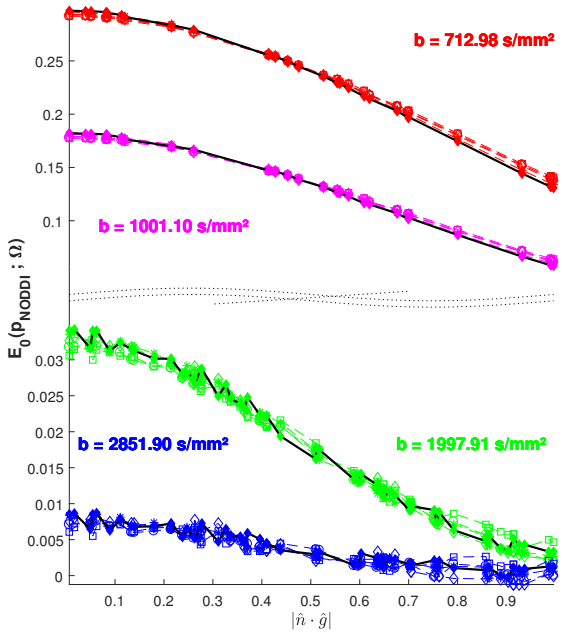

(A) **MC signals for comparison following 3.7a.**

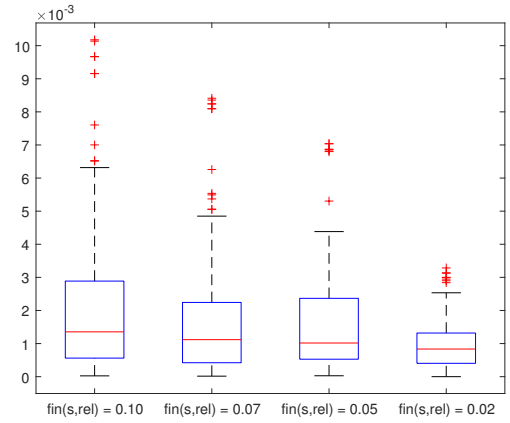

(B) **Differences between the MC signals computed with and without pores.**

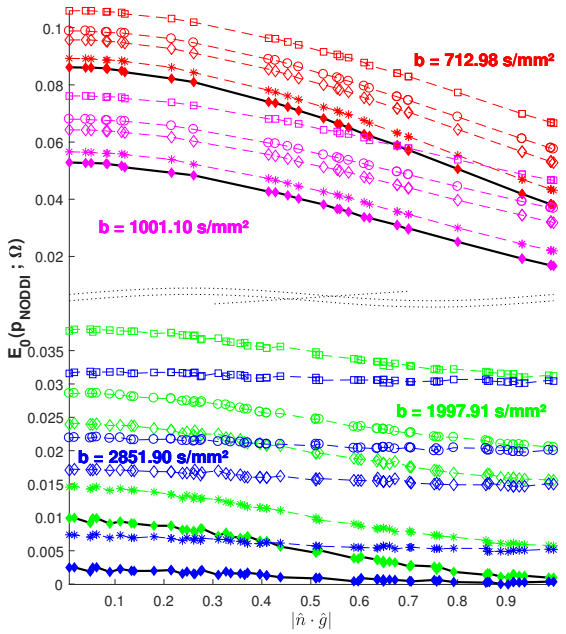

(C) **Total signals with pores considered filled with water molecules for comparison following 3.7c.**

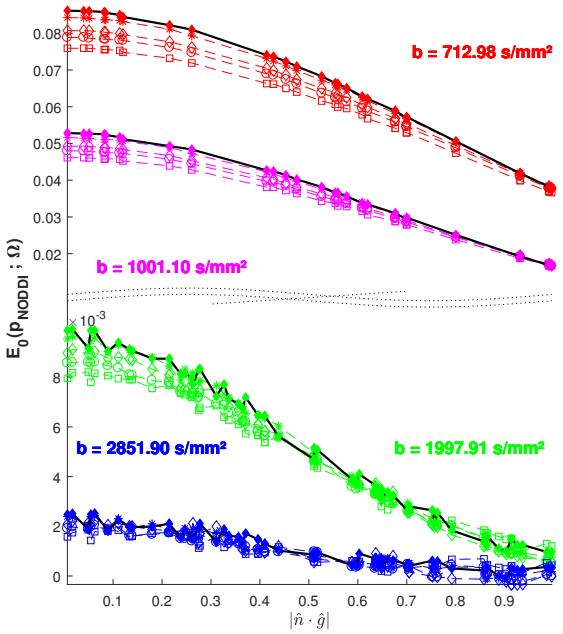

(D) **Total signals with pores considered without water molecules for comparison following 3.7b.**

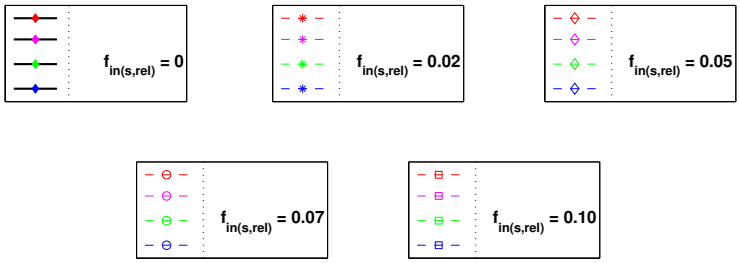

(E) **Legend for the three signal plots.**

FIGURE 3.13: **Attenuation signals obtained using the NODDI-like scheme for the hexagonally packed fasciles of identical axons environment with vs without pores.** The two dashed line crossed by another dash line are there to delimit the two different scales used respectively for lower and higher b-values.

Crossing fasciles of identical axons environment with vs without pores

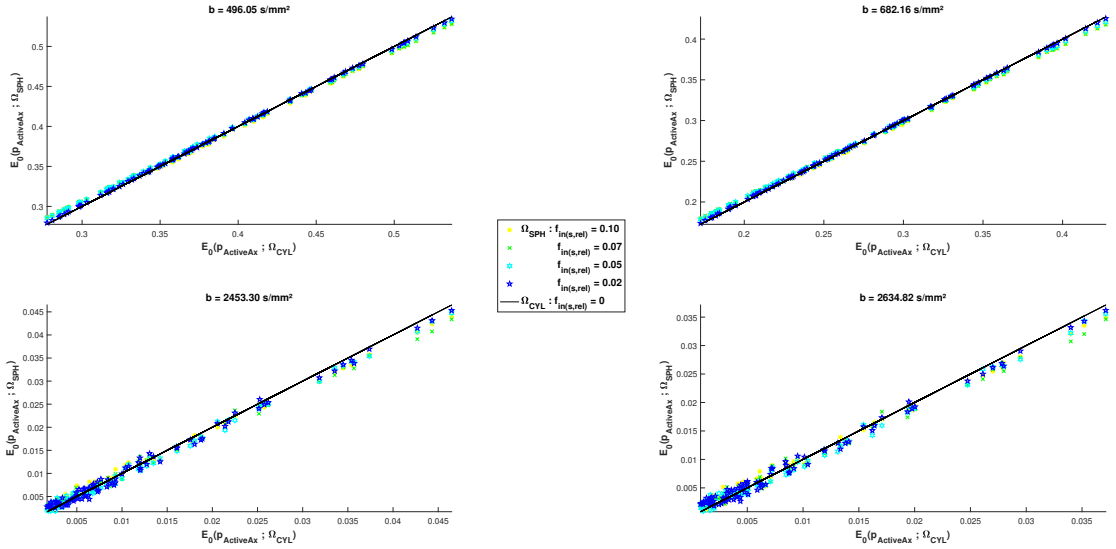

FIGURE 3.14: **MC attenuation signals obtained using the ActiveAx-like scheme for the crossing fasciles of identical axons environment with vs without pores.**

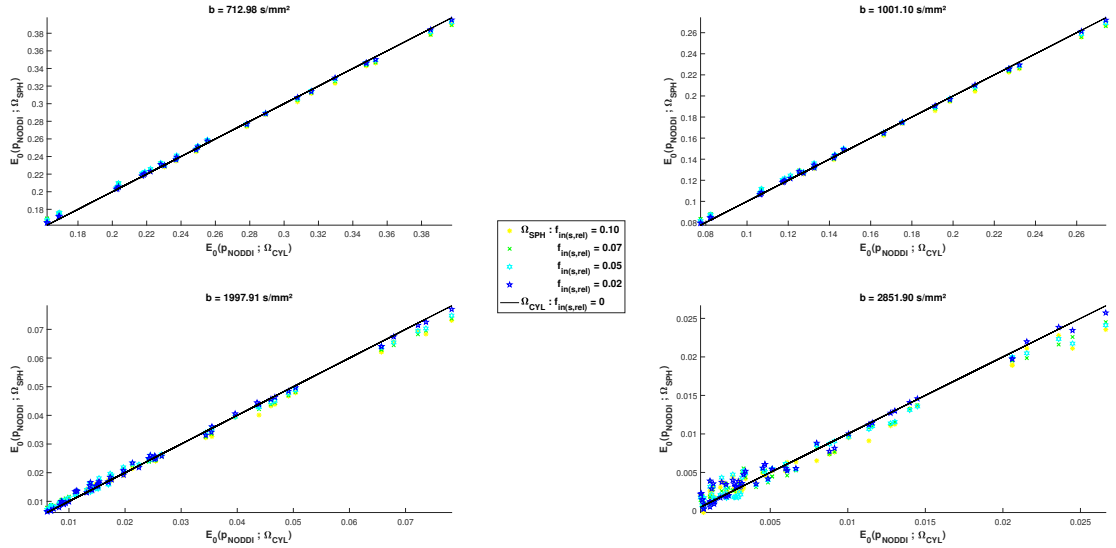

FIGURE 3.15: **MC attenuation signals obtained using the NODDI-like scheme for the crossing fasciles of identical axons environment with vs without pores.**

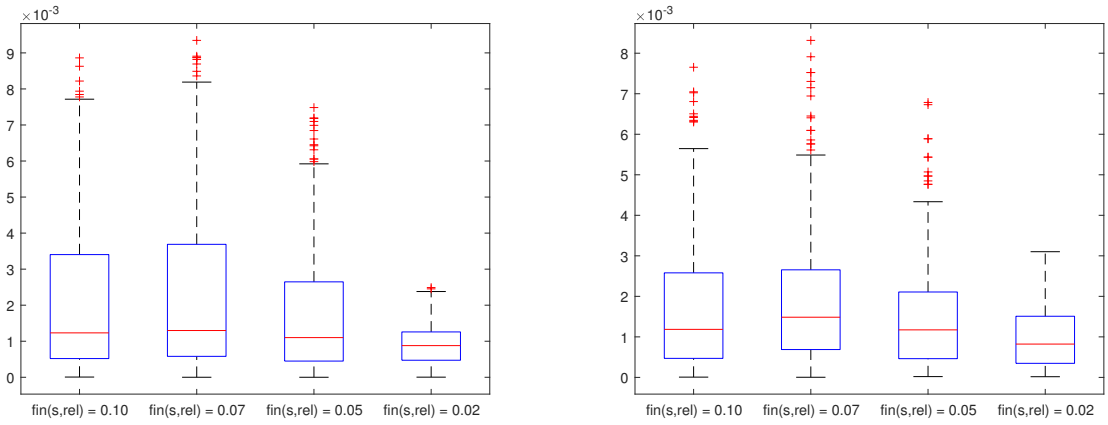

(A) **Using ActiveAx-like scheme.** (B) **Using NODDI-like scheme.**

FIGURE 3.16: **Differences between the MC signals computed with and without pores.**

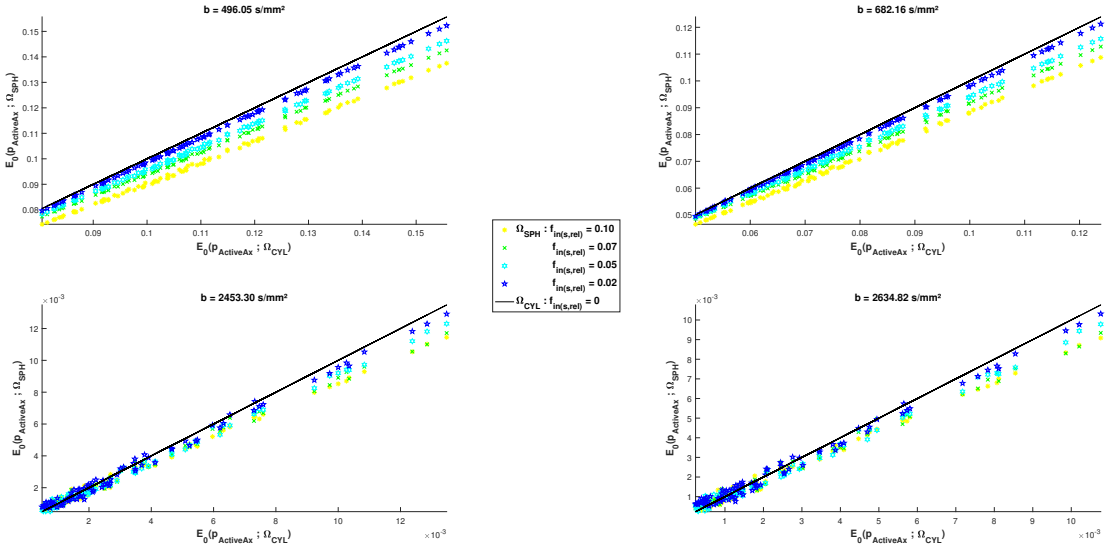

FIGURE 3.17: **Attenuation signals obtained using the ActiveAx-like scheme for the crossing fasciles of identical axons environment with vs without pores considered without water molecules.**

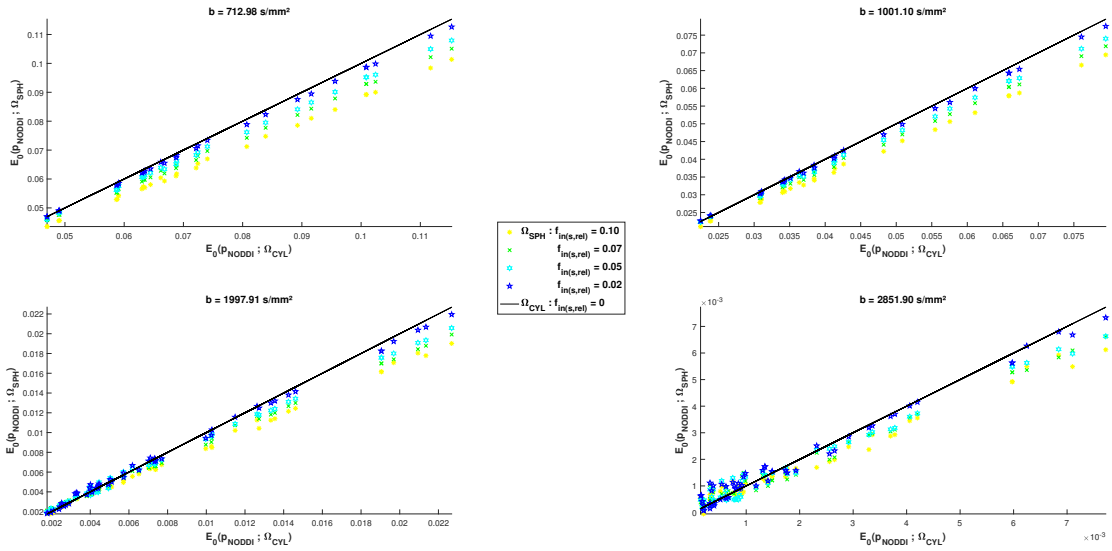

FIGURE 3.18: **Attenuation signals obtained using the NODDI-like scheme for the crossing fasciles of identical axons environment with vs without pores considered without water molecules.**

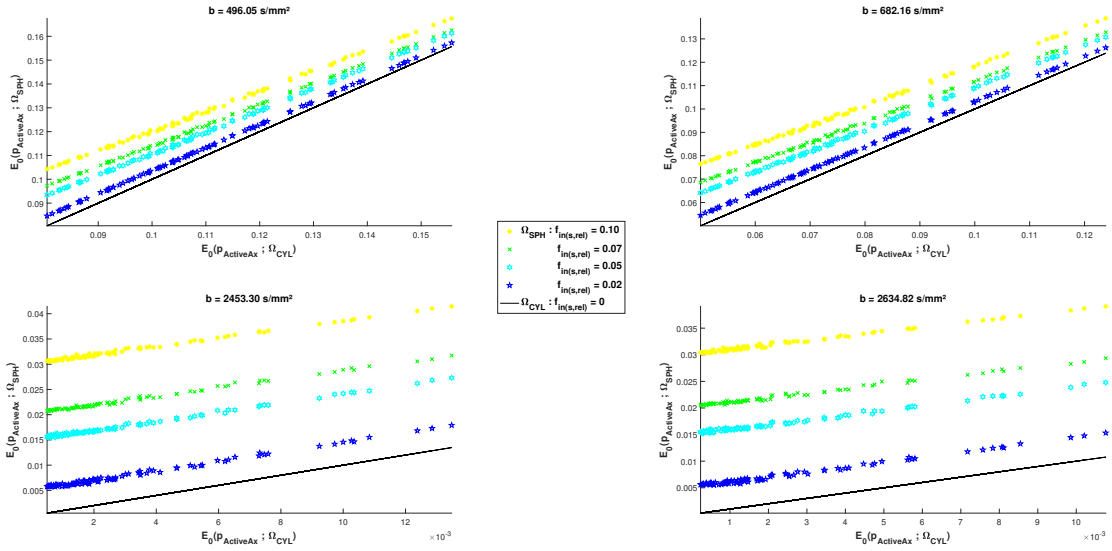

FIGURE 3.19: **Attenuation signals obtained using the ActiveAx-like scheme for the crossing fasciles of identical axons environment with vs without pores considered filled with water molecules.**

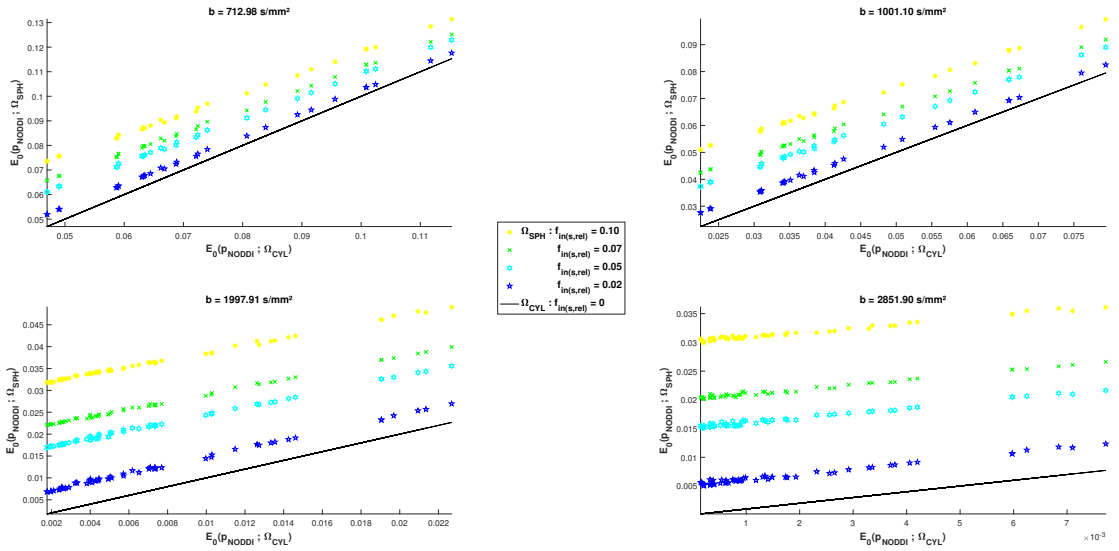

FIGURE 3.20: **Attenuation signals obtained using the NODDI-like scheme for the crossing fasciles of identical axons environment with vs without pores considered filled with water molecules.**

3.3 Determination of the effective extracellular diffusivity

As we have seen in § 3.2, except for "diffraction"-dependent settings, the MC signals in a more restricted environment yield higher values. Moreover, this is always the case for the attenuation signals in which the pores contains water molecules. Nevertheless, if we decrease the diffusivity value D used in the previous study, for the extra-cell compartment of the environments without pores, their attenuation signals increase. This is understandable as the diffusivity is the ratio of the thermal energy to the friction : therefore, decreasing its value is similar to increasing the friction and so adding more restriction to the motion of the spins.

Based on that, we try to determine the effective extracellular diffusivity

$$D_{eff} = argmin_{D_i} \left|\left| E(\boldsymbol{p}_{pgse};\Omega)_{SPH,D_{int}} - E(\boldsymbol{p}_{pgse};\Omega)_{CYL,D_i} \right|\right| \tag{3.9}$$

of the environments without pores that yields the "same" attenuation signals as the environments with pores for which the intrinsic diffusivity value D_{int} equal to $3 \times 10^{-9} \frac{m^2}{s}$, is used. Moreover the candidate values D_i for D_{eff} are chosen in the interval $]0, D_{int}[$. For the hexagonally packed and crossing fasciles of identical axons environments, the candidate values are found in TABLE 3.7 ; whereas for the free diffusion environment, as an exact analytical solution (1.35a) exists (i.e. requiring no simulations), 1000 candidate values are linearly sampled from the interval $]0, 3 \times 10^{-9}[$.

D_i	1	1.125	1.25	1.375	1.5	1.625	1.75	1.875	1.938	2
$[\times 10^{-9} \frac{m^2}{s}]$	2.125	2.25	2.375	2.5	2.5625	2.625	2.6875	2.75	2.875	3

TABLE 3.7: **Candidate values for effective extracellular diffusivity used to determine the effective extracellular diffusivity D_{eff} in the case of hexagonally packed and crossing fasciles of identical axons environments.**

Furthermore, the determination of the equivalent diffusivity is done with respect to the signals where the pores contains water molecules. This choice is driven by the fact that there are little to no difference between the MC signals with pores and without pores, and similarly with the pairs of signal with rigid pores, as shown on FIGURES 3.21 and 3.22. Such that the effective extracellular diffusivity is always

equal to the intrinsic diffusivity.

As expected and as portrayed on FIGURES 3.24, 3.24 and 3.25, the effective extracellular diffusivity decreases with the relative intra-pore volume fraction. Meaning that in order for the environments without pores to behave like the homologous environment with pores, restriction must be artificially added by decreasing the diffusivity.

Furthermore as suggested by FIGURES 3.23A and 3.23B, the effective extracellular diffusivity is not sensitive to the radius of the pores. This last assertion must be taken cautiously, as we did not explore enough range of different radii.

Investigating TABLE 3.8, we notice that the relative intra-pore volume fraction that give an effective diffusivity equal to the commonly used diffusivity value (i.e. $2 \times 10^{-9} \frac{m^2}{s}$) in MC simulations decreases with increasing b-values. Prompting us to conclude that for b-values that are expected to allow better description of the signal decay and refine the proposed model [20], that the lower commonly used diffusivity mimics restrictions due to pores with smaller intra-pore volume fraction.

Furthermore, we can spot that as the environment gets more complex, a higher intra-pore volume fraction is requested to reach this commonly used diffusivity value for smaller b-values. Additionally, for b-values higher than $1000 \frac{s}{mm^2}$, the necessary intra-pore volume fraction to reach a diffusivity of $2 \times 10^{-9} \frac{m^2}{s}$ is strictly smaller than 10%.

		Ω_{s-only}		Ω_{hex}		Ω_{cross}	
		ActiveAx	NODDI	ActiveAx	NODDI	ActiveAx	NODDI
$fin_{(s,rel)}$	ALL	0.131	0.085	> 0.10	0.103	> 0.10	> 0.10
	b_1	0.189	0.124	> 0.10	> 0.10	> 0.10	> 0.10
	b_2	0.129	0.086	> 0.10	> 0.10	> 0.10	> 0.10
	b_3	0.010	0.016	0.038	0.052	0.048	0.063
	b_4	0.009	0.008	0.031	0.026	0.043	0.038

TABLE 3.8: **Relative intra-pore volume fraction corresponding to an effective diffusivity equal to the commonly used diffusivity (i.e. $2 \times 10^{-9} \frac{m^2}{s}$) in the MC simulations found in the literature, for the first set of environment configuration.** Ω_{s-only}, Ω_{hex} and Ω_{cross} refer respectively to the three studies environments : spheres only environment, hexagonally packed fascicles of identical axons surrounded by hexagonally distributed distributed pores and crossing fascicles of identical axons surrounded by rectangularly packed pores. Moreover, "ALL", b_1, b_2, b_3 and b_4 respectively refer to the entire protocol (i.e. either ActiveAx-like scheme or NODDI-like scheme) and to their b-values from the lowest (b_1) to the highest (b_4). For some of the configuration, the corresponding relative intra-pore volume fraction is higher than the maximal value (i.e. $fin_{(s,rel)} = 0.10$) that was investigated for the set.

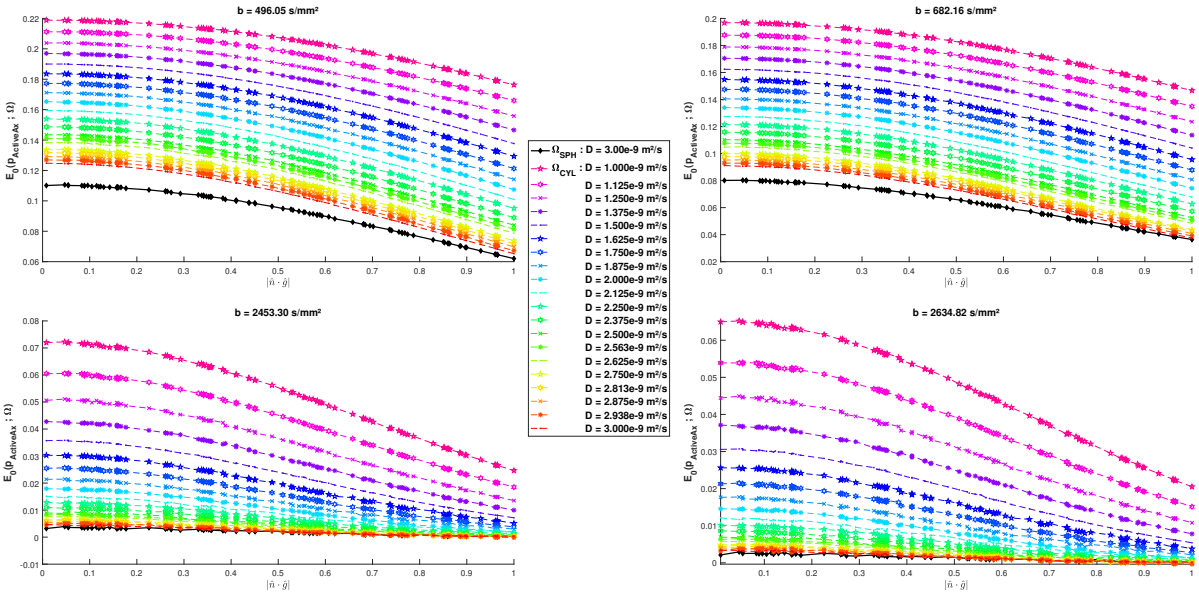

FIGURE 3.21: **Attenuation signals obtained using the ActiveAx-like scheme for the hexagonally packed fasciles of identical axons environment, considering various diffusivity values when no pores are present and the intrinsic diffusivity value D_{int} when empty rigid pores are present, with a relative intra-pore volume fraction $f_{in_{(s,rel)}}$ of 0.10.**

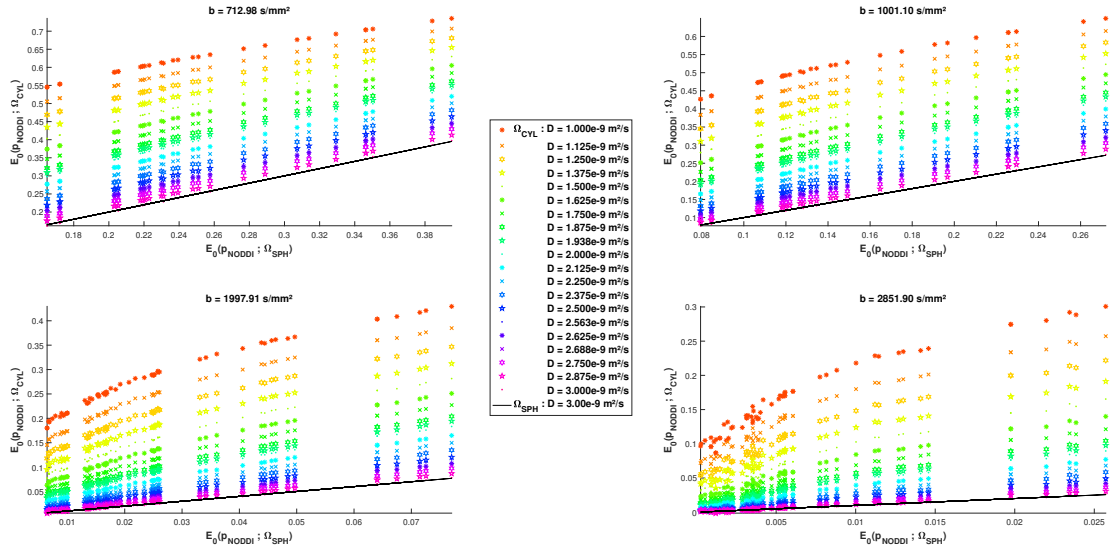

FIGURE 3.22: **MC signals obtained using the NODDI-like scheme for the crossing fasciles of identical axons environment, considering various diffusivity values when no pores are present and the intrinsic diffusivity value D_{int} when pores are present, with a relative intra-pore volume fraction $f_{in_{(s,rel)}}$ of 0.02.**

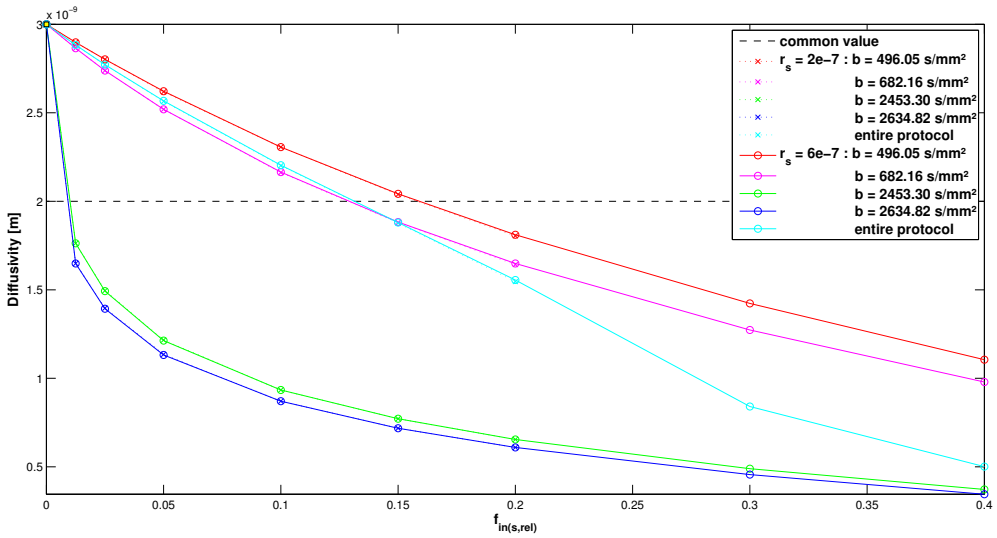

(A) **Using ActiveAx-like scheme.**

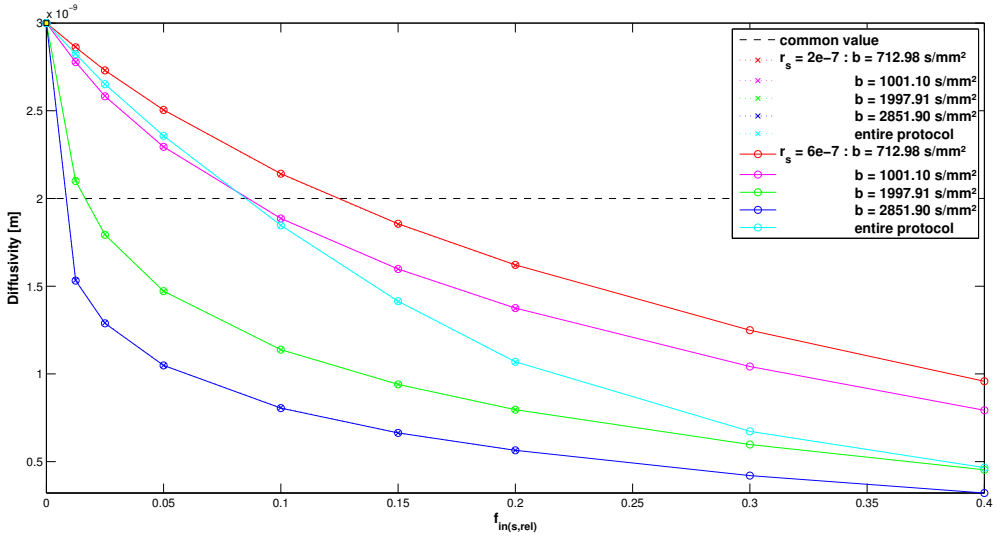

(B) **Using NODDI-like scheme.**

FIGURE 3.23: **Variation of the effective extracellular diffusivity D_{eff} in function of the relative intra-pore volume fraction $f_{in_{(s,rel)}}$ for free diffusion environment with respect to the pores only environment.**

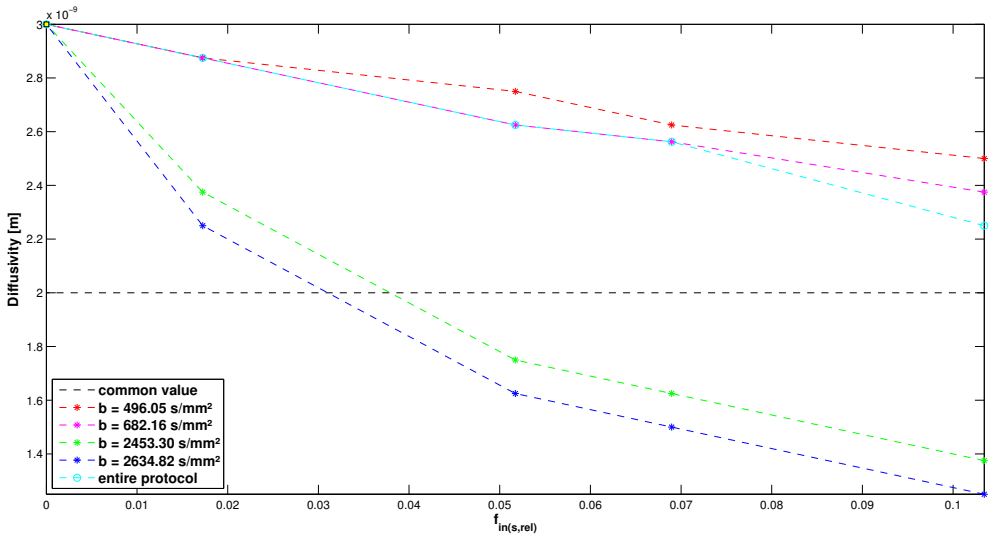

(A) **Using ActiveAx-like scheme.**

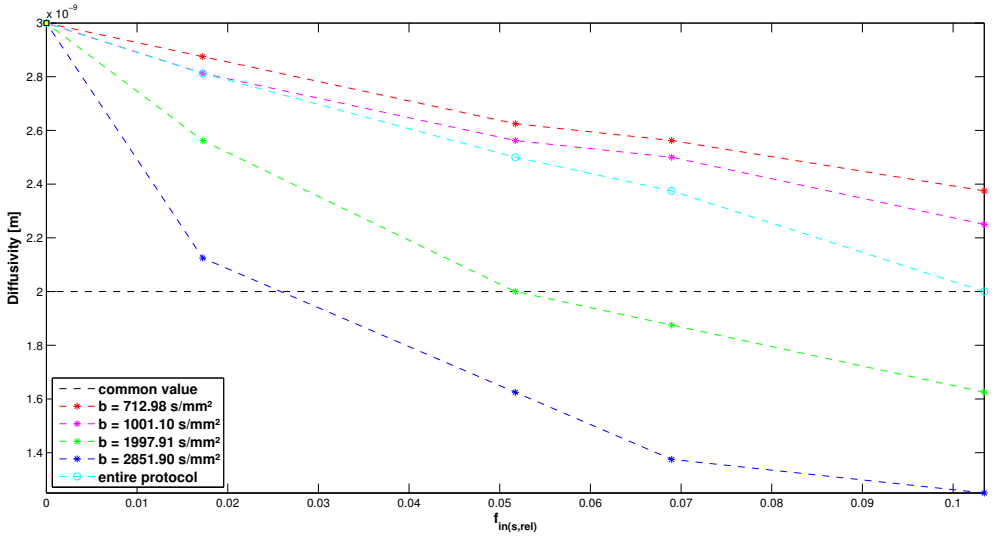

(B) **Using NODDI-like scheme.**

FIGURE 3.24: **Variation of the effective extracellular diffusivity D_{eff} in function of the relative intra-pore volume fraction $f_{in_{(s,rel)}}$ for hexagonally packed fasciles of identical axons environment without pores with respect to the similar environment with pores, using the microstructure parameters of the firs set.**

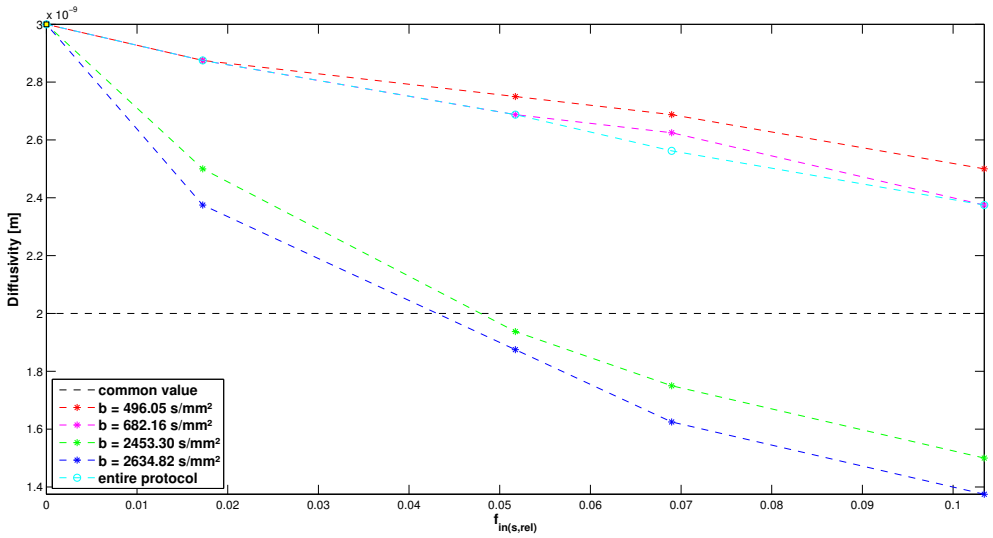

(A) **Using ActiveAx-like scheme.**

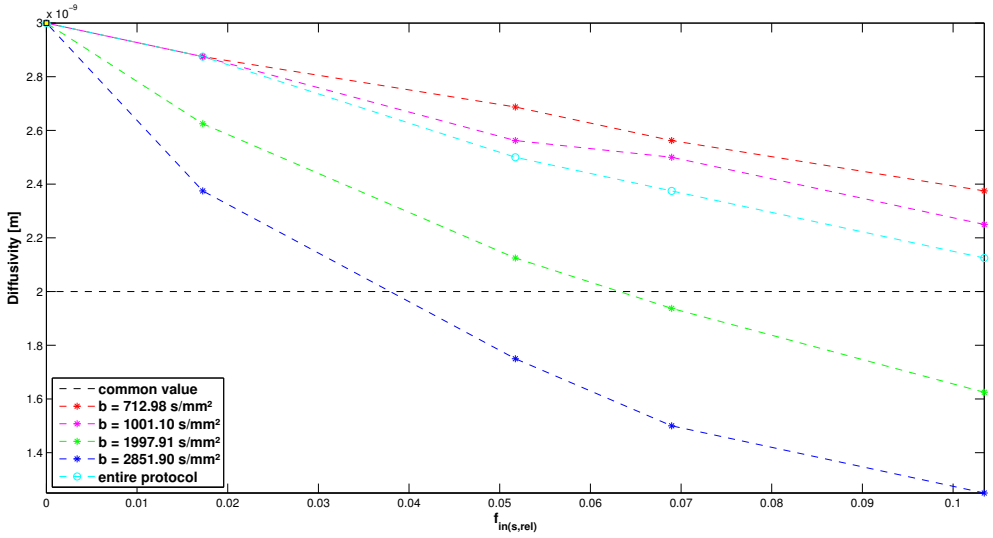

(B) **Using NODDI-like scheme.**

FIGURE 3.25: **Variation of the effective extracellular diffusivity D_{eff} in function of the relative intra-pore volume fraction $f_{in_{(s,rel)}}$ for crossing fasciles of identical axons environment without pores with respect to the similar environment with pores, using the microstructure parameters of the firs set.**

Conclusions and perspectives

This thesis has investigated the impact of spherical pores on the free diffusion environment and on two microstructure environments composed of fascicles of axons modelled by infinitely long cylinders that artificially represent the brain white matter.

This study was carried out using mainly the Monte-Carlo simulation framework, described in Chapter 2, which is more suited for arbitrary and more complex geometrical environments, e.g. the extracellular compartment, our region of interest. In addition, , a comparative study of the synthetically generated DWI attenuation signals was carried out after careful investigation of the optimal MC simulation parameters to be used. This was illustrated in Chapter 3 along with the determination of the effective diffusivity that corresponds to each of the studied sets of microstructure configuration.

By comparing the signals, we verified that the MC signals in pore-added environments and the total signals for environments counting pores filled with water molecules (i.e. modelling glial cells), exhibit always higher values (i.e. subject to more restriction) than their homologous environments without pores. Nevertheless exceptions occur for the acquisition sequences for which the gradient direction is more perpendicular than parallel to the principal direction of the fascicles. This phenomenon was conjectured to be caused by "diffraction-like" behaviours occurring when we add symmetrically and periodically pores in regions already subject to important restriction. On the other hand, environments with empty pores (e.g. representing empty cellular debris), display a decrease in their DWI signals with respect to their homologous environments without pores. This diminution in signal intensity can be mathematically understood, as, in order to obtain those signals, the MC signals are weighted by their corresponding extracellular volume fractions, which are smaller for environments including pores.

Subsequently, the effective extracellular diffusivity of each of our settings was determined, by fixing the diffusivity of the pore-added environments to the intrinsic diffusivity of water molecules in human at normal body temperature and by varying the diffusivity of the pore-free environments. This effective diffusivity was found to be always equal to the intrinsic one, for MC signals and for signals compared to empty pore-added environments, independently of the microstructural configuration. In contrast, this effective diffusivity was sensitive to and decreased with the (relative) intra-pore fraction volume, in the case of water-filled pore environments. Furthermore, the results from this study permit to observe that this effective diffusivity was not sensitive to the radius of the pores. Nonetheless, as we did not explore a wide range of various radii, the above assertion is not absolute. Subsequently, we provided, for each clinically-realistic studied protocol and their b-values, the (relative) intra-pore volume fraction which yields the same effective diffusivity used for MC simulations founded in the literature.

Finally, due to prohibitive computation times, we did not investigate the impact of spherical pores on single fascicles of gamma-distributed axons, another well-known and used microstructure environment in synthetic study of DWI signals done with MC simulations. Moreover, additional sets of pore-added microstructure environments could be studied, in particular considering a wider range of pore radii. Both approaches leaving room for future improvements on further diffusivity studies.

Appendix A

Determination of the intra-axonal and intra-glial volume fractions

A.1 For hexagonally packed fasciles of identical axons surrounded by hexagonally distributed glial cells

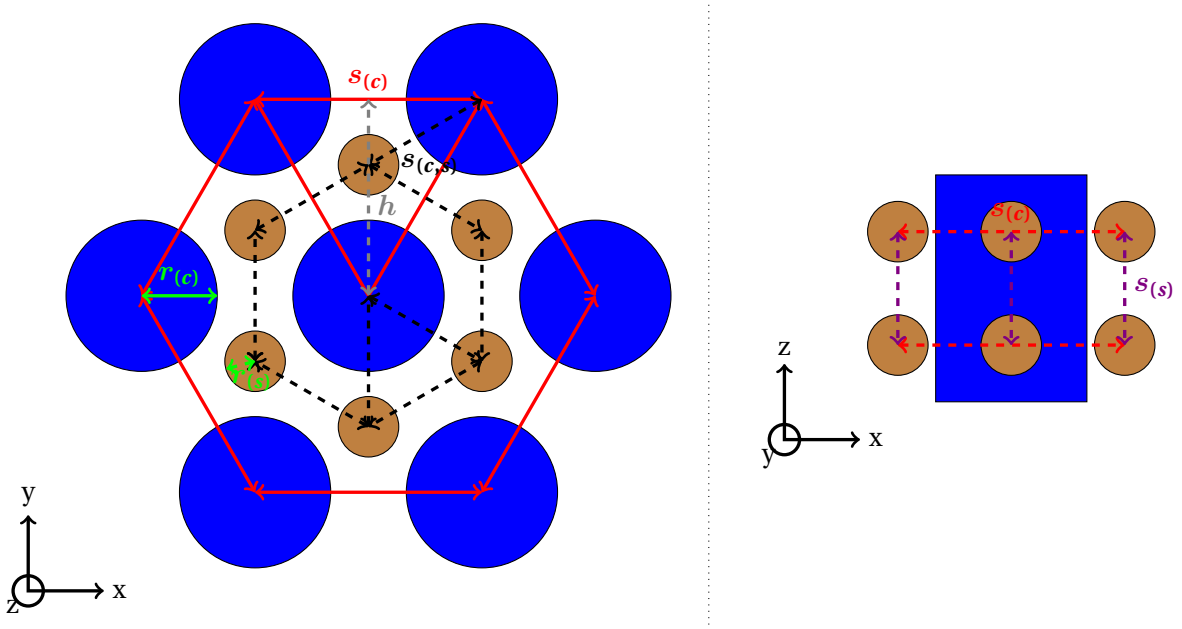

A.1.1 Intra-axonal volume fraction

As the fasciles are modelled by infinitely long (in the z-axis) and parallel cylinders of the same radius, the intra-axonal volume fractions is determined by the ratio of the area occupied by the cylinders and the area of the enclosing voxel, in the xy-axis. Moreover, as the cylinders are hexagonally packed, this ratio can be determined by considering only the area of one hexagon with respect to the area occupied

by the within spherical portions :

$$f_{in_{(c)}} = \frac{A_{cyl}}{A_{hex}} = \frac{A_{\bigcirc} + 6A_{\bigcirc\!\!\!\frac{}{3}}}{6A_{\triangle}} \text{ with } \begin{cases} A_{\bigcirc} = \pi r_{(c)}^2 \\ A_{\bigcirc\!\!\!\frac{}{3}} = \dfrac{\pi r_{(c)}^2}{3} \\ A_{\triangle} = \dfrac{s_{(c)}h}{2} = \dfrac{s_{(c)}}{2}\sqrt{s_{(c)}^2 - \dfrac{s_{(c)}^2}{4}} = \dfrac{\sqrt{3}s_{(c)}^2}{4} \end{cases} \tag{A.1}$$
$$\Rightarrow f_{in_{(c)}} = \frac{2\pi}{\sqrt{3}}\left(\frac{r_{(c)}}{s_{(c)}}\right)^2$$

A.1.2 Intra-glial volume fraction

On the contrary, glial cells are of finite dimension in all directions such that the contribution in the z-direction must be taken in account. Nevertheless, as the cells are hexagonally distributed, the ratio can be determined by considering only the volume of one prism with an hexagonal base with respect to the volume occupied by the within glial cells :

$$f_{in_{(s)}} = \frac{V_{sph}}{V_{hex}} = \frac{12V_{\bigcirc\!\!\!\frac{}{6}}}{A_{hex}s_{(s)}} \text{ with } \begin{cases} V_{\bigcirc\!\!\!\frac{}{6}} = \dfrac{1}{6}\dfrac{4\pi r_{(s)}^3}{3} \\ A_{hex} = 6A_{\triangle} = 6\dfrac{\sqrt{3}s_{(c,s)}^2}{4} \\ s_{(c,s)} = \dfrac{2}{3}h = \dfrac{s_{(c)}}{\sqrt{3}} \end{cases} \tag{A.2}$$
$$\Rightarrow f_{in_{(s)}} = \frac{16\pi}{3\sqrt{3}}\frac{r_{(s)}^3}{s_{(c)}^2 s_{(s)}}$$

A.2 For crossing fasciles of identical axons surrounded by rectangularly distributed glial cells

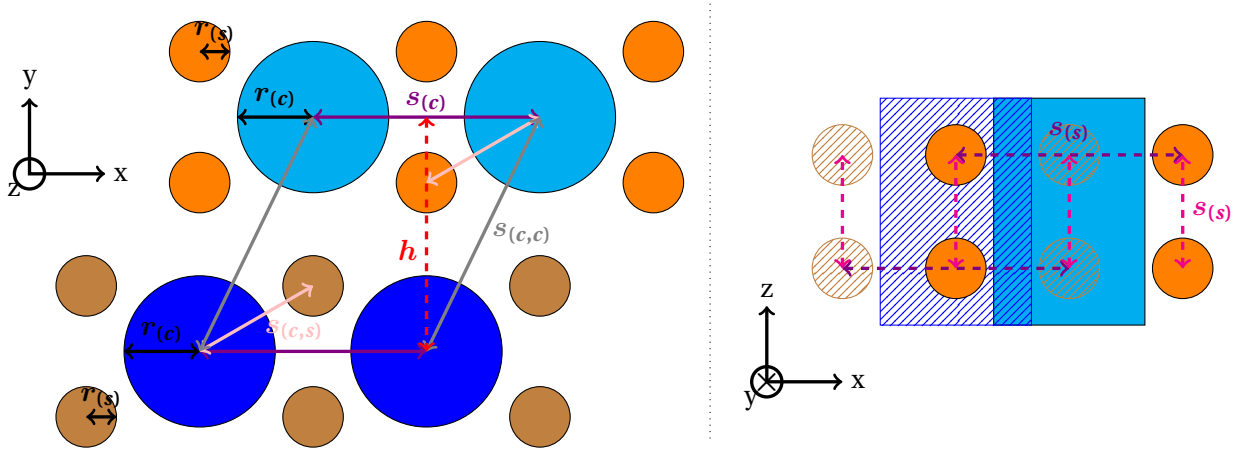

A.2.1 Intra-axonal volume fraction

Due to the fact that the cylinders are infinitely long along their principal direction and that the packing configuration repeats itself along all the directions, the intra-axonal volume fractions is established by the ratio of the area occupied by the cylinders and the area of the enclosing voxel, in the xy-plane, considering no rotation. Additionally, due to the packing configuration, the ratio can be determined by

considering only the area of the parallelogram with respect to the area occupied by the within spherical portions :

$$f_{in_{(c)}} = \frac{A_{cyl}}{A_{parall}} = \frac{2A_{\bigcirc_{\frac{3}{}}} + 2A_{\bigcirc_{\frac{6}{}}}}{A_{parall}} \text{ with } \begin{cases} A_{\bigcirc_{\frac{3}{}}} = \dfrac{\pi r_{(c)}^2}{3} \\ A_{\bigcirc_{\frac{6}{}}} = \dfrac{\pi r_{(c)}^2}{6} \\ A_{parall} \overset{h=s_{(c)}}{=} s_{(c)}^2 \end{cases} \tag{A.3}$$

$$\Rightarrow f_{in_{(c)}} = \pi \left(\frac{r_{(c)}}{s_{(c)}} \right)^2$$

A.2.2 Intra-glial volume fraction

In a similar manner, except this time the contribution along the z-axis must be taken in account, the intra-glial volume fraction is given by the ratio of the volume of one parallelepiped with respect to the volume occupied by the within glial cells :

$$f_{in_{(s)}} = \frac{V_{sph}}{V_{parall}} = \frac{4V_{\bigcirc_{\frac{2}{}}}}{A_{parall} s_{(s)}} \text{ with } \begin{cases} V_{\bigcirc_{\frac{2}{}}} = \dfrac{1}{2} \dfrac{4\pi r_{(s)}^3}{3} \\ A_{parall} = s_{(c)}^2 \end{cases} \tag{A.4}$$

$$\Rightarrow f_{in_{(s)}} = \frac{8\pi}{3} \frac{r_{(s)}^3}{s_{(c)}^2 s_{(s)}}$$

Appendix B

MC simulation parameters

B.1 Standard deviation study

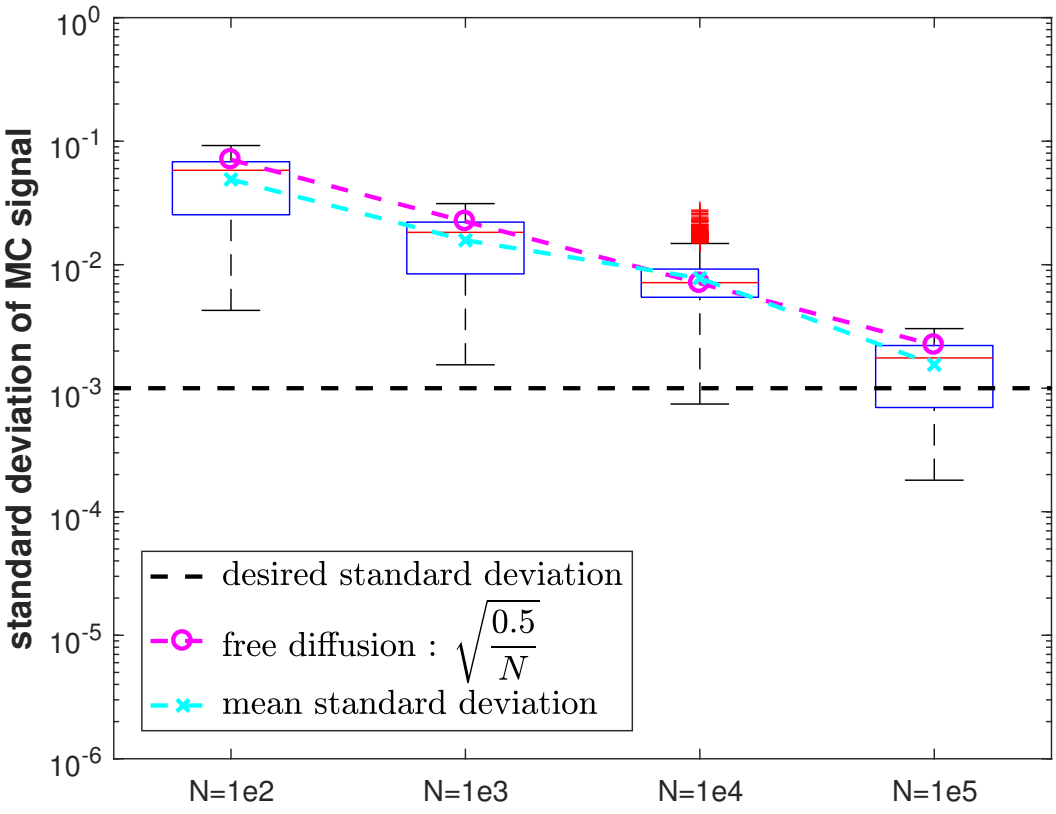

FIGURE B.1: **Variation of the standard deviation in fonction of the number N of spins using a custom multi-shell scheme for the crossing fascicles environment and with the number T of time steps fixed to $2x10^4$.**

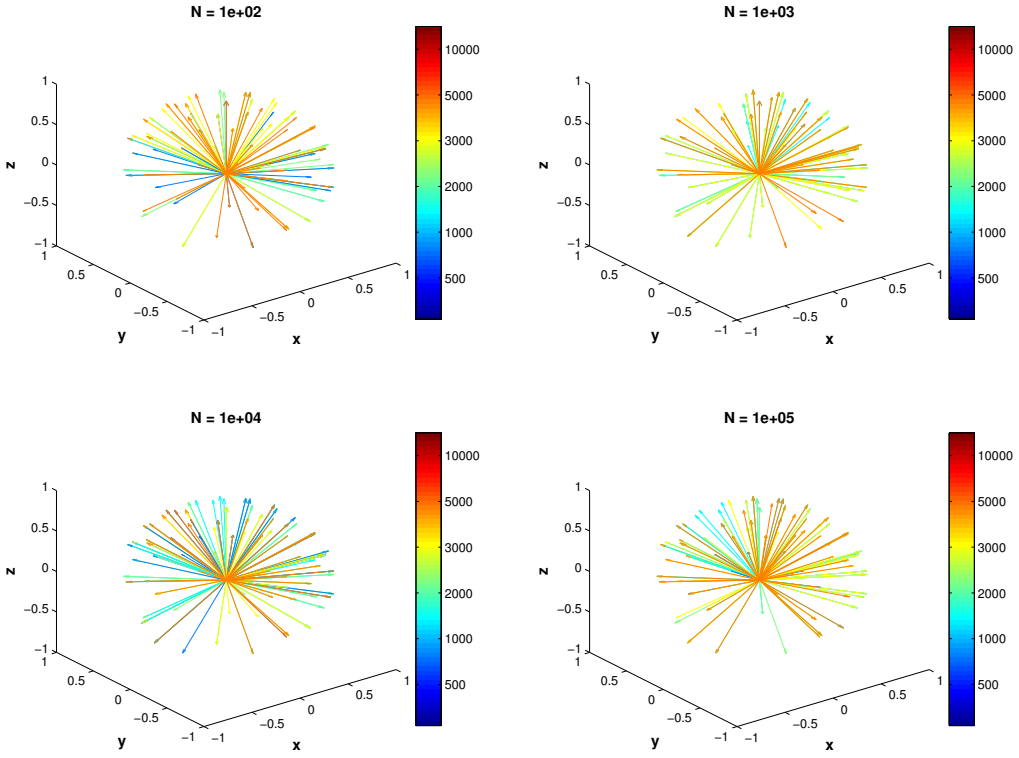

FIGURE B.2: **Representation of the b-vectors that yield a standard deviation higher than the standard deviation of the free diffusion for the crossing fascicles environment.** The colorbar represents the intensity of the b-values, whereas the arrows represent their gradient directions.

B.2 Bias study

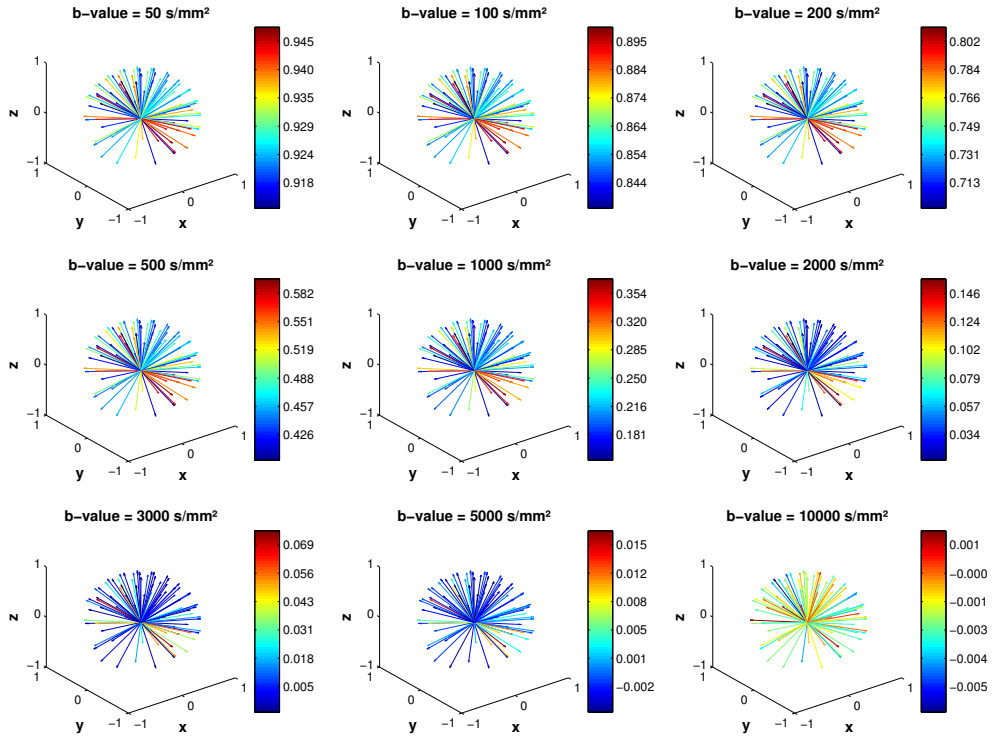

FIGURE B.3: **Attenuation signal in function of the gradient direction $\hat{g}$ for various b-values and for the crossing fascicles environment, using a number** N **of spins equal to** $1.5x10^4$ **and a number** T **of time step equal to** 10^6**.** The colorbar represents the intensity of the attenuation signal, whereas the arrows represent the gradient directions of the b-vectors. Moreover, the negative signal attenuation, observed for high b-values (i.e. $5000\frac{s}{mm^2}$ and $1000\frac{s}{mm^2}$) are due to numerical truncation errors, as the computed signals are really low.

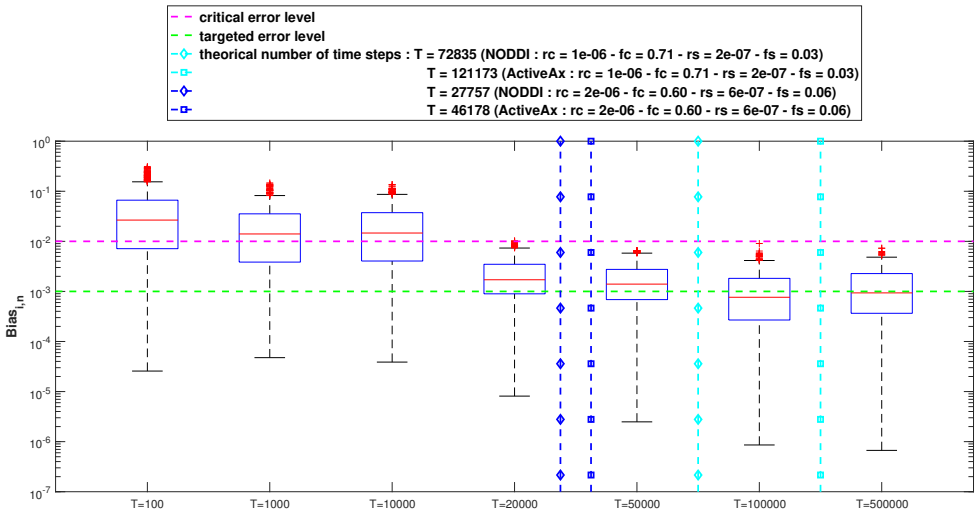

FIGURE B.4: **Variation of the bias in fonction of the number** T **of time steps using a custom multi-shell scheme for the crossing fascicles environment and with the number** N **of spins fixed to** $1.5x10^4$**.**

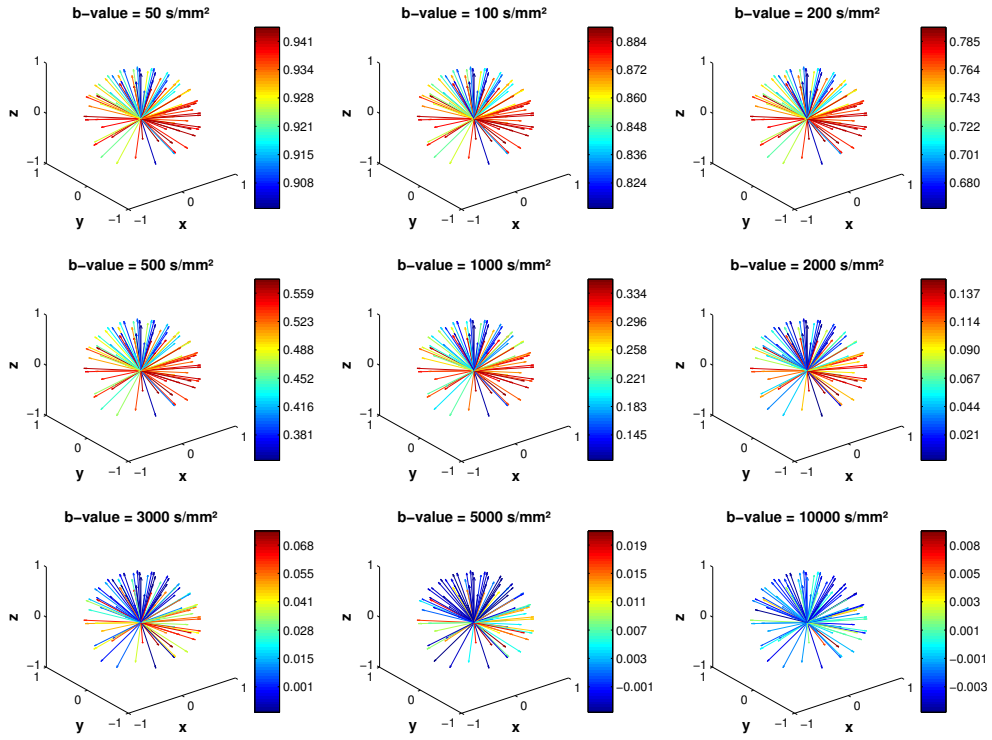

FIGURE B.5: **Attenuation signal in function of the gradient direction $\hat{g}$ for various b-values and for a environment with gamma-distributed cylinder radii, using a number N of spins equal to $1.5x10^4$ and a number T of time step equal to 10^6.** The colorbar represents the intensity of the attenuation signal, whereas the arrows represent the gradient directions of the b-vectors. Moreover, the negative signal attenuation, observed for high b-values (i.e. $5000\frac{s}{mm^2}$ and $1000\frac{s}{mm^2}$) are due to numerical truncation errors, as the computed signals are really low.

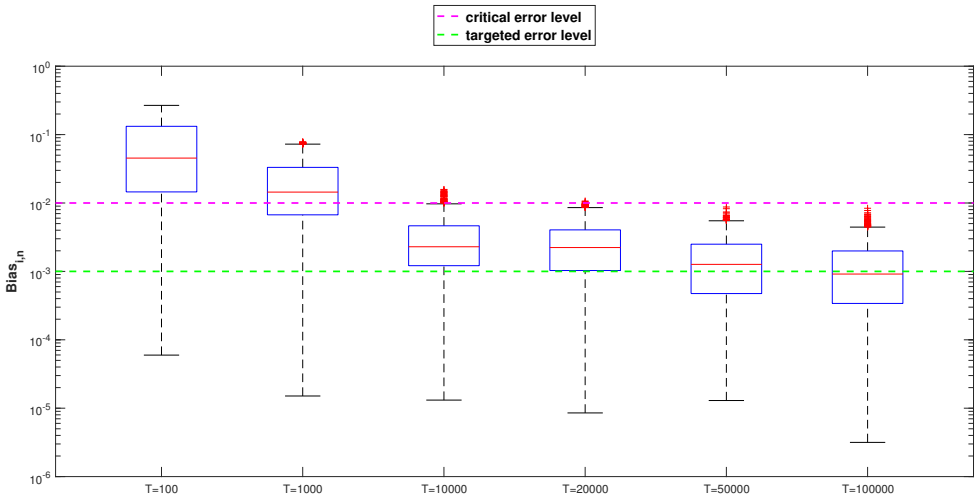

FIGURE B.6: **Variation of the bias in fonction of the number T of time steps using a custom multi-shell scheme for a environment with gamma-distributed cylinder radii and with the number N of spins fixed to $1.5x10^4$.**

Appendix C

Comparison of DWI signals for the second set of microstructure parameters

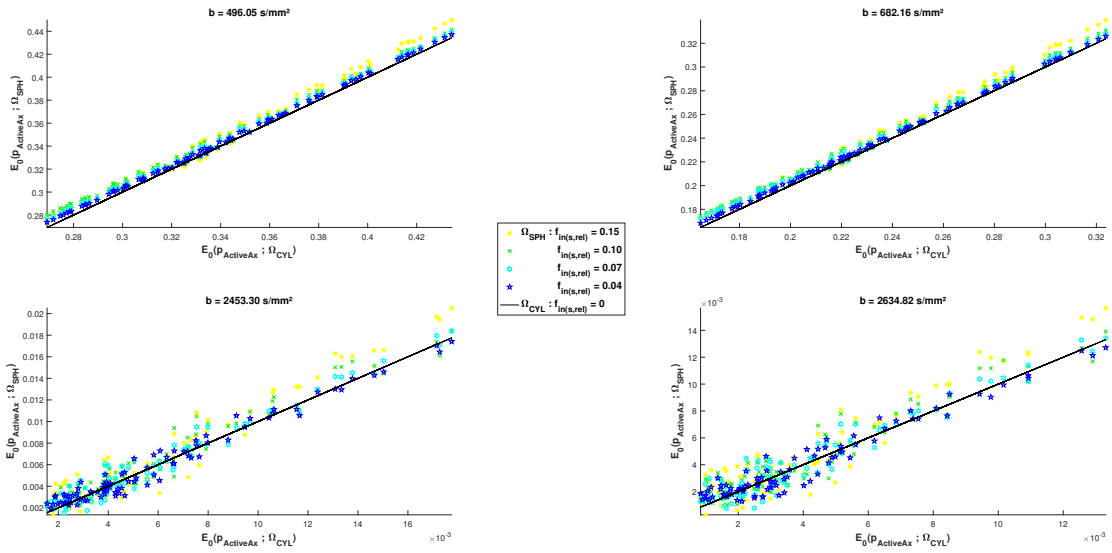

FIGURE C.1: **MC attenuation signals obtained using the ActiveAx-like scheme for the crossing fasciles of identical axons environment with vs without pores.**

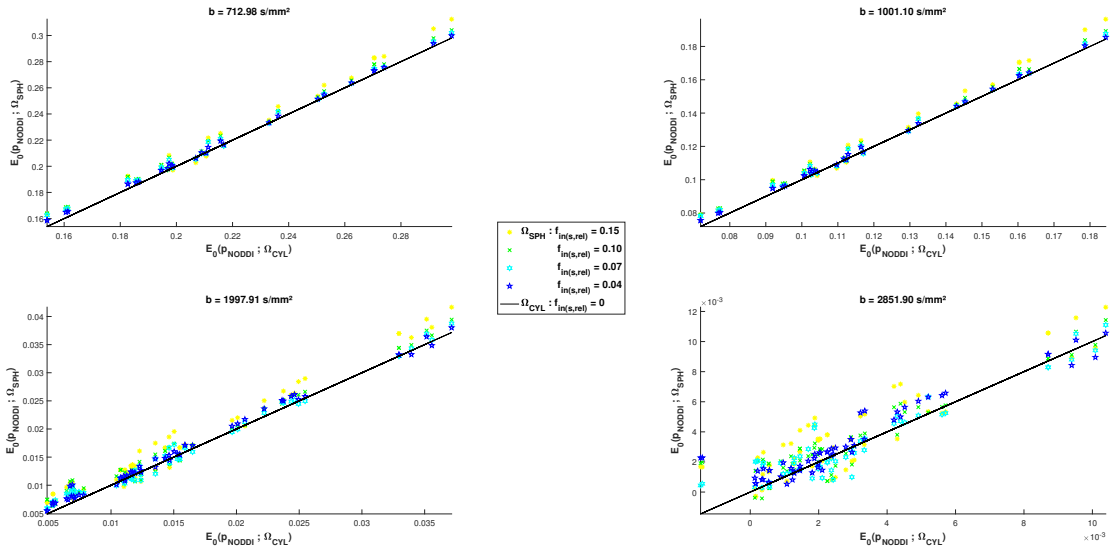

FIGURE C.2: **MC attenuation signals obtained using the NODDI-like scheme for the crossing fasciles of identical axons environment with vs without pores.**

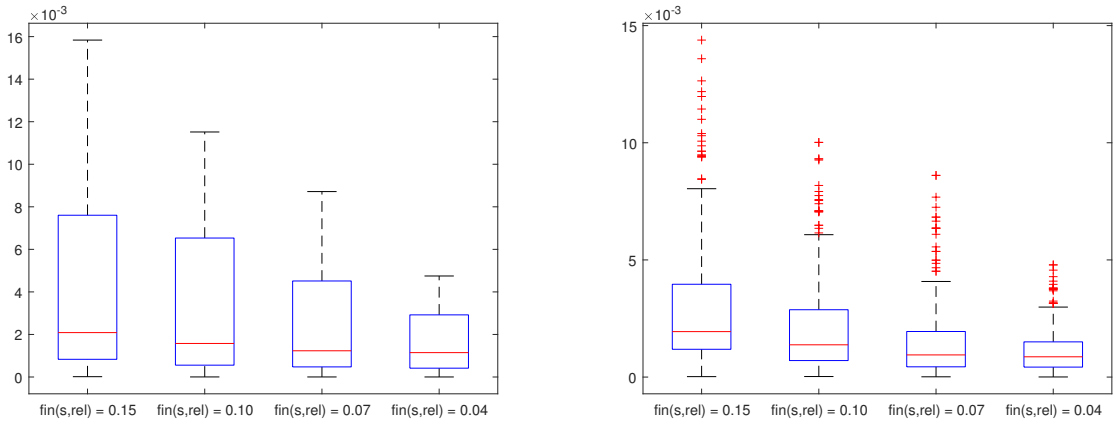

(A) **Using ActiveAx-like scheme.** (B) **Using NODDI-like scheme.**

FIGURE C.3: **Differences between the MC signals computed with and without pores.**

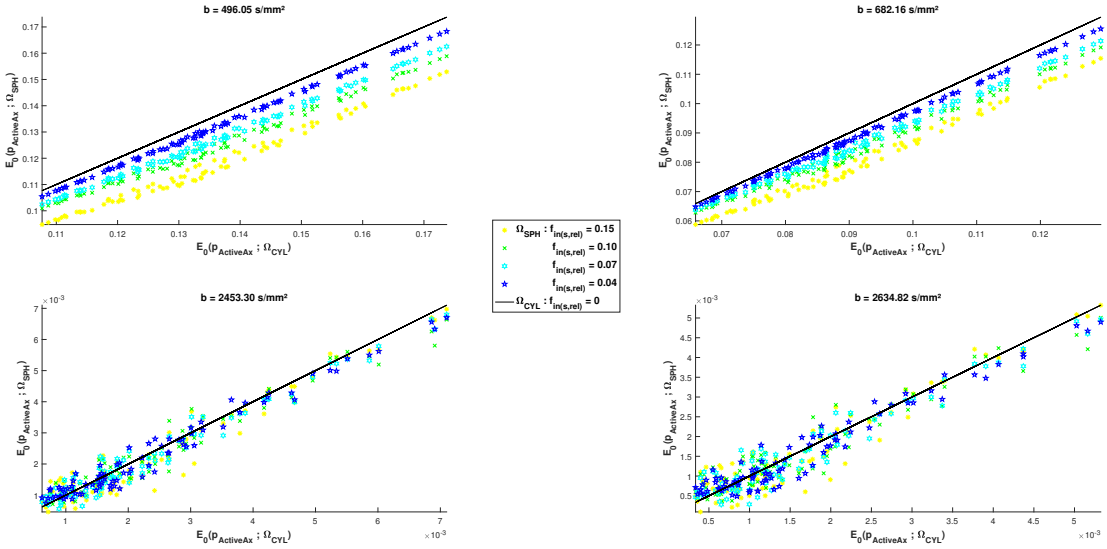

FIGURE C.4: **Attenuation signals obtained using the ActiveAx-like scheme for the crossing fasciles of identical axons environment with vs without pores considered without water molecules.**

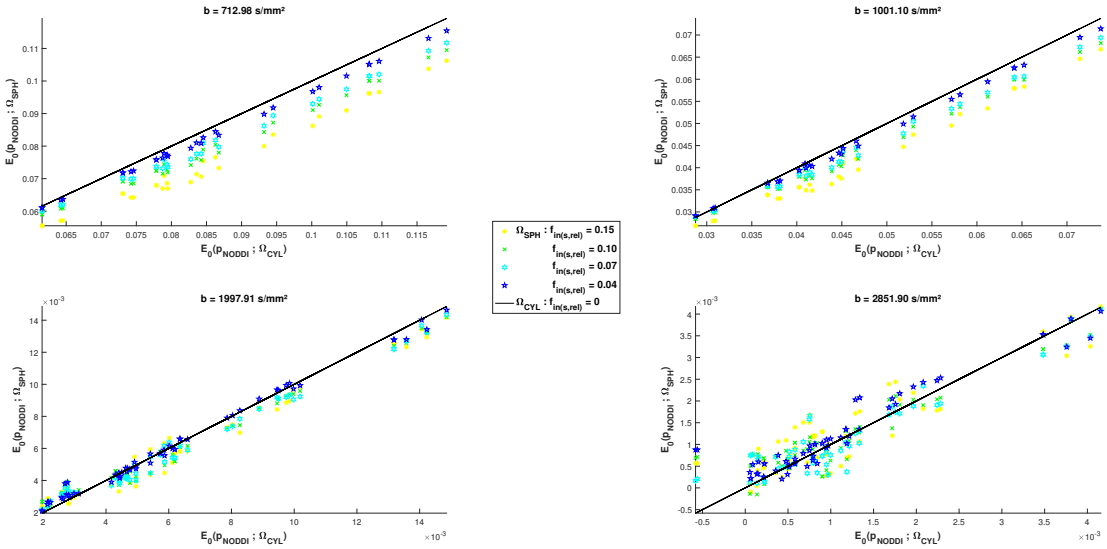

FIGURE C.5: **Attenuation signals obtained using the NODDI-like scheme for the crossing fasciles of identical axons environment with vs without pores considered without water molecules.**

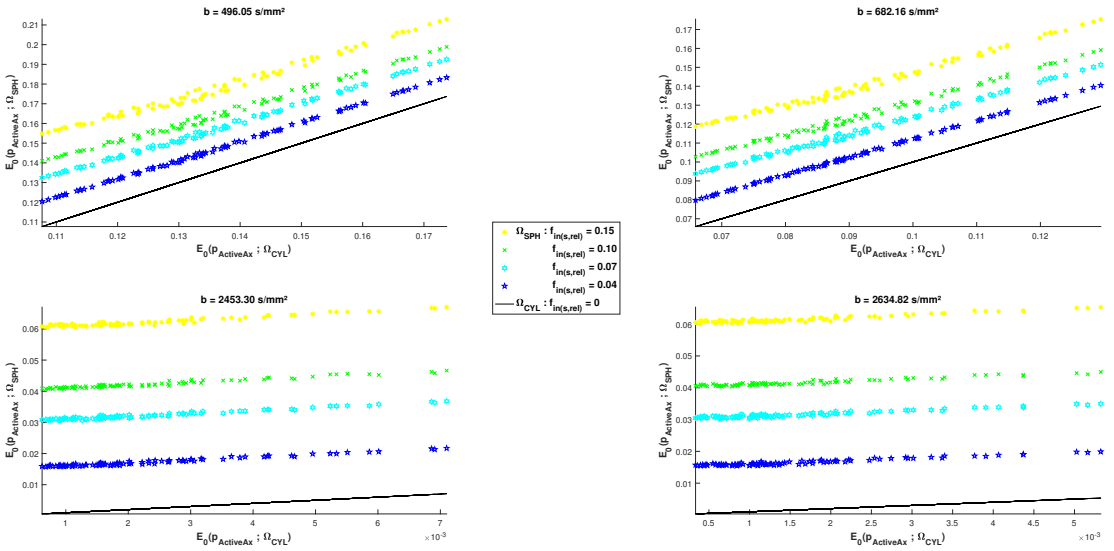

FIGURE C.6: **Attenuation signals obtained using the ActiveAx-like scheme for the crossing fasciles of identical axons environment with vs without pores considered filled with water molecules.**

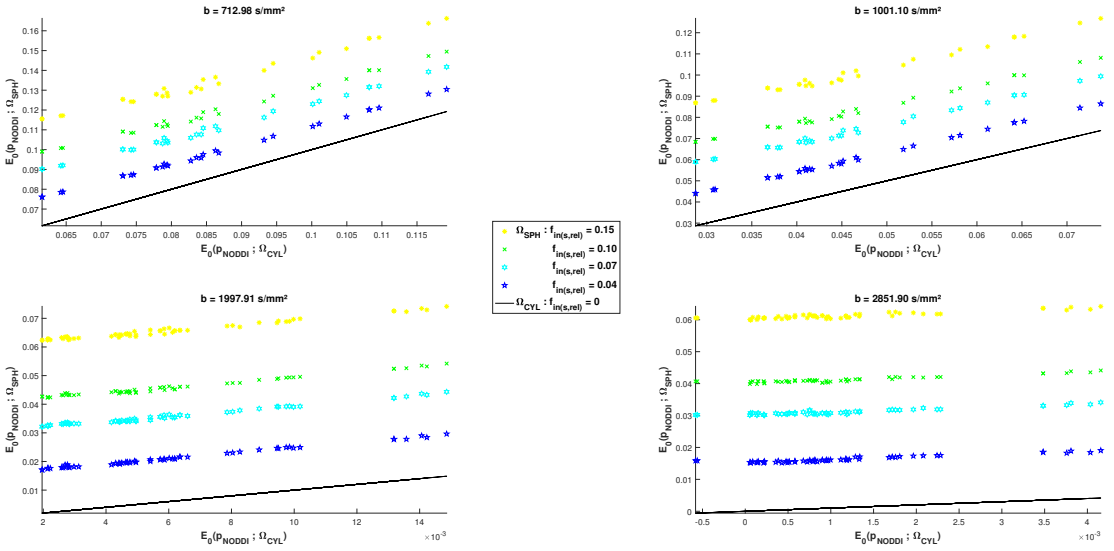

FIGURE C.7: **Attenuation signals obtained using the NODDI-like scheme for the crossing fasciles of identical axons environment with vs without pores considered filled with water molecules.**

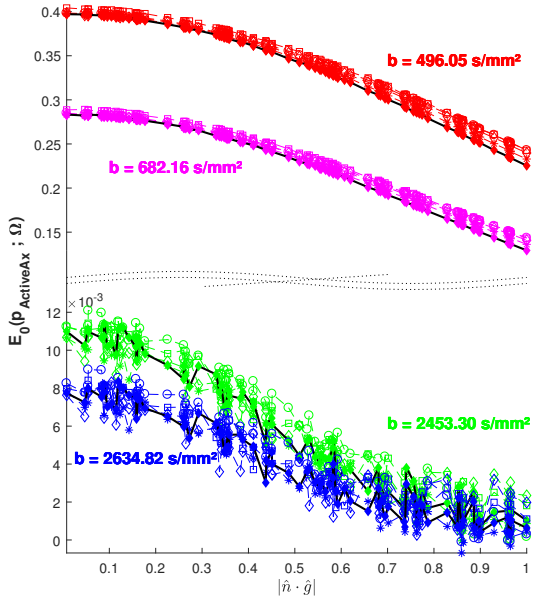

(A) **MC signals for comparison following 3.7a.**

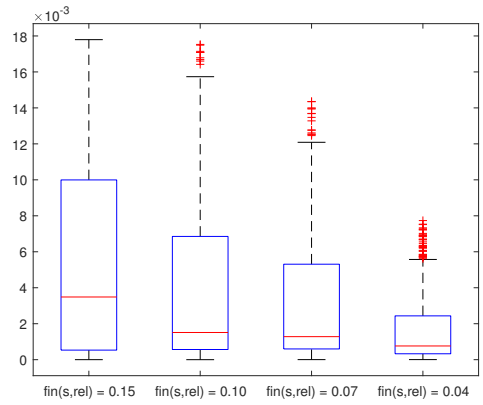

(B) **Differences between the MC signals computed with and without pores.**

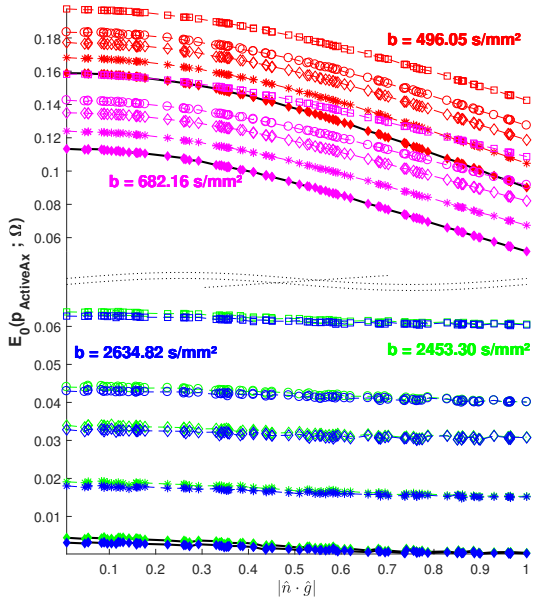

(C) **Total signals with pores considered filled with water molecules for comparison following 3.7c.**

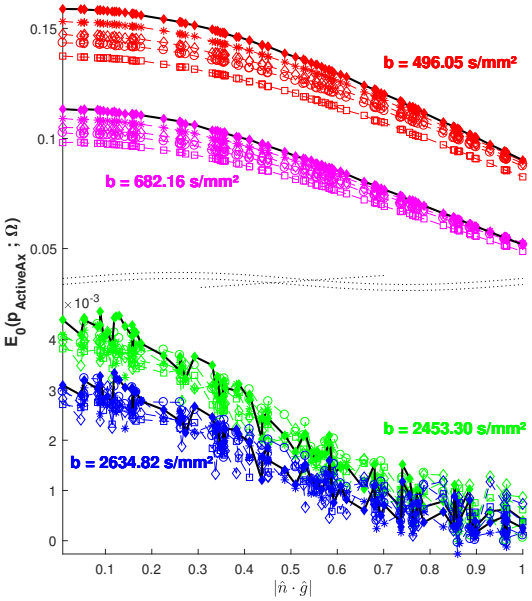

(D) **Total signals with pores considered without water molecules for comparison following 3.7b.**

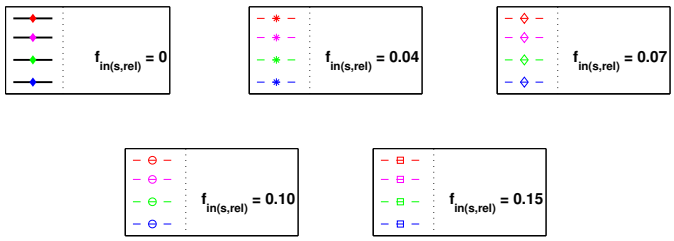

(E) **Legend for the three signal plots.**

FIGURE C.8: **Attenuation signals obtained using the ActiveAx-like scheme for the hexagonally packed fasciles of identical axons environment with vs without pores.** The two dashed line crossed by another dash line are there to delimit the two different scales used respectively for lower and higher b-values.

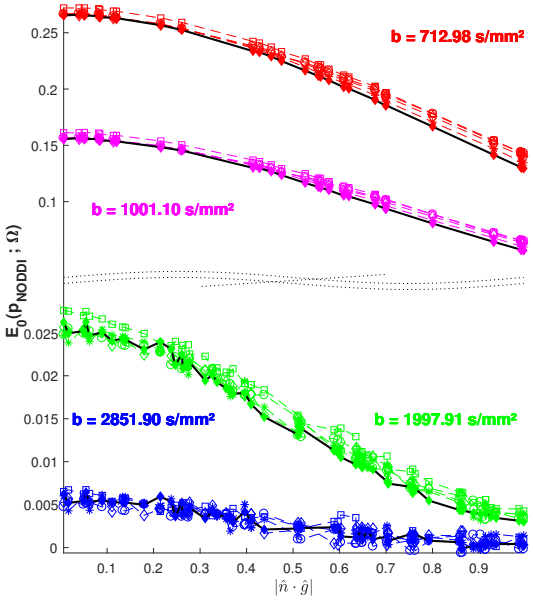

(A) **MC signals for comparison following 3.7a.**

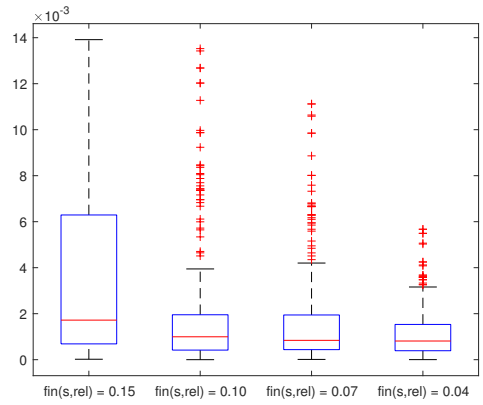

(B) **Differences between the MC signals computed with and without pores.**

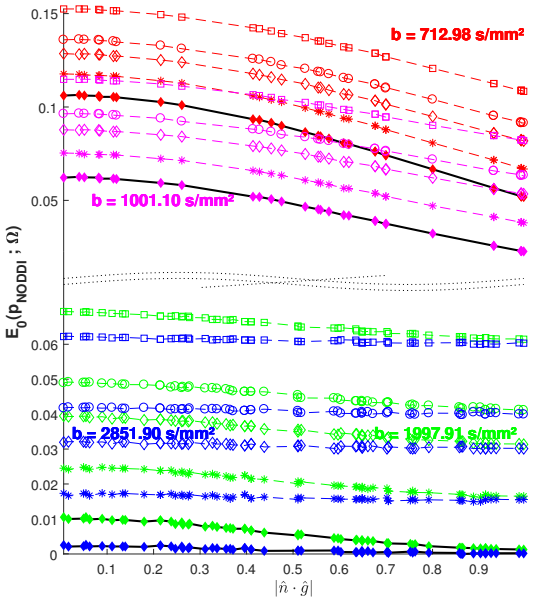

(C) **Total signals with pores considered filled with water molecules for comparison following 3.7c.**

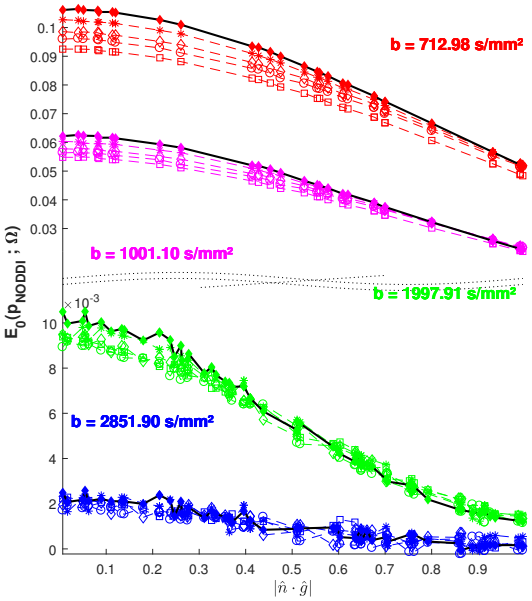

(D) **Total signals with pores considered without water molecules for comparison following 3.7b.**

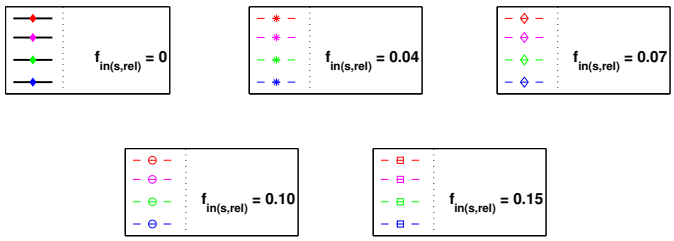

(E) **Legend for the three signal plots.**

FIGURE C.9: **Attenuation signals obtained using the NODDI-like scheme for the hexagonally packed fasciles of identical axons environment with vs without pores.** The two dashed line crossed by another dash line are there to delimit the two different scales used respectively for lower and higher b-values.

Appendix D

Determination of the effective extracellular diffusivity for the second set of microstructure parameters

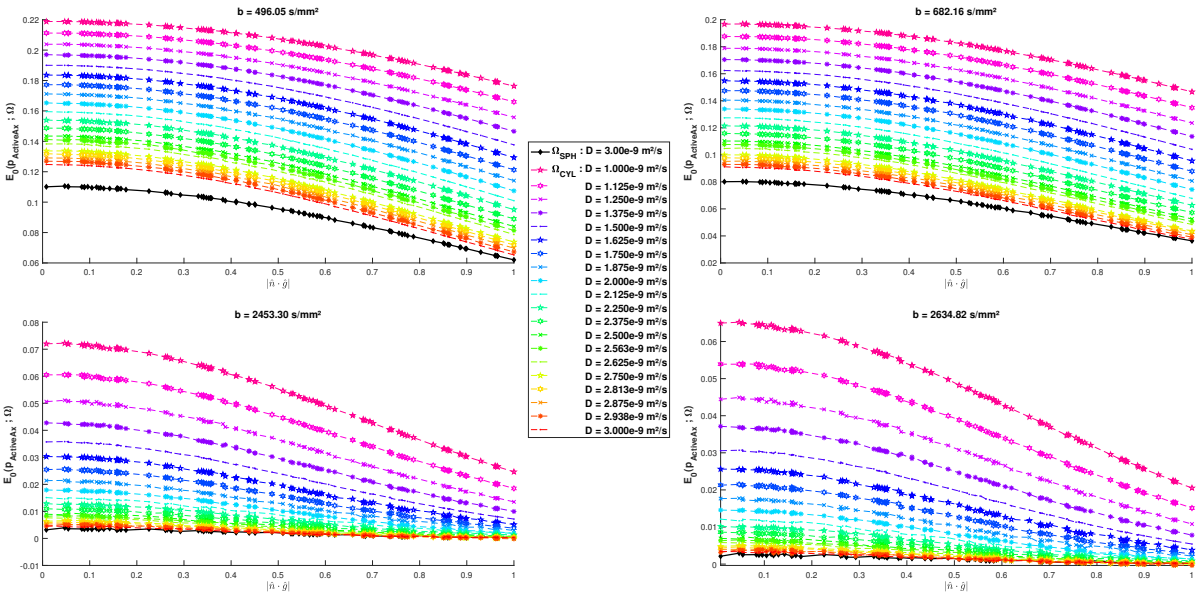

FIGURE D.1: **Attenuation signals obtained using the ActiveAx-like scheme for the hexagonally packed fasciles of identical axons environment, considering various diffusivity values when no pores are present and the intrinsic diffusivity value D_{int} when empty rigid pores are present, with a relative intra-pore volume fraction $f_{in_{(s,rel)}}$ of 0.15.**

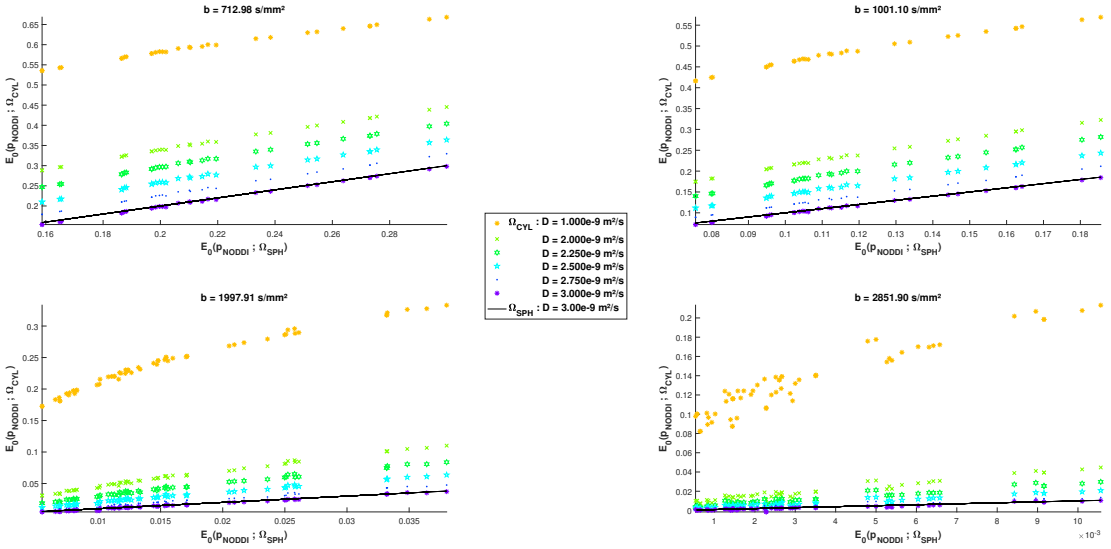

FIGURE D.2: **MC signals obtained using the NODDI-like scheme for the crossing fasciles of identical axons environment, considering various diffusivity values when no pores are present and the intrinsic diffusivity value D_{int} when pores are present, with a relative intra-pore volume fraction $f_{in_{(s,rel)}}$ of 0.04.**

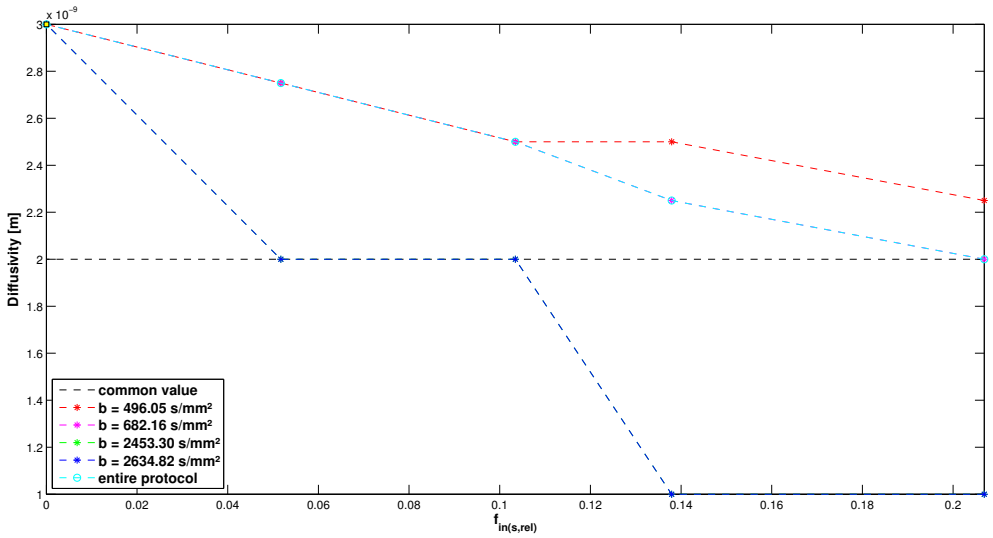

(A) **Using ActiveAx-like scheme.**

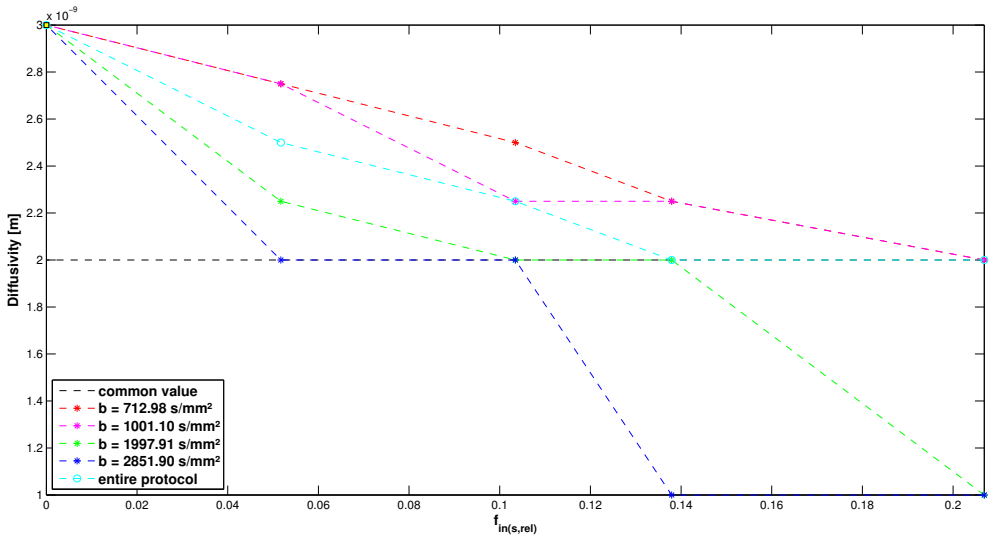

(B) **Using NODDI-like scheme.**

FIGURE D.3: **Variation of the effective extracellular diffusivity D_{eff} in function of the relative intra-pore volume fraction $f_{in_{(s,rel)}}$ for hexagonally packed fasciles of identical axons environment without pores with respect to the similar environment with pores, using the microstructure parameters of the firs set.**

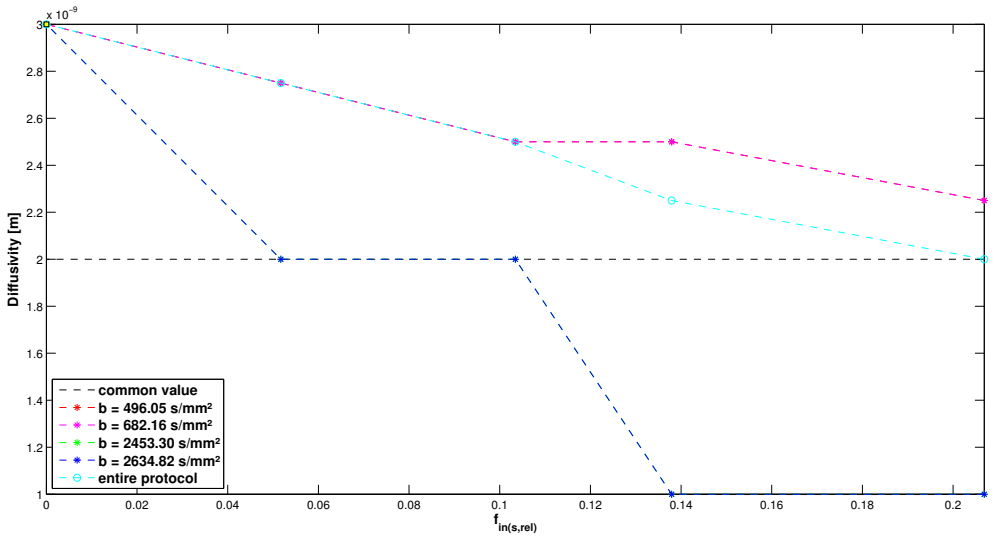

(A) **Using ActiveAx-like scheme.**

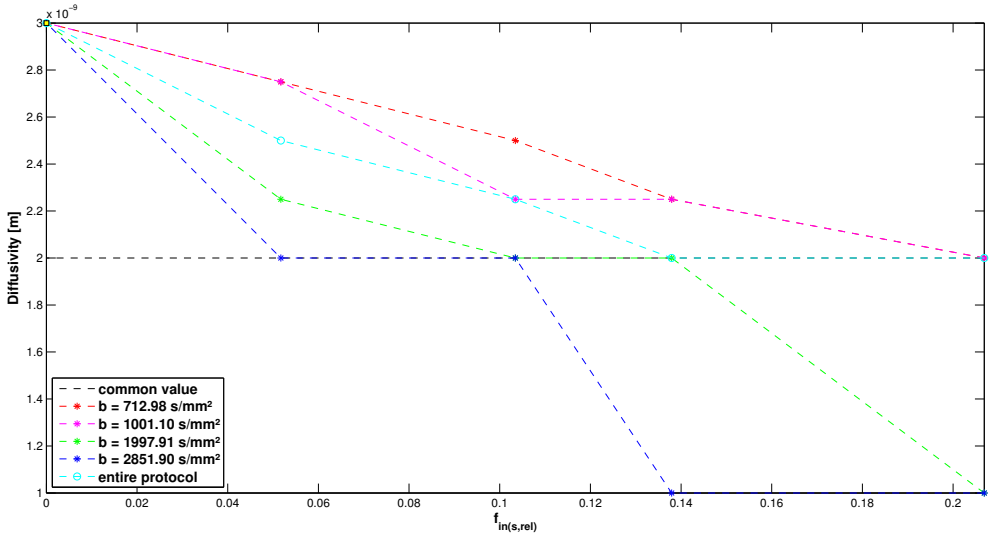

(B) **Using NODDI-like scheme.**

FIGURE D.4: **Variation of the effective extracellular diffusivity D_{eff} in function of the relative intra-pore volume fraction $f_{in_{(s,rel)}}$ for crossing fasciles of identical axons environment without pores with respect to the similar environment with pores, using the microstructure parameters of the firs set.**

Bibliography

[1] Francisco Aboitiz et al. “Fiber composition of the human corpus callosum”. In: *Brain research* 598.1 (1992), pp. 143–153.

[2] Daniel C Alexander. “A general framework for experiment design in diffusion MRI and its application in measuring direct tissue-microstructure features”. In: *Magnetic Resonance in Medicine* 60.2 (2008), pp. 439–448.

[3] Daniel C Alexander et al. “Orientationally invariant indices of axon diameter and density from diffusion MRI”. In: *Neuroimage* 52.4 (2010), pp. 1374–1389.

[4] Yaniv Assaf et al. “New modeling and experimental framework to characterize hindered and restricted water diffusion in brain white matter”. In: *Magnetic Resonance in Medicine* 52.5 (2004), pp. 965–978.

[5] Peter J Basser, James Mattiello, and Denis LeBihan. “MR diffusion tensor spectroscopy and imaging”. In: *Biophysical journal* 66.1 (1994), pp. 259–267.

[6] Christian Beaulieu. “The basis of anisotropic water diffusion in the nervous system–a technical review”. In: *NMR in Biomedicine* 15.7-8 (2002), pp. 435–455.

[7] Paul Browne et al. “Atlas of Multiple Sclerosis 2013: A growing global problem with widespread inequity”. In: *Neurology* 83.11 (2014), pp. 1022–1024.

[8] Chris A Clark and Denis Le Bihan. “Water diffusion compartmentation and anisotropy at high b values in the human brain”. In: *Magnetic Resonance in Medicine* 44.6 (2000), pp. 852–859.

[9] Ivana Drobnjak et al. “PGSE, OGSE, and sensitivity to axon diameter in diffusion MRI: insight from a simulation study”. In: *Magnetic resonance in medicine* 75.2 (2016), pp. 688–700.

[10] Mayada Elsabbagh et al. “Global prevalence of autism and other pervasive developmental disorders”. In: *Autism Research* 5.3 (2012), pp. 160–179.

[11] Rutger Fick et al. “Diffusion MRI Anisotropy: Modeling, Analysis and Interpretation”. In: (2017).

[12] Denis S Grebenkov. “Laplacian eigenfunctions in NMR. I. A numerical tool”. In: *Concepts in Magnetic Resonance Part A* 32.4 (2008), pp. 277–301.

[13] Denis S Grebenkov. “NMR survey of reflected Brownian motion”. In: *Reviews of Modern Physics* 79.3 (2007), p. 1077.

[14] Matt G Hall and Daniel C Alexander. “Convergence and parameter choice for Monte-Carlo simulations of diffusion MRI”. In: *IEEE transactions on medical imaging* 28.9 (2009), pp. 1354–1364.

[15] Scott N Hwang et al. “An image-based finite difference model for simulating restricted diffusion”. In: *Magnetic Resonance in Medicine* 50.2 (2003), pp. 373–382.

[16] Damien Jacobs. *Characterization of Wallerian Degeneration by In Vivo Diffusion Compartment Imaging*. 2015.

[17] Doctor Klioze. *MRI: Basic Physics & a Brief History*. Youtube Video. Nov. 2013. URL: `https://www.youtube.com/watch?v=djAxjtN$\_$7VE`.

[18] Daniel Liewald et al. “Distribution of axon diameters in cortical white matter: an electron-microscopic study on three human brains and a macaque”. In: *Biological cybernetics* 108.5 (2014), pp. 541–557.

[19] Damien J McHugh et al. “Ground Truth for Diffusion MRI in Cancer: A Model-Based Investigation of a Novel Tissue-Mimetic Material”. In: *International Conference on Information Processing in Medical Imaging*. Springer. 2015, pp. 179–190.

[20] C Meca, S Chabert, and D Le Bihan. “Diffusion MRI at large b values: what’s the limit”. In: *Proceedings of the 12th Annual Meeting of ISMRM, Kyoto, Japan*. 2004, p. 1196.

[21] Eleftheria Panagiotaki et al. “Compartment models of the diffusion MR signal in brain white matter: a taxonomy and comparison”. In: *Neuroimage* 59.3 (2012), pp. 2241–2254.

[22] Frank Peeters. *Chapter 4 : Magnetic Resonance Imaging*. Course-Notes, 2017.

[23] William S Price. *NMR studies of translational motion: principles and applications*. Cambridge University Press, 2009.

[24] Nadya Pyatigorskaya et al. “Relationship between the diffusion time and the diffusion MRI signal observed at 17.2 tesla in the healthy rat brain cortex”. In: *Magnetic resonance in medicine* 72.2 (2014), pp. 492–500.

[25] Gaëtan Rensonnet. “Generation of dictionary of DW-MRI signals from arbitrary brain microstructure configurations”. MA thesis. Université Catholique de Louvain, June 2015, pp. 3–21.

[26] Benoit Scherrer and Simon K Warfield. “Parametric representation of multiple white matter fascicles from cube and sphere diffusion MRI”. In: *PLoS one* 7.11 (2012), e48232.

[27] Benoit Scherrer et al. “Characterizing the distribution of anisotropic micro-structural environments with diffusion-weighted imaging (DIAMOND)”. In: *Medical image computing and computer-assisted intervention: MICCAI... International Conference on Medical Image Computing and Computer-Assisted Intervention*. Vol. 16. 0 3. NIH Public Access. 2013, p. 518.

[28] Aaron Szafer, Jianhui Zhong, and John C Gore. “Theoretical model for water diffusion in tissues”. In: *Magnetic resonance in medicine* 33.5 (1995), pp. 697–712.

[29] Maxime Taquet. *Diffusion-weighted MRI and Microstructure Imaging*. Youtube Video. Sept. 2015. URL: `https://www.youtube.com/watch?v=-JGLhF5FiGY`.

[30] David S Tuch et al. “High angular resolution diffusion imaging reveals intravoxel white matter fiber heterogeneity”. In: *Magnetic resonance in medicine* 48.4 (2002), pp. 577–582.

[31] Van J Wedeen et al. “Mapping complex tissue architecture with diffusion spectrum magnetic resonance imaging”. In: *Magnetic resonance in medicine* 54.6 (2005), pp. 1377–1386.

[32] R.R. Weynants and P. Vandenplas. *Physique V - Partie 1 : Mecanique Quantique*. 2006.

[33] Chun-Hung Yeh et al. “Diffusion microscopist simulator: a general Monte Carlo simulation system for diffusion magnetic resonance imaging”. In: *PloS one* 8.10 (2013), e76626.

[34] Hui Zhang et al. “NODDI: practical in vivo neurite orientation dispersion and density imaging of the human brain”. In: *Neuroimage* 61.4 (2012), pp. 1000–1016.

Rue Archimède, 1 bte L6.11.01, 1348 Louvain-la-Neuve **www.uclouvain.be/epl**